

ADA034066

AFGL-TR-76-0231

**ANALYSIS AND PROGRAMMING FOR RESEARCH IN
PHYSICS OF THE UPPER ATMOSPHERE**

James N. Bass
Krishin H. Bhavnani
Ben-Zion J. Guz
Robert R. Hayes
Paul N. Houle
Shu T. Lai
Leo A. Whelan

New
409990
Logicon, Inc.
P.O. Box 451
Bedford, Massachusetts 01730



30 September 1976

Final Report for Period 1 September 1974 - 31 August 1976

Approved for public release; distribution unlimited.

AIR FORCE GEOPHYSICS LABORATORY
AIR FORCE SYSTEMS COMMAND
UNITED STATES AIR FORCE
HANSOM AFB, MASSACHUSETTS 01731

**COPY AVAILABLE TO DDC DOES NOT
PERMIT FULLY LEGIBLE PRODUCTION**

Qualified requestors may obtain additional copies from the Defense Documentation Center. All others should apply to the National Technical Information Service.

Unclassified

SECURITY CLASSIFICATION OF THIS PAGE (When Data Entered)

REPORT DOCUMENTATION PAGE		READ INSTRUCTIONS BEFORE COMPLETING FORM																
1. REPORT NUMBER 18 AFGL-TR-76-0231	2. GOVT ACCESSION NO.	3. PECIEN'TS STLOC NUMBER 9																
4. TITLE (and subtitle) ANALYSIS AND PROGRAMMING FOR RESEARCH IN PHYSICS OF THE UPPER ATMOSPHERE		5. TYPE OF REPORT & PERIOD COVERED Final rept. 1 Sept 1974 - 31 Aug 1976																
6. AUTHOR(s) James N. Bass, Krishin H. Bhavnani, Ben-Zion J. Guz		7. CONTRACT OR GRANT NUMBER(S) F19628-75-C-0039																
8. PERFORMING ORGANIZATION NAME AND ADDRESS Logicon, Inc. P.O. Box 451 Bedford, Massachusetts 01730		10. PROGRAM ELEMENT, PROJECT, TASK AREA & WORK UNIT NUMBERS P - n/a-Tn/a-WUn/a PE 61102F																
11. CONTROLLING OFFICE NAME AND ADDRESS Air Force Geophysics Laboratory Hanscom AFB, Massachusetts 01731 Contract Monitor: Isabel M. Hussey/SUYA		12. REPORT DATE 30 Sep 1976																
13. NUMBER OF PAGES 211		14. MONITORING AGENCY NAME & ADDRESS (if different from Controlling Office)																
15. SECURITY CLASS. (of this report) Unclassified		15a. DECLASSIFICATION/DOWNGRADING SCHEDULE																
16. DISTRIBUTION STATEMENT (of this Report) Approved for public release; distribution unlimited. 12 212p.																		
17. DISTRIBUTION STATEMENT (of the abstract entered in Block 20, if different from Report)																		
18. SUPPLEMENTARY NOTES Tech, Other																		
19. KEY WORDS (Continue on reverse side if necessary and identify by block number) <table> <tr> <td>Computer Programs</td> <td>Geopotential Models</td> <td>Rocket Trajectory</td> </tr> <tr> <td>Astronomical Ephemeris</td> <td>Ionospheric Research</td> <td>Satellite Orbits</td> </tr> <tr> <td>Atmospheric Density</td> <td>Orbit Determination</td> <td>Satellite Wire-Boom Dynamics</td> </tr> <tr> <td>Auroral Morphology</td> <td>Plasma Motion</td> <td>Scintillations</td> </tr> <tr> <td>Electric Fields</td> <td>Radar Signal Processing</td> <td></td> </tr> </table>				Computer Programs	Geopotential Models	Rocket Trajectory	Astronomical Ephemeris	Ionospheric Research	Satellite Orbits	Atmospheric Density	Orbit Determination	Satellite Wire-Boom Dynamics	Auroral Morphology	Plasma Motion	Scintillations	Electric Fields	Radar Signal Processing	
Computer Programs	Geopotential Models	Rocket Trajectory																
Astronomical Ephemeris	Ionospheric Research	Satellite Orbits																
Atmospheric Density	Orbit Determination	Satellite Wire-Boom Dynamics																
Auroral Morphology	Plasma Motion	Scintillations																
Electric Fields	Radar Signal Processing																	
20. ABSTRACT (Continue on reverse side if necessary and identify by block number) <p>This report describes significant analyses and computer programming problems performed in support of Air Force Geophysics Laboratory scientists. Mathematical and logical procedures are discussed, and samples of results are presented. Astronomical ephemeris programs include solar-lunar and stellar viewing information, and special plots.</p>																		

409990

VB

Block Number 20.

Orbit determination programs include various types of rapid orbit generation, and modifications to an in-house program.

Atmospheric density and geopotential model studies were conducted in conjunction with elaborate orbit determination programs.

Ionospheric research programs include data reduction and analyses for auroral studies, electric field mapping, plasma bulk motion mapping, topside plasma monitoring, and scintillations modeling. A satellite wire-boom dynamics analytical study is summarized.

A radar signal processing task for maximum signal-to-clutter detection is described.

Attachment 20

REF ID:	MAIL Section	<input checked="" type="checkbox"/>
DOC	DATA Section	<input type="checkbox"/>
REMARKS		
JUSTIFICATION		
BY		
DISTRIBUTION/AVAILABILITY CODES		
Distr.	AVAIL. AND/or SPECIAL	
		

Acknowledgments

The coordination, guidance and encouragement of our Contract Monitor, Mrs. Isabel Hussey of the Analysis and Simulation Branch, is deeply appreciated.

Ms. Eunice Cronin, Branch Chief, and Mr. Edward Robinson, Alternate Contract Monitor, both of the Analysis and Simulation Branch have provided invaluable help through their involvement and interest in many of the projects.

Thanks are also due to the initiators and investigators on the various projects, whose technical motivation and direction has consistently benefited our participation in AFGL research.

Ms. Karen Favreau and Miss Andrea Weiss of Logicon were admirably adaptive and efficient in handling the technical typing, diagrams, and revisions.

Mr. Krishin H. Bhavnani, Technical Contract Manager for Logicon, edited this report.

Table of Contents

<u>Section</u>		<u>Page</u>
1.	<u>Astronomical Ephemeris Programs</u>	11
1.1	Lunar Phase and Illumination	12
1.2	STELAZ and Polaris	13
1.3	Program ECLPLOT	18
1.4	Program SOLPLT	19
2.	<u>Arctic Ionospheric Research</u>	24
2.1	Program ISOZEN	25
2.2	Photometric Data Presentation	28
2.3	DAASM Flight Program	32
2.4	ISIS-2 Data Base	35
2.5	Auroral Morphology Study (Part II)	37
2.6	IORPL Library	41
3.	<u>Rapid Orbit Prediction Program - ROPP</u>	42
3.1	C _D A/M Optimization	43
3.2	Position and Velocity I/O	45
3.3	Other Modifications	45
3.4	Problems with ADC and SCF Elements	48
3.5	Parameter - Lifetime Study	54
4.	<u>Satellite Ephemeris Generation Program - LOKANGL</u>	56
4.1	Use of Element - Sets	57
4.2	Use of Successive Sets of Elements	60
4.3	Input of SCF Position-Velocity Vectors	61
4.4	Problems with ADC Elements	64
4.5	Other Modifications	69
5.	<u>Satellite Orbit Support Programs</u>	72
5.1	Apogee-Perigee Program AP	73
5.2	Program PLOTIT	73
5.3	Satellite Visibility Program MINVIS	76

Table of Contents (cont.)

<u>Section</u>		<u>Page</u>
6.	<u>Satellite Orbit Determination Program - DABOS</u>	78
6.1	Smoothing	79
6.2	Observation System Bias Estimation	81
6.3	Atmospheric Density Models.	82
6.4	Earth's Gravitational Field	84
7.	<u>Atmospheric Density Studies</u>	91
8.	<u>Geopotential Model Studies</u>	102
8.1	Procedure	103
8.2	Results	106
8.3	Comparison of Close Orbit Characteristics	111
8.4	Resonant Terms	116
8.5	Uncertainties in Earth Constants	122
8.6	Normalization of Geopotential Coefficients	125
9.	<u>Rocket Trajectory System</u>	127
9.1	Editor-Preprocessor DRIVEA	128
9.2	Filter DRIVEB	238
9.3	Multi-Radar Trajectory DRIVEC	133
10.	<u>Satellite Wire-Boom Dynamics</u>	139
11.	<u>Ionospheric Field Mapping</u>	147
11.1	Data Reduction	148
11.2	Instrumental and Environmental Factors	148
11.3	Graphical Presentations	154
12.	<u>Plasma Bulk Motion</u>	160
12.1	Data Processing	161
12.2	Electron Properties of Plasma	161
12.3	Ion Properties and Flow	166

Table of Contents (cont.)

<u>Section</u>		<u>Page</u>
13.	<u>DMS_P Topside Plasma Monitor</u>	172
13.1	Data Processing System	173
13.2	Determination of Electron and Ion Parameters	175
14.	<u>High Latitude Scintillations Study</u>	180
14.1	Data Base Creation	181
14.2	Modeling	184
14.3	Distribution of Scintillation Index Readings	192
14.4	Other Analyses	197
15.	<u>Real Time Signal Processing with CSP-30</u>	200
15.1	Introduction	201
15.2	Maximum Signal to Clutter Processing	201
15.3	Hardware	203
15.4	Fast Fourier Transform Display	207

List of Figures

<u>Sect. No.</u>		<u>Page</u>
1. 1	STELAZ Output with Culmination and Elongation Angles for Polaris	15
2	Solar Eclipse Viewing Geometry	18
3	ECLPLOT Output for Solar Eclipse of July 10, 1972. . .	20
4	Solar Elevation and Moon Rise-Set Plots for 1976 at AFGL and 20° further North.	22
2. 1	Iso-z zenith Angle Contours in Geomagnetic Coordinates for 180-270E	26
2	Iso-z zenith Angle Contours in Geomagnetic Coordinates for 0-90E	27
3	Photometer Reading Projection--Restricted Background	30
4	Photometer Reading Projection--Succeeding Time . . .	31
5	Doppler Summary Table for 5 Minutes of Flight Time .	34
6	Auroral View From a Geo-stationary Satellite for Selected Ionospheric Conditions.	38
7	Polar Projection and 30 km Tangent Height Contribu- tion for the Study of Figure 6	39
3. 1	ROPP C _D A/M Optimization for Elements 40 Days Apart .	46
2	Full ROPP Output Sample	47
3	ADC-SCF Eccentricity Comparison Before J ₃ Correction to ADC Elements.	51
4	ADC, SCF and ROPP (Predicted) Eccentricities . . .	52
5	Comparison of ROPP and LOKANGL (X) Derived Eccen- tricities Against Argument of Latitude	53
4. 1	ADC 5-Card Element-set Format.	58
2	ADC 2-Card and SCF Position-velocity Element-set Formats	59
3	Comparison of ADC and SCF (X) Derived Semi-major Axes Before and After J ₂ Correction to ADC Elements	65

List of Figures (cont.)

<u>Sect. No.</u>		<u>Page</u>
(cont.)4.	4 ADC, SCF and ROPP (Predicted) Inclinations	66
	5 Comparison of ADC and SCF Eccentricities After J_3 Correction to ADC Elements	67
	6 ADC, SCF and ROPP (Predicted) Perigee Altitudes . . .	68
	7 Card Input Description for Program LOKANGL	70
5.	1 Card Input Description for Program PLOTIT.	74
	2 Perigee and Apogee Plots of Latitude, Altitude and Local Time	75
6.	1 Card Input Description for Program DABOS	87
7.	1 Perigee Latitudes for Satellite DB-7	93
	2 Perigee Heights for Satellite DB-7	94
	3 Perigee Latitudes for Satellite DB-8	95
	4 Perigee Heights for Satellite DB-8	96
	5 Perigee Latitudes for Satellite DB-9	98
	6 Perigee Heights for Satellite DB-9	99
	7 Model Ratios for Satellite DB-9	100
	8 Solar Flux and K_p Index During DB-9 Flight	101
8.	1 Total Prediction Error (km), - Satellite DB-7, Day 76 (1973).	107
	2 In-track Component of Prediction Error (km) - Satellite DB7, Day 76 (1973)	108
	3 Mean Track Prediction Error (km): Product of Semi-major Axis and Error in Sum of Argument of Perigee and Mean Anomaly - Satellite DB7, Day 76 (1973)	109
	4 R.M.S. of the Ratio of Prediction Error Effect to Perturbation Amplitude for Periodic Perturbation .	121
9.	1 Description of DRIVEB Filter Time Limits, KEYOPT, Geoc. Position and Velocity Card Input	129

List of Figures (cont.)

<u>Sect. No.</u>		<u>Page</u>
10.	1 Simulation of Hub Angular Velocity and Boom Deflections Following a Disturbance	142
	2 Nontrivial Harmonic Frequencies of Satellite System Spinning at 3 RPM	145
11.	1 Task Outline for Ionospheric Field Mapping Project.	149
	2 Computed Ambient Electric Field During an Orbit . .	155
	3 Polar Plot of Electric Field Vectors During an Orbit.	156
	4 Polar Plot of Computed Drift Current During an Orbit.	157
	5 Combination Plot of Measurements From the E-Field, Plasma Motion, and High-energy Particle Flux Experiments	159
12.	1 Task Outline for Plasma Bulk Motion Project	162
	2 Data Processing and Computation Flow Chart for Plasma Flow Parameters	163
	3 Plot of Parameters Computed from Electron Sensor Experiment	167
	4 Plot of Measured and Modeled Ion Current During One Satellite Rotation	170
13.	1 Defense Meteorological Systems Project SSIE Sensor Processing System	174
14.	1 Model of Average SI For Goose Bay	187
	2 Average SI Data and Model Plots for Goose Bay for March	188
	3 Average SI Data and Model Plots for Narssarssuaq for March	189
	4 Average SI Data and Model Plots for Narssarssuaq for October	190
	5 Average SI Data and Model Plots for Sagamore Hill for March	191

List of Figures (cont.)

<u>Sect. No.</u>		<u>Page</u>
(cont.) 14.	6 Global High Latitude Model of Average SI Based on ATS-3 Data from 3 Stations.	193
	7 Average SI for March for the 3 Stations as Given by the Global Model.	194
	8 Average and Median SI for Goose Bay for March . .	196
15.	1 CSP-30 Configuration for Maximum Signal to Clutter Processing Experiment.	204
	2 Fast Fourier Transform Display	208
	3 Console Master Switch Register (MSR) Settings to Implement Various Options	209
	4 16-point Complex Simulation Signal Generated By Subroutine VIDEO (Reference 4)	210
	5 Flow Diagram for FFT Display Program	211

1.0 Astronomical Ephemeris Programs

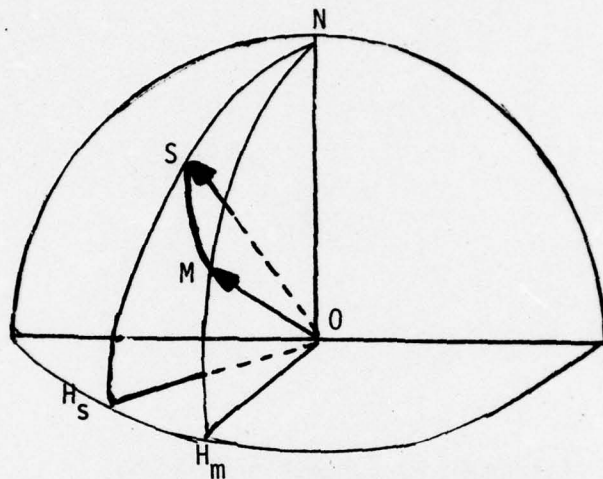
1.1 Calculation of Lunar Phase and Illumination

Initiator: I.M. Hussey

Project No.: 0001

Problem No.: 4510

Using spherical trigonometry, the elongation angle and the phase of the moon can be calculated from the given values of the declination angles and hour angles of the sun and the moon.



$\angle H_s OS$ = Solar Declination (b)

$\angle H_m OM$ = Lunar Declination (c)

$\angle H_s OH_m$ = Difference of Hour Angles of the Sun and the Moon (A)

$\angle SOM$ = Elongation (e)

In the spherical triangle SNM with the centre of the sphere at O, the elongation angle is given by

$$\cos e = \sin b \sin c + \cos b \cos c \cos A$$

The phase of the moon is related to the elongation angle by

$$\text{phase} = \frac{1}{2} (1 - \cos e)$$

For a given phase of the moon, or, equivalently, a given elongation angle, the illumination of the moon can be calculated by means of a curve-fitting method using a set of known elongation-illumination data $\{x_i\}$ as published in "Explanatory Supplement to the Ephemeris"⁽¹⁾. The method used for curve-fitting is based on a cubic equation fit algorithm which provides the coefficients A, B, C, D for each range (x_i, x_{i+1}) of elongation. The illumination F(x) is then given by $F(x) = A_i x^3 + B_i x^2 + C_i x + D_i$ where $x_i < x < x_{i+1}$. These

calculated coefficients for the cubic equation fit are given in the following table:

Range of Elongation	A	B	C	D
0 to 20	$-.9748 \times 10^3$	$.9674 \times 10^2$	0.0	0.0
20 to 40	$-.3425 \times 10$	$.1739 \times 10$	$.2810 \times 10$	$-.2238 \times 10^{-1}$
40 to 60	$-.1340$	$-.3453$	$.2992 \times 10$	$.1674 \times 10^{-1}$
60 to 80	$.3842 \times 10^{-1}$	$-.1907$	$.3015 \times 10$	$-.6900 \times 10^{-1}$
80 to 100	$-.1321 \times 10^{-1}$	$.1652$	$.2225 \times 10$.4851
100 to 120	$-.1227 \times 10^{-2}$	$.1926 \times 10^{-1}$	$.2761 \times 10$	$-.3800 \times 10^{-1}$
120 to 140	$.1193 \times 10^{-1}$	$-.3982$	$.7101 \times 10$	$-.1487 \times 10^2$
140 to 160	$.2652 \times 10^{-3}$	$.2003 \times 10^{-1}$	$.2344 \times 10$	$.1717 \times 10$
160 to 180	$-.7256 \times 10^{-2}$.5625	$-.1058 \times 10^2$	$.1036 \times 10^3$

Existing solar-lunar ephemeris programs (Project 0001; Problems 1131, 1461) were adapted, and output topocentric viewing angles as well as the phase and illumination at specified time intervals.

1.2 STELAZ and Polaris

Initiator: I.M. Hussey

Project No.: 0001

Problem No.: 4517

Given the mean place of a star at any epoch, e.g. 1975.0, January 0^d.978 in Right Ascension and Declination (α_0, δ_0); find the Apparent Right Ascension and Declination for any specified date and time by correcting for aberration (primarily stellar annual), precession, and nutation. For any geographic location (geodetic latitude, longitude, and altitude)

find the stellar azimuth and zenith angle corrected for refraction.
Obtain culmination and elongation angles and times for a selected star.

1.2.1 Functional Description

Following the "Explanatory Supplement to the Ephemeris" P. 150⁽¹⁾, the above three corrections are applied in the order specified. Annual parallax, proper motion, and orbital motion (of star) are neglected.

From apparent right ascension of station at U.T. hours and the geodetic latitude obtain the azimuth and unrefracted elevation. Correct for refraction, assuming station is near sea level. Upper and lower culmination angles and times occur for azimuth 0° and 180°, but not necessarily respectively. Linear interpolation is used. W and E elongations are determined from a parabolic fit to 3 points near the extrema.

NOTE: The spherical geometry calculations show negligible loss in accuracy even for nearly circumpolar stars. If declination >89.8° a warning message is printed.

Figure 1 shows a sample computer print-out for observation of four stars at 4 hour intervals. Daily culmination and elongation angles and times have been requested for Polaris and are also printed. Output is suppressed if the star is unobservable.

The program has been verified using epochs and mean places of stars from different annual editions of the American Ephemeris and Nautical Almanac, and against an earlier program which required transcription of the Pole Star Table from these Almanacs. Results are reproducible to a few tenths of a minute of arc.

1.2.2 Components

Reference Time and Coordinates:

$$D_{\text{oh}} : \text{Julian day at } 0^{\text{h}} \text{ UT} = 2442731.5 \text{ (example)}$$

$$Tu = (D_{\text{oh}} - 2415020.) / 36525.$$

$$TTu = Tu - .01 \times \text{AIN}T (Tu \times 100.)$$

$$\text{Mean R.A. of Greenwich at } 0^{\text{h}} \text{ UT}$$

$$\alpha_G = 6.645065 + 2400. \times TTu + .05126 \times Tu \text{ (hrs.)}$$

$$\Delta\alpha_G = 24.065710 \times (\text{UT}) / 24$$

$$DJ = D_{\text{oh}} + \text{UT} / 24.$$

STATION ID LATITUDE LONGITUDE ALTITUDE KMS H.F./M.F./Y.F MINC K
 AFCRL 42.45480 71.27110 .090 11 15 75 2 1 76 240 1

EPOCHS AND MEAN PLACES OF STARS SELECTED FOR AZ-EL TABULATION

	R1.ASC.	REF.	DEG.	STAR-IDENTIFICATION #
1	EFYR .E0A HR/MN/SE .C	DEG/P-N/SU		
	1975 .978 2 7	26.2	89 9 0	A URS MI (POLARIS) 1
	1975 .978 5 14	50.4	45 58 27	ALPHA AURIGA 2
	1975 .978 14 14	31.2	19 13 43	ALPHA BOOTES 3
	1975 .978 18 36 5.5	33 45 34	ALPHA LYRA (VEGA) 4	

CULMINATION AND ELONGATION ANGLES AND TIMES(UT) REQUESTED FOR A URS MI (POLARIS)

15

DATE (UT)	H.F. MN	AZIM.	REF.EL.	DEG.	ALPHA AURIGA		REF.EL.	DEG.	ALPHA BOOTES		REF.EL.	DEG.	ALPHA LYRA (V.		REF.EL.	DEG.
					DEG.	DEG.			DEG.	DEG.			DEG.	DEG.		
75 11 15 0 0	U = 43.315 AT	3.349	L = 41.630 AT	15.316	W = -1.142 AT	9.281	E =	1.142 AT	21.351							
75 11 15 0 0	• E88	43.006	44.773	25.239						-72.129	43.04					
75 11 15 4 0	-1.197	43.302	69.660	63.921						-40.939	6.26					
75 11 15 8 0	-1.078	42.756	-70.144	72.674												
75 11 15 12 0	-• E66	41.925	-55.165	32.674												
75 11 15 16 0	• 261	41.643	-24.110	4.205												
75 11 15 20 0	1.072	42.166	16.600	1.418												
75 11 16 0 0	U = 43.315 AT	3.283	L = 41.630 AT	15.250	W = -1.142 AT	9.215	E =	1.142 AT	21.245							
75 11 16 0 0	• 875	43.017	50.215	75.856						-71.672	42.35					
75 11 16 4 0	-• 217	43.300	69.803	64.603						-40.331	5.76					
75 11 16 8 0	-1.184	42.742	-70.252	71.930												
75 11 16 12 0	-• 853	41.915	-54.764	32.079												
75 11 16 16 0	.220	41.646	-25.490	3.924												
75 11 16 20 0	1.073	42.193	17.251	1.621												

Figure 1. STELAZ Output with Culmination and Elongation Angles for Polaris

$$d_c = D_{\text{oh}} + \text{UT}/24. - 2415020.0 \quad \left[\begin{array}{l} \text{from} \\ 1900 \end{array} \right] \text{Jan } 0.5$$

$$\& T = d_c / 36525.$$

$$D_{\text{epoch}} = \text{Julian day number for } 1975.0 \quad 0^d.978 \text{ (say)}$$

$$T = (D_{\text{epoch}} - D_{\text{epoch}}) / 365.2500$$

$$T = T - T/2.$$

The fundamental arguments Ω , ν and ϵ are available with sufficient accuracy from Reference 3, using the reference times determined above.

Aberration Correction

At any time, find ϵ the obliquity of the ecliptic and ν the longitude of the sun from the mean equinox of date. Constant of aberration $K = 20.47''$. Then, [from "Spherical Astronomy" by W.M. Smart, p. 184] (2)

$$C = -K \cos \epsilon \cos \nu$$

$$D = -K \sin \nu$$

$$c_\alpha = 1/15 \cos \alpha \sec \delta; \quad d_\alpha = 1/15 \sin \alpha \sec \delta$$

$$c_\delta = \tan \epsilon \cos \delta - \sin \epsilon \sin \delta; \quad d_\delta = \cos \epsilon \sin \delta$$

and apparent right ascension and declination is obtained from true right ascension and declination by:

$$\alpha_1 = \alpha + C c_\alpha + D d_\alpha$$

$$\delta_1 = \delta + C c_\delta + D d_\delta$$

Annual Precession Correction

$$m = 3^s .07234 + 0^s .00186 T$$

$$n = 20^s .0468 - 0^s .0085 T$$

$$= 1^s .33646 - 0^s .00057 T$$

where T is in tropical centuries from 1900.0.

Reduction from mean to apparent places:

$$\Delta \alpha_p = T(m + n \sin \alpha \tan \delta)$$

$$\Delta \delta_p = T(n \cos \alpha)$$

[evaluate at mean T over the period T years plus. frac.]

Nutation Correction

In Longitude

$$\Delta \psi = -17''.2327 * \sin(\Omega)$$

In Obliquity

$$\Delta \epsilon = 9''.21 * \cos(\Omega)$$

where

$$\begin{aligned}\Omega &= \text{Longitude of moon's ascending node} \\ &= .71995354167 - .000147094228332 d_c (1 - .2941759 \times 10^{-15} d_c) \\ &\quad \text{revolutions.}\end{aligned}$$

where $d_c = \text{Julian day number} - 2415020.0$
 $[1900.5 \text{ ET}]$

$$\begin{aligned}\Delta\alpha_n &= (\cos \epsilon + \sin \epsilon \sin \alpha \tan \delta) \Delta\psi - \cos \alpha \tan \delta \Delta \epsilon \\ \Delta\delta_n &= \sin \epsilon \cos \alpha \Delta\psi + \sin \alpha \Delta \epsilon\end{aligned}$$

1.2.3 Procedure

Apparent (corrected) R.A. and Declination:

$$\alpha_1 = \alpha_0 + C c_\alpha + D d_\alpha$$

$$\delta_1 = \delta_0 + C g + D d_\delta$$

$$\alpha_p = \alpha_1 + T(m + n \sin \alpha_1 \tan \delta_1)$$

$$\delta_p = \delta_1 + T(n \cos \alpha_1)$$

$$\begin{aligned}\alpha &= \alpha_p + (\cos \epsilon + \sin \epsilon \sin \alpha_p \tan \delta_p) \Delta\psi \\ &\quad - \cos \alpha_p \tan \delta_p \Delta \epsilon\end{aligned}$$

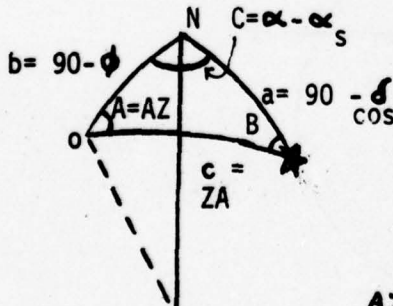
$$\delta = \delta_p + \sin \epsilon \cos \alpha_p \Delta\psi + \sin \alpha_p \Delta \epsilon$$

Apparent R.A. of station at UT(hrs.)

$$\alpha_s = 0.9174 * \Delta\psi * \frac{\text{hr}}{\text{sec}} + \Delta\alpha_G + \alpha_G - \text{GLONW} * \frac{\text{hr}}{\text{deg.}}$$

Unrefracted Azimuth and Zenith Angle:

Observer station orientation on the celestial sphere: α_s , ϕ (geodetic latitude).



Find Zenith Angle from

$$\cos c = \cos a \cos b + \sin a \sin b \cos C$$

$$\text{Then, } \sin A = \sin C \frac{\sin a}{\sin c}.$$

$$\text{& } \cos A = \frac{\cos a - \cos b \cos c}{\sin b \sin c}.$$

$$AZ = \text{ATAN2}(\cos \delta \cos \phi \sin C, \sin \delta \sin \phi + \cos \delta \cos \phi \cos C)$$

where

$$ZA = \cos^{-1}(\sin \delta \sin \phi + \cos \delta \cos \phi \cos C)$$

1.3 Program ECLPLOT

Initiator: J. Aarons

Project No.: 4643

Problem No.: 4844

Program ECLPLOT was designed to depict the local eclipse circumstances for any solar eclipse and any observational station, at selected time intervals.

1.3.1 Functional description

Program ECLPLOT uses punched output of program ECLPT which includes exposure fraction EXP for every time step as well as semi-diameter of the sun SDS, semi-diameter of the moon SDM, angular distance ANGDIS and position angle POSANG of the moon relative to the sun, and position of the sun's axis PSAXS. (Project 0001, Problem 3501)

Based on this information program ECLPLOT produces plots which depict the progression of the eclipse and also indicates north and sun-axis directions. The sun-moon center line is always horizontal to allow a large uniform plot scale of 1 inch for 5 secs of arc.

1.3.2 Procedure

Figure 2 shows a typical eclipse configuration and identifies the variables described above.

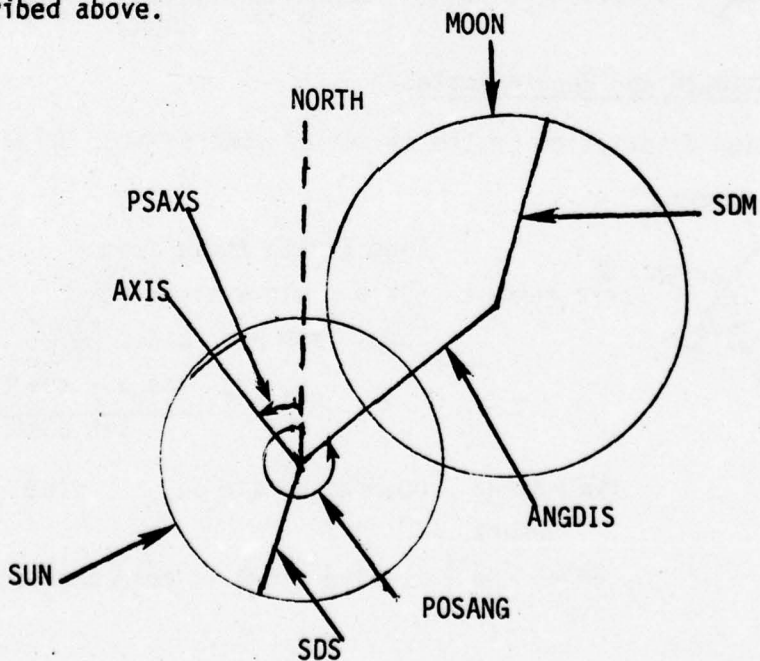


Figure 2. Solar Eclipse Viewing Geometry

Punched card output and format is as follows:

IYR, IMO, IDA, IHR, IMN, EXP, SDS, SDM, ANGDIS, POSANG, PSAXS

Format (5(I2,IX),6F10.7)

Exposure EXP is a fraction (1-obscurcation). Others, SDS to PSAXS, are in radians. Figure 3 shows a typical plotted output.

1.4 Program SOLPLT

Initiator: G. Best

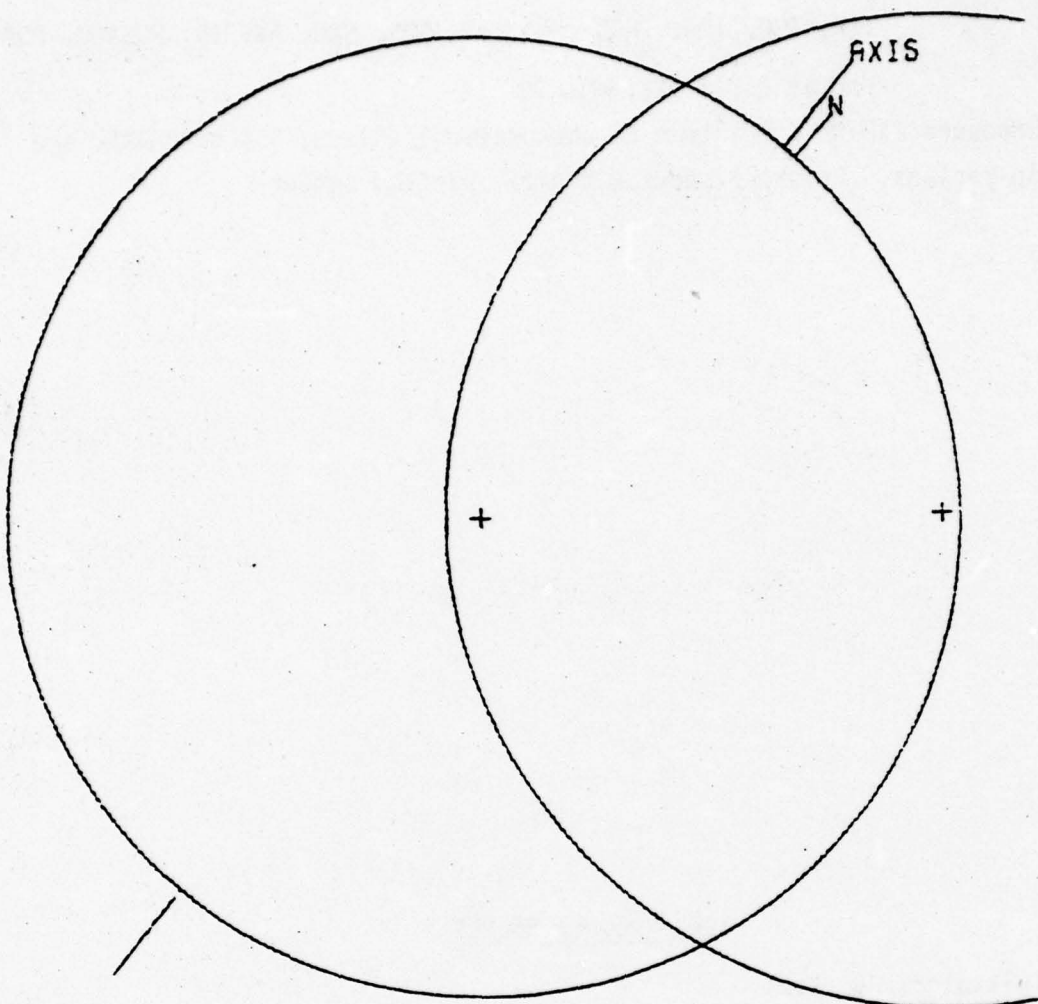
Project No.: 7635

Problem No.: 4824

In planning rocket launches or other experiments depending on sunrise, sunset or twilight, it is useful to have plots on which these times are given for a whole year for a specified location. These plots can be made even more informative by also including times of moonrise and moonset.

The Solar and Lunar Ephemeris programs previously developed and modified under project 0001, Problem Nos. 1131 and 1461 were adapted for this problem. Certain refinements also make this SOLPLT program more up-to-date than the original programs.

1.4.1 Functional Description



5' of arc = 1 inch

EXP=0.5607 UT= 2010
HAMILTON

Figure 3. ECLPLOT Output for Solar Eclipse of July 10, 1972

Program SOLPLT determines times of specific elevation and/or depression angles of sun and/or moon for any location. A tabulation and a file of daily values is created, and a plot of graphs to depict these conditions is produced.

Program SOLPLT uses program SOLLUN⁽⁴⁾ as a principal subroutine which generates, as a function of the universal time, the hour angles, azimuth, declination and elevation of the sun and the moon for any station location. Program SOLPLT uses the above subroutine to determine local standard times for specified elevation and/or depression angles for the sun and the moon. Some refinements to the original programs were incorporated. Double precision is not required on the CDC-6600 and has been eliminated. The correction for ET-UT is calculated by default as (KYR-1929) secs. All parts of the separate solar and lunar programs have been recombined into the original order (parts A-M). Refraction correction and librations of the moon (part M) are not used. As input, program SOLPLT requires only the coordinates of the station, the desired values of the elevation and/or depression angles and the year of observations. In order to obtain local standard time values, the applicable standard time longitude must also be input. Note that for angles equal to zero the times of sun/moon rise and set will be produced.

Subroutine LORAN uses values obtained by SOLPLT to produce plots of elevation angle times which are represented by solid lines and depression angle times which are represented by broken lines. The plot covers a full year. Figure 4 shows typical plots where the solar elevation angle contours are 20° apart.

1.4.2 Mathematical or Logical Procedures

To calculate the time for the specific elevation angle the following procedure was developed. For every day of the specified year the standard time monotonically increases starting from zero. Using spherical trigonometry formulae one calculates the minimum earth rotation and corresponding increment in standard time to step from one specified angle to the next. Standard time should increase monotonically but allowance is made for small negative increments to avoid possible skipping of angles.

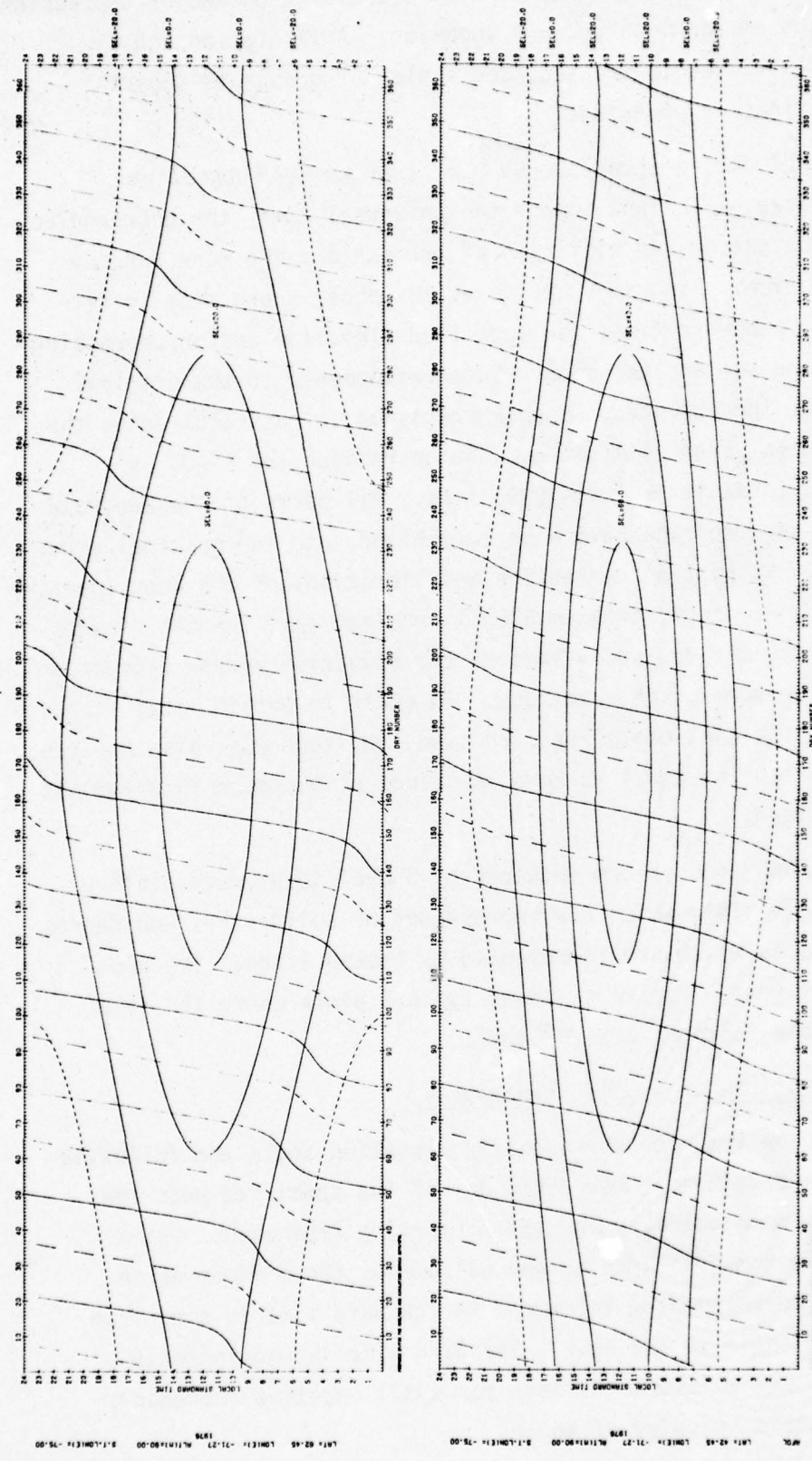


Figure 4. Solar Elevation and Moon Rise-Set Plots for 1976 at AFGL and 200 further North

For elevation angles of the moon the program uses the same procedure as for the sun, with subroutine SOLLUN providing elevation and hour angles of the moon.

Whereas rising solar elevations always occur between 0 and 12 hours local time, and dropping elevations after 12 hours, this property cannot be used for the moon. Instead, a test for increasing or decreasing moon elevation is made. If the first time corresponds to a decreasing elevation, the moon set and rise times for the day are swapped.

References

- (1) Explanatory Supplement to the Astronomical Ephemeris, H.M. Stationery office, London, 1961.
- (2) Smart, W.M., Textbook on Spherical Astronomy, Cambridge University Press, Cambridge, 1960.
- (3) Williams, Jr., Wentworth, "Predictiton and Analysis of Solar Eclipse Circumstances", AFCRL Report No. 71-0049, March 1971.
- (4) Hussey, I.M., "Generation of Solar and Lunar Ephemeris", AFGL/SUA Project No. 0001, Problem Nos. 1131, 1461.

Section 2. Arctic Ionospheric Research

2.1 Program ISOZEN

Initiator: J. Buchau

Project No.: 7663

Problem No.: 4714

ISOZEN plots contours of constant solar zenith angle for any 90° polar segment of the Northern Hemisphere. The contours are mapped in either geodetic or geomagnetic coordinates, and are designed to be used with an AFGL world-map overlay. Figure 1 and 2 are examples of such plots for different quadrants.

2.1.1 Functional description

For a given date, time, quadrant and coordinate system, (geodetic or geomagnetic), ISOZEN produces a 10" one-quadrant plot of constant zenith angle, each contour being separated by 5° , and drawn as a solid or dashed line, solid for less than 90° , dashed otherwise. The present version allows one to step the time by a given increment, thereby generating several plots in one run.

2.1.2 Mathematical & Logical Procedures

The solar zenith angle, Z, (the angle between the local vertical and the position of the sun), is a function of latitude, longitude, and time.

$$Z = Z (\theta, \phi, T)$$

A contour of constant zenith angle for a particular time is given by the equation

$$Z_0 = Z (\theta, \phi, T_0)$$

where Z_0 and T_0 are given constants.

The following procedure was used to generate such contours, making use of some subroutines developed previously⁽¹⁾:

A search is initiated along one of the quadrant boundaries for desired contour values. When one is found, either θ or ϕ is stepped away from the boundary, and a Mueller's iteration technique, using the subroutine SOLUN to evaluate Z, is used to find the other coordinate (ϕ or θ).

This procedure, analogous to a blind man's use of his cane to navigate crosstown, is repeated until another boundary is encountered, thereby completing this particular contour. The intersection is catalogued to avoid redundant plotting, and entire sequence repeated until all contours have been mapped. The transformation from geodetic to geomagnetic coordinates, if required, is effected by the subroutine CGINV.

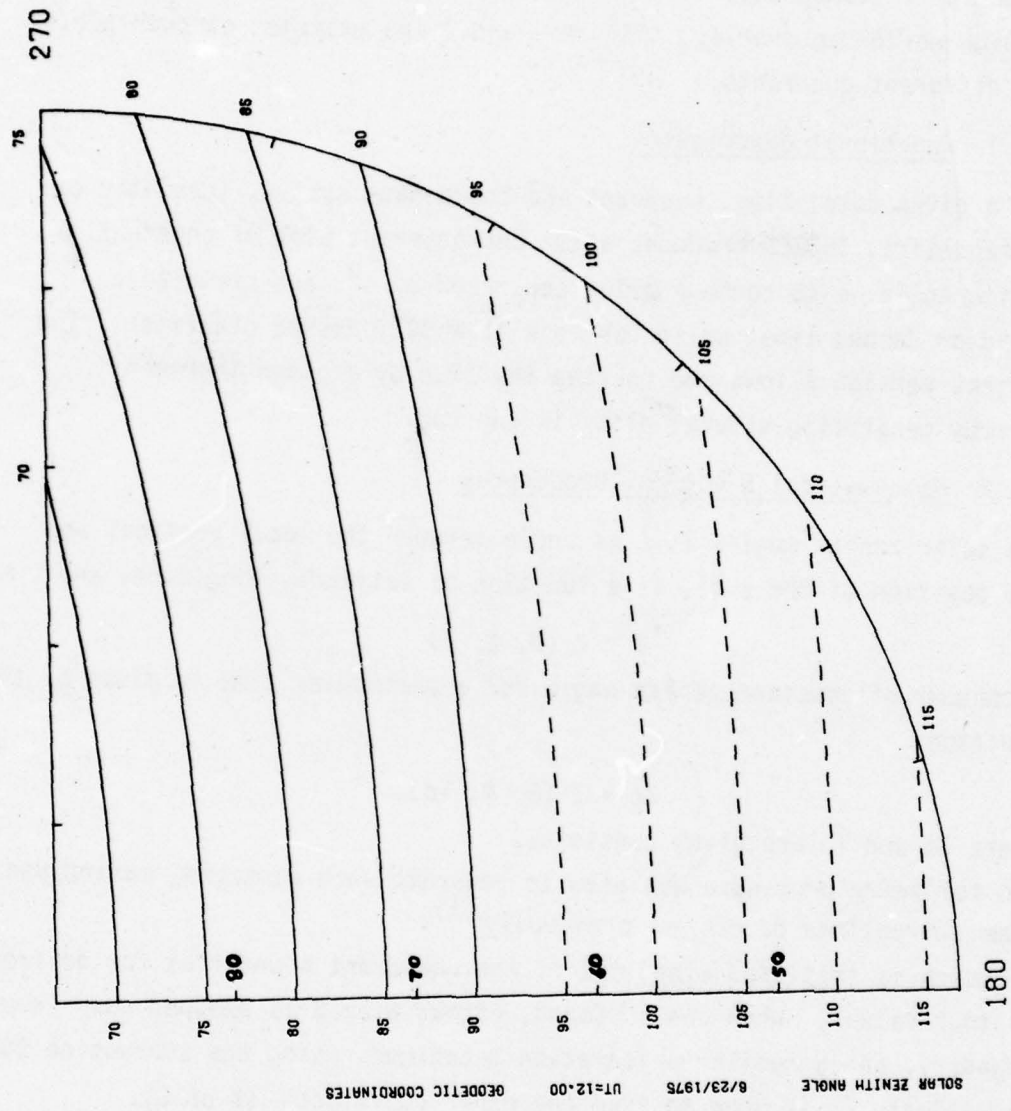
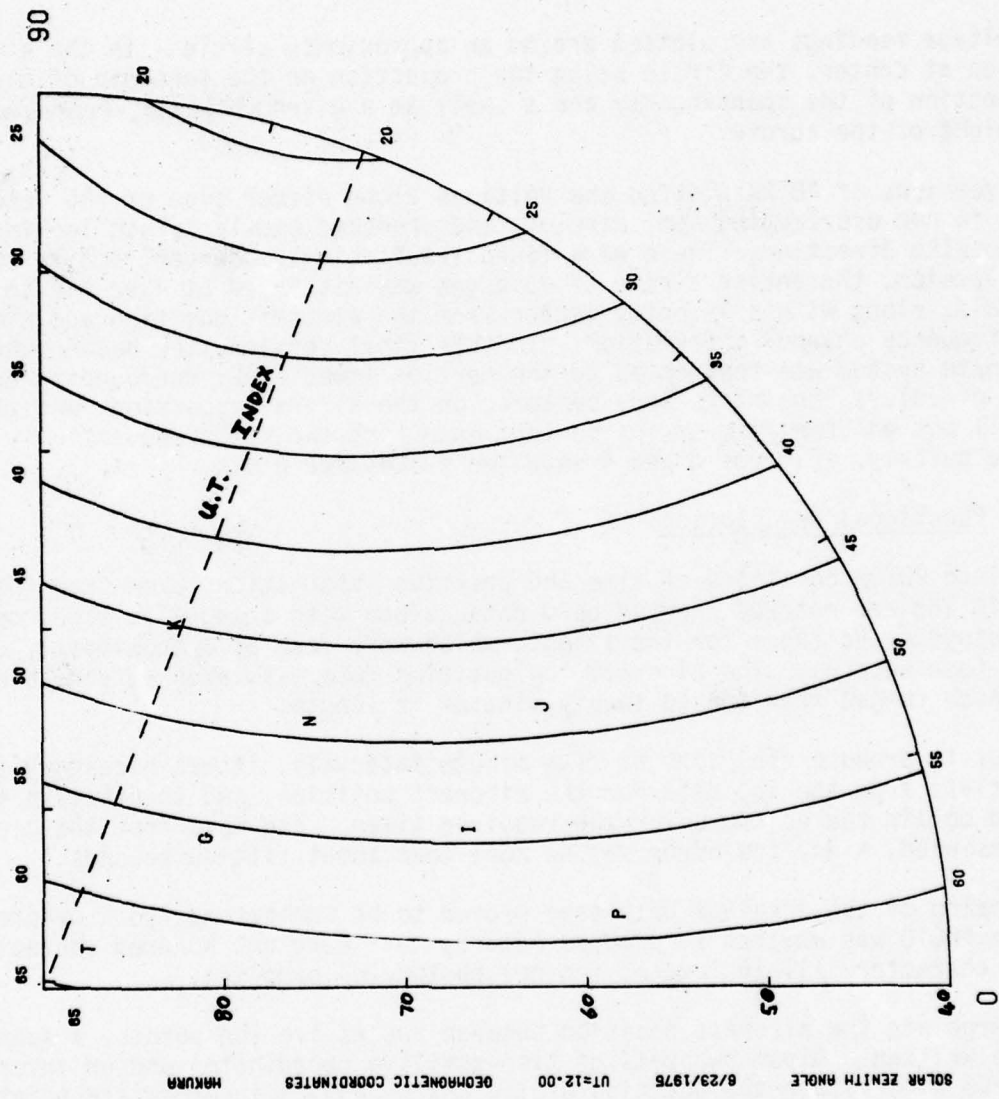


Figure 1. Iso-zenith Angle Contours in Geographic Coordinates for 180-270°

Figure 2. Iso-z zenith Angle Contours in Geomagnetic Coordinates for 0-90E
Locations of selected stations are identified by letters.



2.2 Photometric Data Presentation

Initiator: J. Buchau
Project No.: 5631

Problem No.: 4605

Program PDTRK is essentially a plotting program to display voltage readings from an aircraft mounted 360 degrees scanning photometer along the projection on the spheroid of the aircraft flight path, all in a corrected geomagnetic polar coordinate system.

The voltage readings are plotted around an approximate circle with the aircraft position at center, the circle being the projection on the spheroid of the intersection of the scanning ray and a shell at a given altitude, representing the height of the aurora.

Early versions of PDTRK plotted the voltages along either side of the velocity vector in non overlapping semi circles, and produced similar plots looking in the opposite direction. These were found insufficient, however, and in the final version, the entire circle of voltages was displayed at five minute intervals, along with a velocity vector from the aircraft position and time/date/frequency channel information. In this final version, the background coordinate system was restricted to the portion immediately surrounding the circle of values, the plots were centered on the aircraft position, and they were all put on 35mm film strips so that examining the plots sequentially could be done quickly. Figures 3 and 4 show two successive plots.

2.2.1 Functional Description

Input into PDTRK consisted of time and position information taken from the aircraft log and entered punched card data, along with a magnetic tape containing the photometer voltages for the flight, which were read at approximately every thirty-four seconds. The aircraft log position data was taken at variable intervals which ranged from ten to twenty minutes in length.

In order to produce the plots at five minute intervals, it was necessary to interpolate from the log data for the aircraft position, and to position the data tape to obtain the voltages for the required times. The data from the closest time was used, since the error was no more than about fifteen seconds.

Positioning of the original data tape proved to be cumbersome, so a preprocessor program PHOTO was written to produce records that were one hundred characters plus 8 character fill in length, ten per photometer sampling.

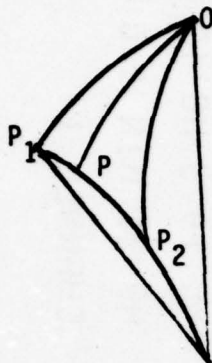
To interpolate the aircraft position between successive log points, a subroutine POS was written. Given two sets of time-positive coordinates and an intermediate time, POS will return the position of the corresponding intermediate point on the great circle between the given points, assuming a constant velocity over the entire interval.

To find the projection of the photometer ray and the aurora, program SAP was employed. CORRGM2 converted geographic coordinates to corrected geomagnetic coordinates. SAP and CORRGM2 are described elsewhere⁽¹⁾

2.2.2 Mathematical or Logical Procedures

Subroutine POS is essentially the solution of two spherical triangles.

In the diagram the first application is to the triangle P_1OP_2 , where P_1, P_2 are the given points, O is the pole and OP_1, OP_2 are co-latitudes, to obtain P_1P_2 and the spherical angle OP_1P_2 . P_1P is obtained by a simple ratio since velocity is constant, and then the spherical triangle OP_1P is solved to obtain OP , the new co-latitude and P_1OP , the longitude increment.



To produce the restricted background plot, we obtained the limits of the polar coordinates of the projected number field, and chose convenient latitudes and longitudes to enclose the figure. The direction arrow was added, and the rectangular coordinates for plotting were corrected by the coordinates of the aircraft position to center the plot on the aircraft.

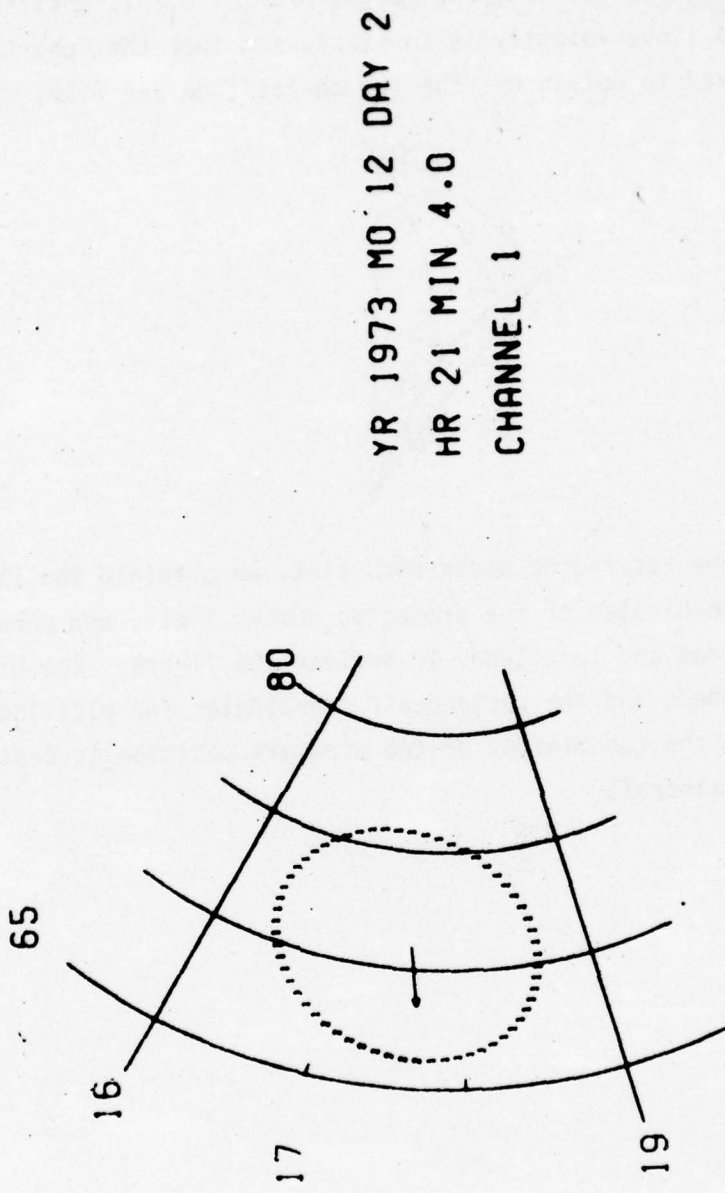


Figure 3. Photometer Reading Projection-Restricted Background

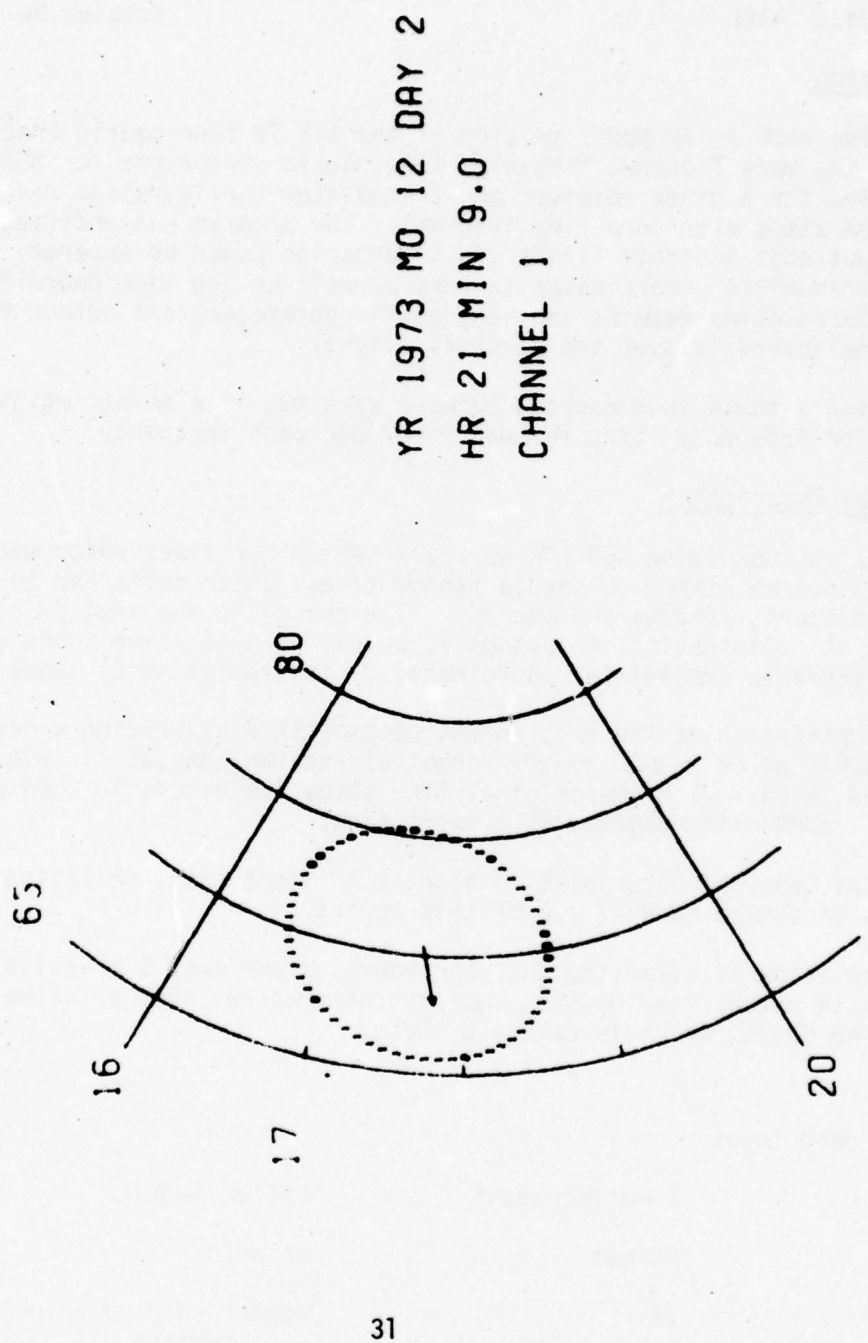


Figure 4. Photometer Reading Projection-succeeding Time

Section 2.3 DAASM Flight Program

Initiator: J. Videberg
Project No.: 414L

Problem No.: 4693, 4748

Introduction

In the Blue Deck Polar Model version of the ITS 78 Ionospheric Predictions Program, the mode 7 output tabulates ionospheric parameters for MUF and selected frequencies for a given receiver and transmitter configuration repeating at designated steps over some time interval. The program was modified so that in this output mode aircraft flight log information could be entered, effectively causing transmitter coordinates to vary as well as the time coordinate. Then using interpolation methods the ionospheric parameters are output for selected equal time intervals over the aircraft flight.

In addition a table is presented between each two time points which summarizes the Doppler frequency shift for each mode and each frequency.

Functional Description

The calls to subroutine CGMTIME were all set up for times which were integral hours. Since we wished to handle random times, these calls had to be reworked to permit hours, minutes and seconds. The change to the program essentially involved a) eliminating the automatic hourly integral time increments b) permitting variable transmitter coordinates c) interpolating d) summarizing Doppler.

The reorganization of the program was accomplished by writing a new main program, called NUMAN which reads input information and reorganizes it into files called TAPE2 and TAPE3. With the original time steps inhibited, it then calls the original BDPM main program, as a subroutine.

NUMAN also does the interpolation along the flight path, utilizing subroutine POS, which is discussed in sec. 2.2 of this report.

Upon completion of outputting the ionosphere parameters, BDPM calls subroutine OUTS, which outputs the Doppler summary information. The printing is done by subroutine SUBPR, which is called by OUTS.

INPUT

card input

cd 1	Time increment	Doppler Summary
cc	Format	Contents
1-5	I5	Time
6-10	I5	Doppler summary selector
		0--no summary
		1--summary
cd 2, 3	Transmitter and receiver antenna cards, as described in ESSA TECHNICAL REPORT ERL 110-ITS 78 (denoted henceforth as ETR)	
cd 4	99 in cc 7-8.	
cd 5	Month and Sunspot card (see ETR)	

cd 6 -1 in cc 4-5

cd 7 } Program control cards (see ETR)
cd 7+k }

cd 8+k 99999 in cc 1-5

cd 9+k Frequency complement card (see ETR)

cd 10+k Circuit card (see ETR)

cd 11+k Flight time-position cards

cc	format	contents
1-5	I5	Universal time-hrs(integer)
6-10	F5.0	Universal time-min(decimal)
cd 11+k+1	11-15	Latitude-deg. (integer)
16-20	I5	Latitude-min (integer)
21-25	I5	Longitude-deg. (integer)
26-30	I5	Longitude-min (integer)

cd 12+k+1 1000 in cc 2-5.

Tape input

- 1). Tables for geographic-geomagnetic coordinate conversion.
- 2). Numerical coefficients for various ionospheric layers as described in ETR.

OUTPUT

- 1). Mode 7 output as described in ETR with varying transmitter coordinates.
- 2). Doppler summary table (see Fig. 5). For each mode-frequency box, in printed beginning time delay, ending time delay, difference, and Doppler frequency shift.

JOB CONTROL

Organizing the modified program so that the input could be read as called for by the subroutine was accomplished by job control cards.

The coordinate conversion tables were on a mass storage permanent file, as were the coefficients. With the former designated BDAT, and the latter BDPDA, and the binary program file as BPR, the following job control was used.

```
ATTACH, BB, BPR, ID= ---.  
ATTACH, TAPE 9, BDPDA, ID= ---.  
ATTACH, CC, BDAT, ID= ---.  
COPYCR, CC, EE.  
COPY CR, INPUT, EE.  
REWIND, EE.  
COMBINE, EE, FF, 2.  
BB, FF, PL=77777.
```

Figure 5. Doppler Summary Table for 5 Minutes of Flight Time

2.4 ISIS-2 Data Base

Initiator: C. Pike
Project No.: 7663

Problem No.: 4604

Three magnetic tapes containing ISIS-2 satellite soundings of electron density profile versus height were received from the Canadian Communications Research Center and were reduced, sorted and merged into one data base tape for subsequent research at AFGL. The tapes were converted from 9 track, 800 bpi EBCDIC format to SCOPE 7 track 800 bpi, BCD format. The source tapes were in the "log_e (density)" format that was also used for the later Alouette I N(h) data. Program FIRSTFL had previously been developed for processing that data⁽¹⁾ and was modified to generate the ISIS-2 data base, including geographic, geomagnetic, and solar environmental information. Over 25,000 samples were obtained after rejection of between 1 and 2 percent because of various unacceptable data conditions. The electron density is provided at altitudes from 950 km to 350 km in steps of 100 km. For altitudes below H_{max} the electron density is entered as -9.99. Maximum electron density ED_{max} is replaced by f_0F2 according to $ED_{max} = 1.24 \times 10^4 (f_0F2)^2$. The data were time sorted except where the F5.2 format for UT did not provide enough resolution. The data covers 1970 thru 1973. Table 1 gives the format for the tape that was created.

Table 1. ISIS-2 Data

<u>Variable Description</u>	<u>Format</u>
ID (data source=11)	12
Year	12
Day Number (1-366)	13
UT (hours)	F5.2
Geog. Latitude	F6.2
Local Time (hours)	F5.2
Mag. Latitude	F6.2
Mag. Time (hours)	F5.2
Geog. Longitude- E positive	F5.1
Cosine of Zenith Angle	F6.3
Kp	F4.2
F10.7cm Solar Flux	13
Quality figure (4-very good, 9-very poor)	11
Altitude of Satellite (km)	I4
Elec. Dens. at Satellite $\times 10^{-4}$	F6.2
TOTALN $\times 10^{-11}$	F8.3
Elec. Dens. (950, 850....350) $\times 10^{-4}$	7F6.2
$f_0 F2$	F4.1
H_{max} (km)	F4.0

2.5 Auroral Morphology Study (Part II)

Initiator: R. Nadile
Project No.: 7670

Problem No.: 4689

Program AIMS, which provides a CRT plot satellite view of the aurora and also depicts boundaries, cross-sections, and solar aspect, (1) was modified for extended uses.

- 1.) A polar projection of the earth and auroral oval including a map of continental outlines was programmed. Intersection of aurora and satellite field of view is depicted, with contributions to a selected tangent height also shown.
- 2.) An improved sunline routine was developed to draw the terminator on these plots.
- 3.) The program was adjusted to also allow southern hemisphere auroral morphology studies.

2.5.1 Polar Projection

Figure 6 shows a typical CRT plot for a geo-stationary satellite with emission profile between 75 and 150 km as a function of altitude h given by:

$$V = HN \times e^{(1-HN/1.16)}$$

where

$$HN = (h - 75)/15.$$

The auroral oval is taken to extend uniformly between 61.5° and 73° N: geo-magnetic latitude.

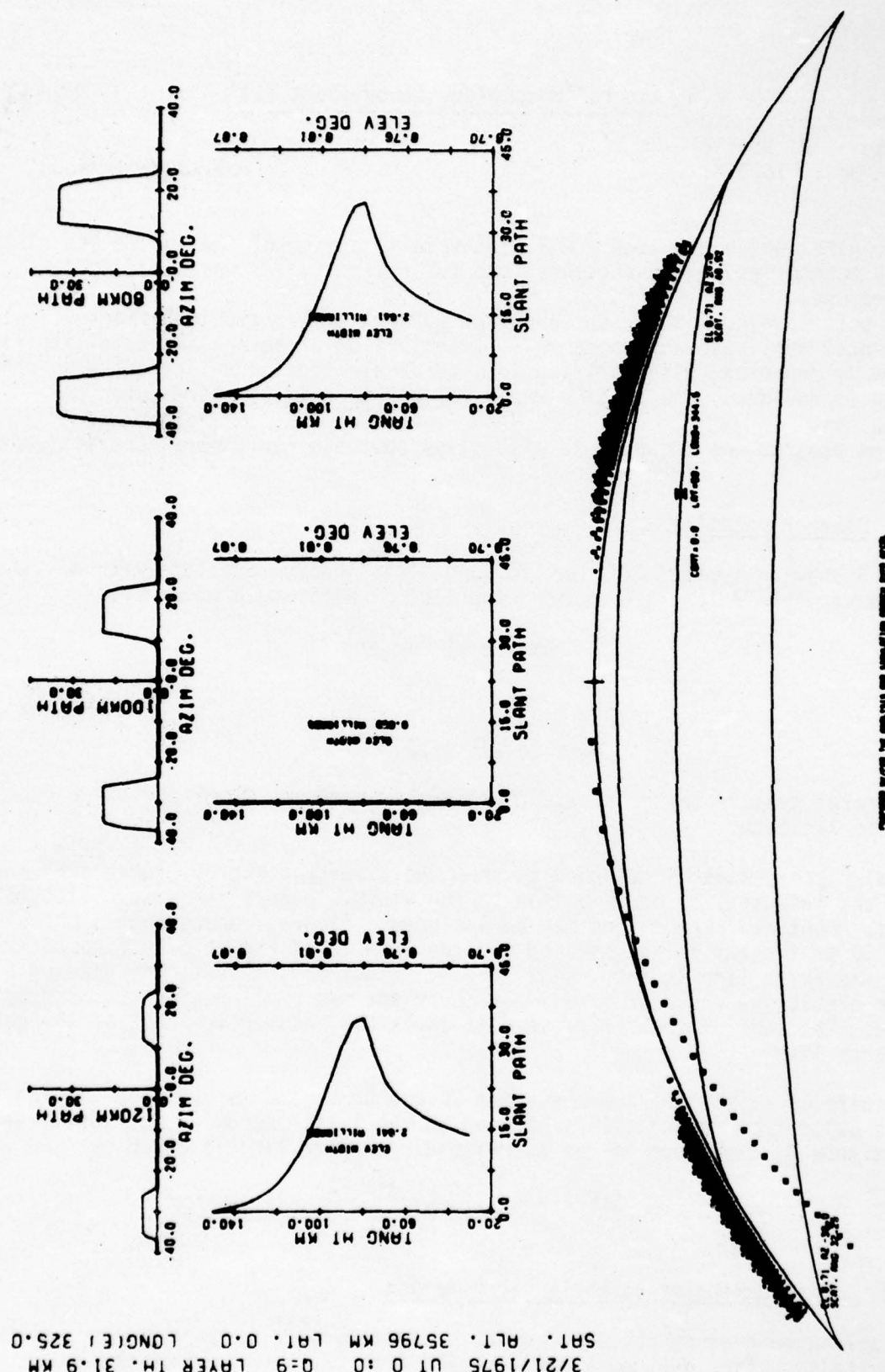
The polar projection is designed to show the viewing geometry, subauroral coordinates, and intensity of contribution to the visible aurora for a specified tangent height. Continental outlines may be included. Figure 7 shows such a CRT plot for a 30 km tangent height section for the example of Figure 6. Since 30 km above the earth limb is the lowest tangent height of interest, the shading at higher elevations would progressively cover the two small regions bounded by the aurora. The rest of the aurora remains invisible, either in front of or behind the earth limb.

The limits of azimuth AZ and elevation EL are converted to a dashed viewing line on the paper from the satellite located on the left. Assuming the satellite is at latitude θ , the slope of the corresponding dashed line is given by

$$\text{SLOPE} = - \frac{\tan EL \sin AZ}{\cos \theta + \tan EL \cos AZ \sin \theta}$$

2.5.2 Solar Terminator at Shell Layer Height

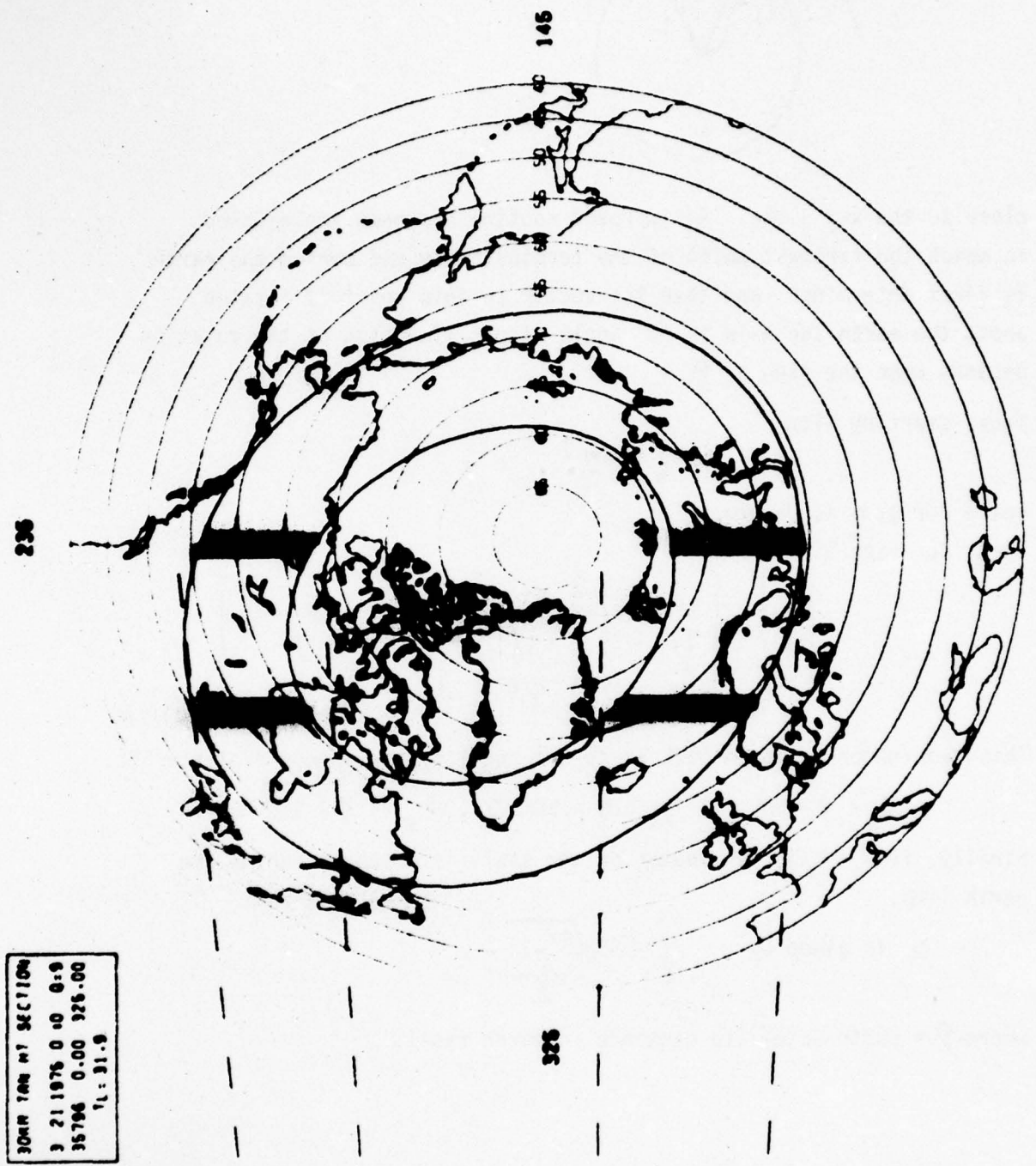
The sunline generating routine developed previously (1) moved the terminator on the earth's surface back by a distance SDL from the direction of the solar radius vector ξ_1, η_1, ζ_1 . In this satellite-oriented geocentric coordinate system, the x-axis is to the north, y to the east, and z passes through the satellite. Equal increments were taken in the x-direction and the terminator was solved for. Difficulties were occasionally encountered when the sun vector was

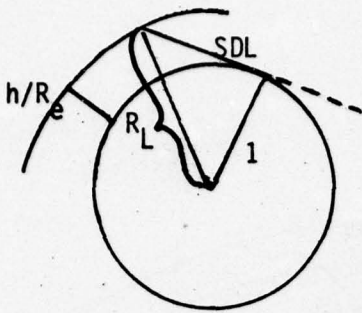


3/21/1975 UT 0 : 0 Q=9 LAYER TH. 31.9 NM
SLT. ALT. 35796 NM LAT. 0.0 LONGE! 325.0

Figure 6. Aurora View from a Geo-stationary Satellite for Selected Ionospheric Conditions

Figure 7. Polar Projection and 30 Km Tangent Height Contribution for the Study of Figure 6





close to the x-z plane. An improved routine has been implemented in which the farthest point of the terminator on and behind the earth is first determined, and then the vector to this point is rotated about the earth sun axis in 'D' angle steps. The sign of the rotation depends upon the sign of γ_1 .

Thus, starting with

$$\xi = -\xi_1^2 + \gamma_1^2 + \epsilon$$

solve for ξ, γ as before.

Then, for each step

$$\begin{bmatrix} \xi \\ \gamma \\ \zeta \end{bmatrix} = \begin{bmatrix} \xi_1 & (\xi_1 - \xi_1) \\ \gamma_1 & (\gamma_1 - \xi_1) \\ \zeta_1 & (\zeta_1 - \gamma_1) \end{bmatrix} \begin{bmatrix} 0 \\ \cos D \\ -\sin D \end{bmatrix}$$

This terminator is moved back on to the shell by the shadow distance SDL.

$$\xi_s = \xi - \text{SDL} \xi_1, \quad \gamma_s = \gamma - \text{SDL} \gamma_1, \quad \zeta_s = \zeta - \text{SDL} \zeta_1.$$

Finally, if $\xi_s < \xi$, the terminator on the shell is obscured behind the earth limb.

$$\xi_L \text{ is given by } \frac{1}{\rho} - \text{SDL} \sqrt{\rho^2 - 1}$$

where ρ = earth-satellite distance in earth radii.

2.6 Ionospheric Research Program Library UPDATE Tape

A group of programs that were developed over a number of years in support of ionospheric research, and that have some commonality either as regards use or subroutines were consolidated into an UPDATE program library. Operation consists of having a binary subroutine library available, created under EDITLIB, and compiling and executing only the requisite main program. The following programs comprise the present library:

	PROGRAM	USE
ALTRAK3 system	1) TRK2	Flight Tracks
	2) ALTRAK2	Satellite Tracks
	3) STATS	Statistics
	4) CON	Contour plots
	5) CGARC1	Auroral are plots
	6) AIMS	Auroral Morphology (Earth Limb)
	7) AIMSA	Auroral Morphology (Global)
	8) CONFMAP	DAPP - CGM grid
	9) WRLDMAP	Continental Outlines
	10) MJRECT	Rectangular Coord. CGM plot
	11) ABCD	Create Binary CGM file
	12) ISOZEN	Iso-zenith angle contours

These programs are described in an earlier report⁽¹⁾ or in the present one.

Reference

- 1) "Analysis and Programming for Scientific Research", Logicon, Inc., Final Report, AFCRL-TR-74-0480, September 1974.

Section 3. Rapid Orbit Prediction Program - ROPP

3.0 Rapid Orbit Prediction Program - ROPP

Initiator: I. M. Hussey

Project No.: 0001

Problem No.: 4506, 4801

For drag perturbed orbits analytic perturbation theory excluding short period oscillations is used in program ROPP with large step sizes to provide reasonably accurate and rapid prediction of the orbit elements.⁽¹⁾ This program was modified to include additional features:

- 1) Estimation of the ballistic coefficient $C_D A \over M$ relative to the atmospheric density model based on two sets of elements.
- 2) Input and output of the osculating position and velocity vector.
- 3) Altitude, perigee-apogee, eclipse in-out times, revolution number information, and apogee-perigee plot file.

The present program typically outputs parameters 1-4 times per second on the CDC6600. For example, a low altitude satellite run with print-out every 12 hours executes 1-2 days' of orbit per second.

3.1 $C_D A \over M$ Optimization

Program ROPP was designed to provide an approximate satellite ephemeris and life-time, given elements and drag factor at any epoch. For the drag model the geomagnetic and solar flux activity are required as well as the ballistic coefficient $C_D A / M$ where C_D is the drag coefficient and A / M is the area to mass ratio. For satellites at significant-drag altitudes the mean motion and resulting in-track error is extremely sensitive to inaccuracies in the atmospheric density model or, what is essentially the same thing, the ballistic coefficient. Given two sets of elements plus revolution number, reasonably separated in time, $C_D A / M$ may be adjusted in ROPP to cause the true anomaly to correspond closely to that of the second element set. The semi-major axis (A), eccentricity (E), inclination (I), argument of perigee (W or 0), and ascending node (N) are slowly changing elements, so that great confidence can then be placed in the trajectory between the element times and for a considerable period beyond.

The main problem in implementing this optimization procedure is in computing the cumulative angular rotation from the first element set to the second. After a few weeks the average mean motion is unable to predict the right revolution number.

It is thus necessary at each incremental output time to correct the cumulative angular rotation obtained from the mean motion and rate of change of argument of perigee, so as to match the true anomaly obtained from the elements at that time. This integration can then be safely continued up to the second set of elements. The procedure is described below:

Let I be any intermediate time, and X the next incremental time. Let 1 and 2 denote the initial and final element sets and times.

Notation:

N - rev. number

v - true anomaly

w - argument of perigee

\dot{w} - rate of change of w

MM - mean motion

AT - cumulative rotation from equator crossing preceding initial elements by $(v_1 + w_1)$.

a) If ATX is the cumulative rotation at time X the corresponding revolution number is given by $NX = NA + \text{INT}[(ATX/360)]$ (1)

Where $NA = N1 - \text{INT}[(v_1 + w_1)/360]$ (2)

NA gives the base revolution number to be added to any subsequent calculation to give the correct rev. number.

b) Compute rotation increment for interval Δt from I to X

$$\text{Estimate } \Delta A = \left(\frac{MMI+MMX}{2} \right) \Delta t + \left(\frac{\dot{w}_I+\dot{w}_X}{2} \right) \Delta t$$

$$\text{Calculate } ATX = ATI + \Delta A$$

Adjust ATX to match $(v_I + w_I)$ to the closest 360° .

c) This ATX becomes ATI for the next step; continue for each increment t until time 2 where we get AT2, the predicted revolution number

$$NT = NA + \text{INT}(AT2/360) \quad (3)$$

$$\text{and the predicted total rotation } \Delta AT = AT2 - ATI. \quad (4)$$

d) Calculate actual rotation DAT from time 1 to time 2.

$$DAT = (N2-N1) \times 360 + \text{MOD}(v_2+w_2, 360) - \text{MOD}(v_1+w_1, 360) \quad (5)$$

Finally, error between observed and computed rotation is

$$\text{Error} = DAT - \Delta AT \quad (6)$$

If the error is positive $C_D A$ must be increased. Successive iterative experiments
 $\frac{M}{M}$

with $C_D A$ adjusted also provide the rotational change sensitivity to these ad-
 $\frac{M}{M}$

justments, thus allowing a rapid convergence to the optimum ballistic coefficient. The procedure was implemented with subroutine CCDAM, and modification of existing routines including OUTSUB and READIN.

Figure 1 shows a typical computer output where $C_D A$ was optimized. The first
 $\frac{M}{M}$

element set is entered in the normal way and is now shown. The NAMELIST input is also standard⁽²⁾, except that the optimization procedure is initiated by setting both CD and CDAM to zero. The second element set is shown entered as a position-velocity vector after the \$END card. Iteration 0 provides a crude first estimate for CDAM based on a mean motion that has increased from time 1 to time 2. Three subsequent trajectory iterations are shown before a close enough match is obtained to the nodal period. The final ROPP prediction run with output is then made with CDAM=.04247 ft.²/lb.

3.2 Position and Velocity I/O

The basis for the addition of osculating position and velocity input - output was the gravitational perturbation model that exists in ROPP. Subroutine OSCSET generates comprehensive functions of eccentricity and inclination plus their derivatives. These are used by subroutine OSCHSUB to compute osculating Kepler elements. Conversion between these elements and position-velocity is a standard procedure⁽³⁾ and was implemented with subroutines ELMTPV and PVTELM⁽⁴⁾. Conversion from osculating to mean Kepler elements was added into PVTELM as an iterative procedure where the mean elements are corrected by the difference between the desired and resulting osculating elements. Four iterations including OSCSET recalls are sufficient for convergence. The mean Kepler elements in Figure 1 were derived in this manner from SCF position-velocity elements.

Figure 2 shows the normal full output, in this case twice a day. The last two lines present osculating position and velocity which have been made consistent with the original input due to the procedure described above.

3.3 Other Modifications

- a) Program ROPP was converted from double precision (RUN) to single precision (FTN) with negligible loss of accuracy. Core memory requirement was reduced by 30K octal, compilation time by 90 percent, and execution time by about 50 percent.

NHLST
\$INPUT
CD=0.,
COAM=0.,

DAY=1827.,

PRINT=10.,

AP=15.,

F10BA9=85.,

3END

COAM ITERATION NUMBER 0

POSITION-VELOCITY INPUT

8469.	76.43	0.019	957
3659.2414-5661.8549-2723.2481	-1.635816	1.314614	-7.029129

CONVERTED TO MEAN ELEMENTS (A,E,I,O,N,M)

1.13322	.083522	96.292435	105.323953	125.426531	86.490946
---------	---------	-----------	------------	------------	-----------

TSTART = .214278J, 5J0 J0C TEND = 21442829.500JU DAYS = 40.000000 REVINC = 561.00
OBS.ROT = .212230.31E+06 CALC.ROT = .20196147E+06 ERROR = 349.83 DEGS
COAM HAS BEEN CORRECTED FROM 5. TO GIVE COAM=.355248E-02

COAM ITERATION NUMBER 1

OBS.ROT = .2120+954E+06 CALC.ROT = .201722455E+06 ERROR = 324.40 DEGS

COAM HAS BEEN CORRECTED FROM .355748E-02 TO GIVE COAM= .605632E-02

COAM ITERATION NUMBER 2

OFS.ROT = .2120+56+E+06 CALC.ROT = .201752505E+06 ERFOR = 297.35 DEGS

COAM HAS BEEN CORRECTED FROM .695632E-02 TO GIVE COAM= .431201E-01

FINAL_COAM ITERATION FOLLOWS

Figure 1. ROPP C_DA/M Optimization for Elements 40 Days Apart

REF ID: A11474 FOR THE ANALYSIS AND SIMULATION SECTION (SUVAI) AIR FORCE GEOPHYSICS LABORATORY. TEL. 861-4161

RAPID ORBIT PREDICTION PROGRAM

PAGE 103

SATELLITE 0466

PERTURBATIONS PRESENT --- EARTH, MOON, SUN, DRAG

AUGUST 9, 1976

HOUR 0 MIN 0 SEC 0

REVOLUTION NO. 3490

TIME	J.D.=	2.642995000E+06	TIME - TO	0.020000000E+02	STEP SIZE	0.000000000E+00
A	KM=	7.1830465941E+03	E	=	7.905379665E+02	I
OMEGA	DEG=	2.715214153E+02	NODE	0.00	2.536906472E+02	MEAN
A DOT	KM/DAY=	-1.429071415E-01	E DOT	1/DAY=	-2.4509618376E-05	I DOT
OMEGA DOT	DEG/DAY=	-3.1734E-04	NODE DOT	DEG/DAY=	7.2630640795E-01	MEAN DOT
OSC A	KM=	7.1761366470E+03	OSC E	=	0.1971831927E-02	OSC I
OSC CHESSA	DEG=	2.7343F61920E+02	OSC NODE	DEG=	2.5369070364E+02	OSC MEAN
LATITUDE	DEG=	8.3724744E+01	E. LONGITUDE	DEG=	2.1912249235E+02	ALTITUDE
MAG.	LAT.	7.742692E+02	MAG. LONG.	DEG=	1.1747226197E+02	GEOD. LAT.
THETA G	DEG=	3.176117450E+02	LAMBDA N	DEG=	6.1456866984E+01	UNUSED
ALT. ERG.	KM=	2.578219425E+02	RAD. PRG.	KM=	6.641906603E+03	L.T. PRG.
ALT. APG.	KM=	1.3939619130E+03	FAD. APG.	KM=	7.7511065959E+03	L.T. APG.
TIME PRG.	J.D.=	2.64299944E+06	LAT. APG.	DEG=	-8.2927457923E+01	E. LONG. PRG.
TIME APG.	J.D.=	2.642999500E+06	LAT. APG.	DEG=	0.2827457923E+01	E. LONG. APG.
ECLIPSE TIME	MIN=	2.350000000E+01	ECLIPSE IN	HRS=	0.0933333333E-01	ECLIPSE OUT
XPOS	KM=	-8.2920677656E+02	YPOS	KM=	1.0160017599E+02	ZPOS
XNUT	KM/SEC=	1.9165681277E+00	YDOT	KM/SEC=	6.5930769478E+00	ZDOT
						200T
						KM/SEC= 9.2337027752E-02

AUGUST 9, 1976 HOUR 12 MIN 0 SEC 0 REVOLUTION NO. 3497

TIME	J.D.=	2.643000000E+06	TIME - TO	0.025000000E+02	STEP SIZE	0.000000000E+00
A	KM=	7.182975E+03	E	=	7.907169099E+02	I
OMFGA	DEG=	2.7192101973E+02	NODE	DEG=	2.5405379665E+02	MEAN
A DOT	KM/DAY=-1.417368398E-01	E DOT	1/DAY=-2.280394453E-05	I DOT	DEG/DAY=-8.405095343E-05	DEG/DAY=
OMFGA DOT	DEG/DAY=-3.173650450E+00	NODE DOT	DEG/DAY=	7.2632237216E-01	MEAN DOT	DEG/DAY= 5.1307745031E+03
CSC A	KM=	7.1615201677E+03	OSC E	=	7.939712650E-02	OSC I
OSC OMFGA	DEG=	2.7227460871E+02	OSC NODE	DEG=	2.5405625297E+02	OSC MEAN
LATITUDE	DEG=	5.2366577756E+01	E. LONGITUDE	DEG=	3.012960339E+02	ALTITUDE
MAG. LAT.	DEG=	6.3455718652E+01	MAG. LONG.	DEG=	1.807348135E+02	GEOD. LAT.
THETA G	DEG=	1.3410156872E+02	LAMBDA N	DEG=	2.695431392E+02	UNUSED
ALT. PRG.	KM=	2.5719631526E+02	RAD. PRG.	KM=	6.6150060389E+03	L.T. PRG.
ALT. APG.	KM=	1.3938175179E+03	PAD. APG.	KM=	7.0501955E+03	L.T. APG.
TIME PRG.	J.D.=	2.6429999570E+06	LAT. PRG.	DEG=-8.352986442E+01	E. LONG. PRG.	DEG= 2.0338753E+02
ECLIPSE TIME	MIN=	2.300000000E+01	ECLIPSE IN	HRS=	1.260333333E+01	ECLIPSE OUT
XPOS	KM=	6.2805189296E+02	YPOS	KM=	4.6100253051E+03	ZPOS
XNUT	KM/SEC= 1.9428022065E+00	YDOT	KM/SEC= 5.0189198195E+00	200T	KM/SEC= 5.0189198195E+00	200T

Figure 2. Full ROPP Output Sample

- b) Element input may be ADC 2-card or 5-card sets (see Section 4.1) or SCF position-velocity data. These capabilities parallel program LOKANGL.
- c) When using $\frac{C_D}{M}$ optimization, if the desired time span for the trajectory is not input, the program operates between the times of the two sets of elements.
- d) Mean satellite altitude is included with latitude and longitude output.
 If R is the mean radius vector and θ the latitude of the satellite, the altitude of the satellite H_s is given by

$$H_s = R - a_e \sqrt{1 + \frac{(2f - f^2)}{(1-f)^2} \sin^2 \theta}$$
 where a_e is the equatorial radius of the earth, and f is the earth flattening.
- e) Local times at perigee and apogee are included in the output, and are readily derived from existing quantities.
- f) Universal times of entry into and exit from solar eclipse are included along with the eclipse duration, for a period close to the requested output time.
- g) Revolution number at any time is calculated according to Equation (1) of Section 3.1, and is output.

h) Optional Apogee-Perigee Plot File

If a '1' is punched in column 71 of the first card of the first element set, apogee-perigee information is written on TAPE7 in punched card format compatible with program PLOTIT (see Section 5.2). This output is described in Table 1. Figure 2 in this Section is part of the run for satellite 8468 which subsequently produced the apogee-perigee plots of Figure 1 in Section 5.

In another application, mean elements from ROPP were punched out periodically to study disparities with mean elements provided by ADC. Results of this study are discussed in Section 4.3.

3.4 Problems with ADC and SCF Elements

A number of problems were identified during the use of the orbit prediction pro-

Table 1. ROPP Apogee-Perigee Output Description

VAR.#	VAR.	UNITS	FORMAT	CARD COL.
1	Day No.		I3	1-3
2	HOUR		I2	4-5
3	MIN		I2	6-7
4	YR		I2	8-9
5	LAT (per.)	Deg.	F5.1	10-14
6	WLONG(per.)	Deg.	F5.1	15-19
7	ALT (per.)	Km.	F7.2	20-26
8	LAT (apog.)	Deg.	F9.1	27-35
9	WLONG(apog.)	Deg.	F9.1	36-44
10	ALT (apog.)	Km.	F7.2	45-51
11	REV. No.		I9	52-60
12	L.T. (per)	Hr.	F6.2	61-66
13	L.T.(apog.)	Hr.	F4.1	67-70
14	MODEL	"18"	I2	71-72
15			I4	73-76
16	IDVEH		I4	77-80

grams. Some of these have been resolved, and others that would require further extensive study but were tolerable are described.

Figure 3 shows a printer-plot of the differences in eccentricity between the mean values provided by ADC (A), and the mean values derived by conversion of the SCF position-velocity vector (X). The element sets are for satellite 7499 and cover a period of 60 days. The argument of perigee is drawn and the greatest $e_A - e_X$ values are seen to occur for $w=270^{\circ}$. A zero drag run of ROPP showed that this program inputs and outputs mean elements that include the long period oscillation due to J_3 . The larger e_A value (≈ 0.0075) for perigee near the South pole shows that the ADC elements leave out the long period perturbations whereas ROPP assumes that they are included. The ADC elements are therefore adjusted for eccentricity (see Section 4.1, Equation 1). The mean semi-major axis is obtained from the mean motion using Equation 5 of Section 13 of Section 4.4.1.

Figure 4 shows the same mean eccentricity values on an absolute scale. A ROPP pure prediction run was made starting with a pair of early elements and an optimized $\frac{C_D}{M} A$. The mean eccentricity (R) is seen to drop off too rapidly after 30 days, along with the associated perigee altitude, indicating that the atmospheric density model in ROPP has an insufficient scale height. (also see Figure 6, Section 4). This problem was not tackled.

Figure 5 represents the results of a search for the cause of erratic altitude predictions in ROPP when using different SCF vector sets. The reference eccentricities (X) are the ones obtained by conversion of SCF elements in LOKANGL (Section 4.3). These elements were also converted in ROPP and the differences $e_R - e_X$ are shown. The ADC mean eccentricity differences $e_A - e_X$ are also shown. The abscissa is the argument of latitude ($w+M$). Values for the different element sources were time interpolated before comparison. The ROPP eccentricities do not even monotonically decrease. The conclusion is that ROPP conversion between mean and osculating elements is always poor when these elements are provided near the poles. Data is absent near the South pole, but a repeating pattern seems indicated. The equally likely large positive or negative differences--leading to the erratic altitudes is unexplained. Inspection of ADC eccentricities with the J_3 correction also shows substantial disparity with the SCF derived values; however the fact that ADC elements are invariably provided near an upward equator crossing limits our evaluation of this problem.

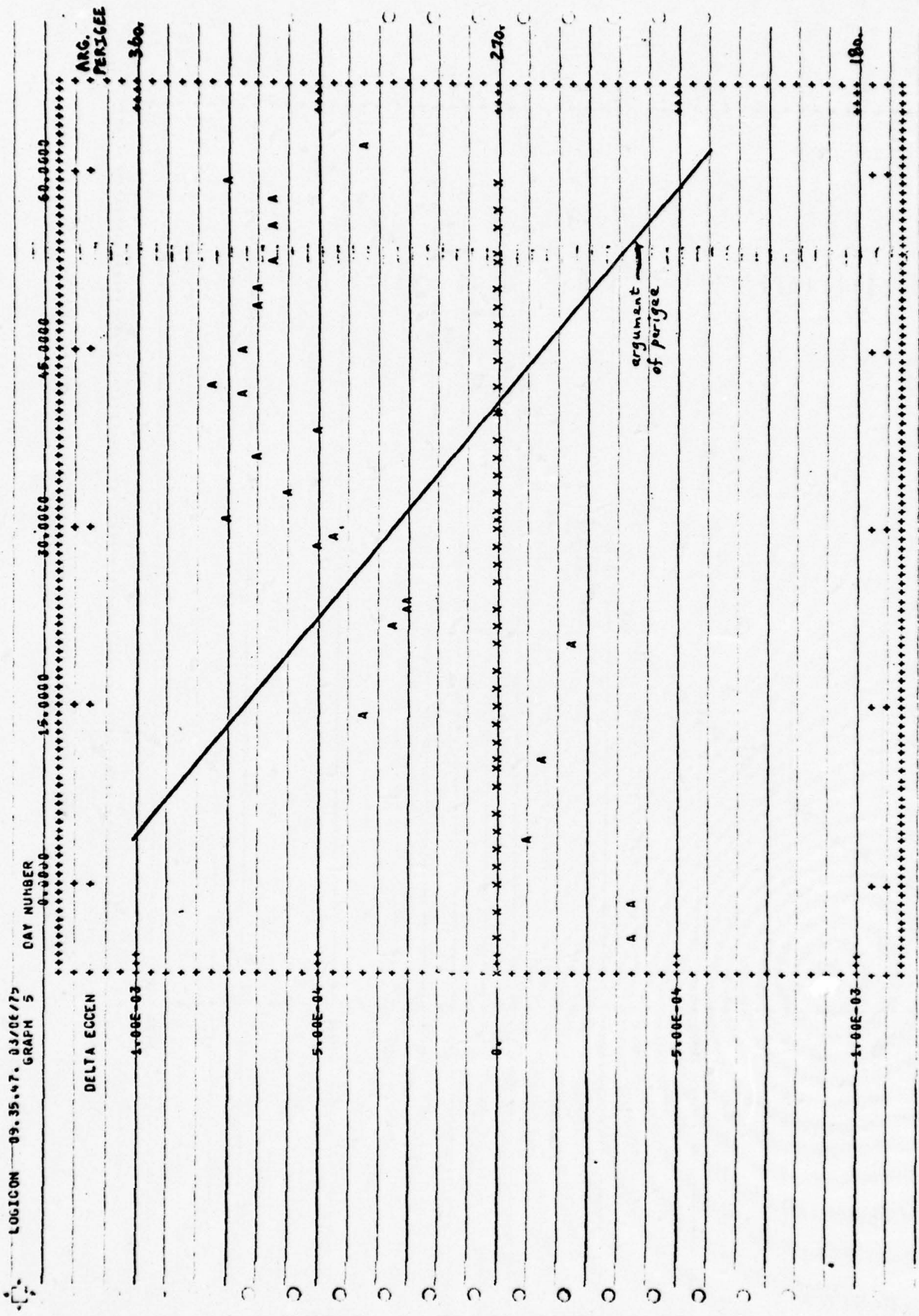


Figure 3. ADC-SCF Eccentricity Comparison Before J_3 Correction to ADC Elements

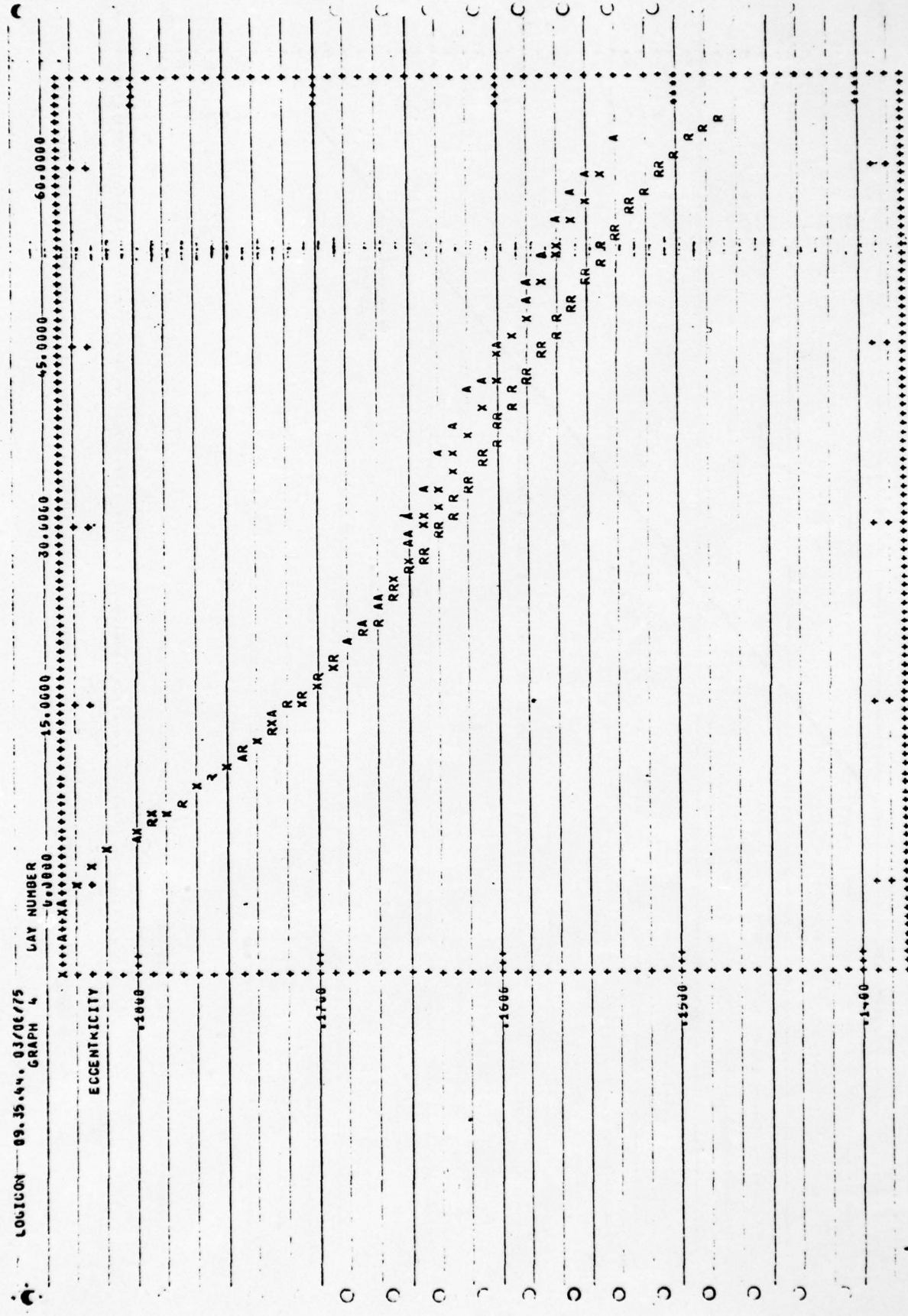


Figure 4. ADC, SCCF and ROPP (predicted) Eccentricities

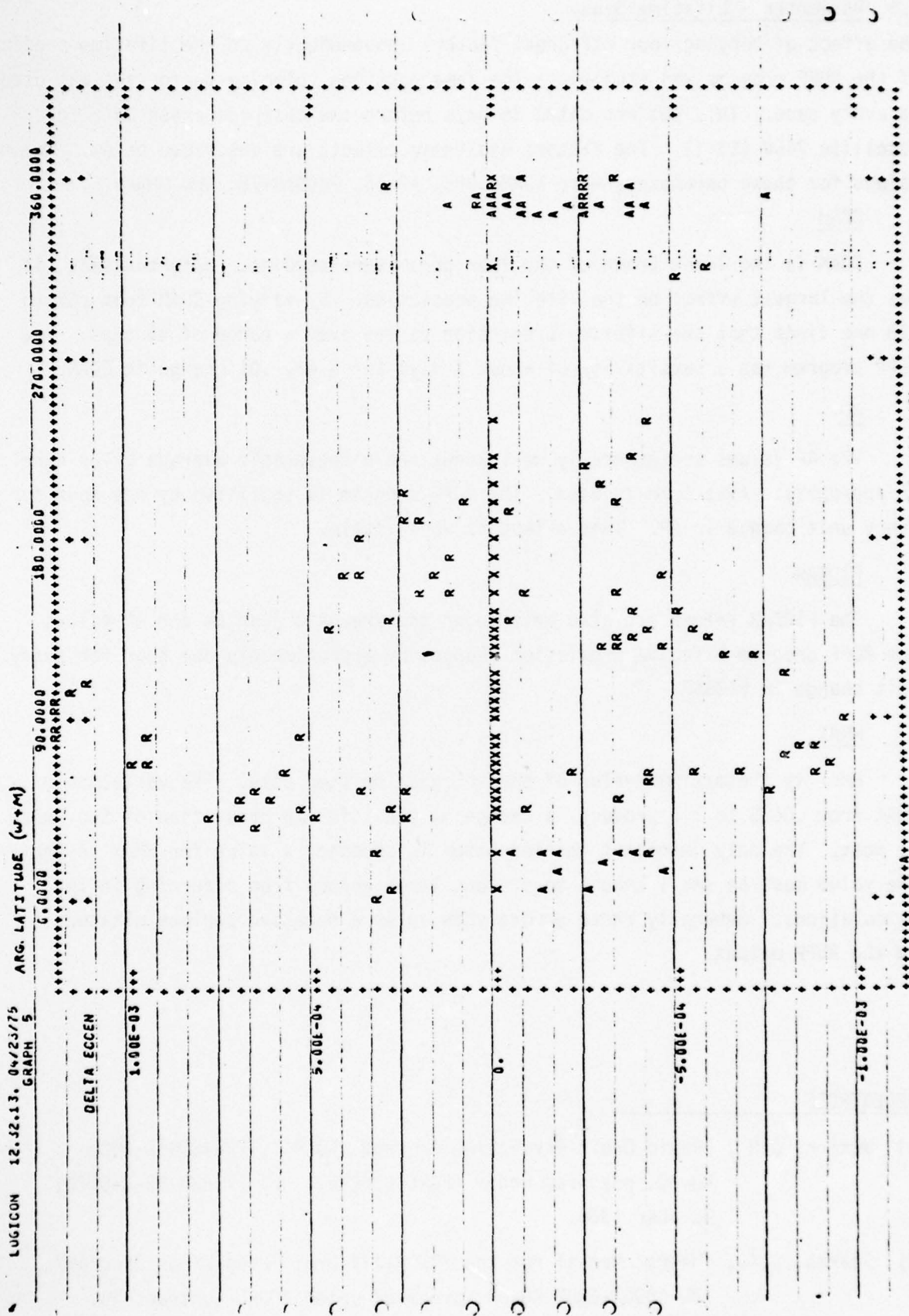


Figure 5. Comparison of ROPP and LOKANGL(X) Derived Eccentricities Against Argument of Latitude
ADC eccentricities are also compared.

3.5 Parameter - Lifetime Study

The effect of varying four different factors independently on the lifetime prediction of the ROPP program was studied. The same position velocity vector set was used in every case. This set was dated 25 days before the observed crash date for satellite 7499 (S3-1). The factors and their effects are described below. Nominal values for these parameters were CDAM=.055, AP=15, FLOBAR=75, and HMAX=.5.

CDAM

CDAM is the least known of the four parameters studies. Unfortunately, it has the largest effect on the lifetime prediction. By varying CDAM from .02 to .08 one finds that the lifetime prediction varies over a range of 45 days. The ROPP program has a sensitivity of about 7 days for every .01 change in CDAM.

AP

The AP values are generally well known and a reasonable average value over an appropriate time span is used. The ROPP program is sensitive by one hour for every unit change in AP. This effect is very little.

FLOBAR

The FLOBAR values are also well known and are used just as the AP values. The ROPP program lifetime prediction changes by approximately one hour for every unit change in FLOBAR.

HMAX

HMAX is the maximum value of the integration step size. The variation of HMAX from .0625 to 1.0 produces a change in the lifetime prediction of two hours at most. The only important consideration in choosing a value for HMAX is that the value must be small enough to prevent large errors from occurring in the calculations. Generally these errors show up as a negative perigee altitude in the ROPP output.

REFERENCES

- 1) Wexler, D.M., "Rapid Orbit Prediction Program (ROPP)", TRW-09967-6001-R0-00, prepared under AFCRL Contract No. F19628-68-C-0170, October 1968.
- 2) Sparks, S.T., "Users' Manual for the TRW Rapid Orbit Prediction Program", TRW-09967-6002-R0-00, prepared under AFCRL Contract No. F19628-68-C-0170, October 1968.

- 3) Minka, K., Fein, J., and Clemenz, B.E., "Orbit Determination and Ephemeris Computation", AFCRL-66-259, May 1966.
- 4) Bramson, A.S., "Program Structure of Atmospheric Density Programs", AFCRL-TR-75-0063, February 1975.

Section 4. Satellite Ephemeris Generation Program - LOKANGL

4.0 Satellite Ephemeris Generation Program - LOKANGL

Initiator: I.M. Hussey

Project No.: 0001

Problem No.: 4506,4801

Program LOKANGL is a specialized orbit determination program that primarily serves the requirements of the AFGL research community. Radar and other observational data may be dispensed with when good quality orbital elements are provided by other agencies that regularly operate full scale orbit determination programs. The program analytically generates satellite ephemerides along with related observational conditions as desired by various researchers. The program has been substantially augmented in response to growing use. LOKANGL was modified to provide reliable ephemerides over long spans of time by interpolating between sequences of elements. Abnormal discontinuities due to improper elements can be recognized by inspection. The program has also been extended to accept and output position-velocity vectors such as are provided by SCF. Support programs for plotting key orbital characteristics over the time spans have been developed and are regularly used. These are described in Section 5.

4.1 Use of Element - Sets

Figures 1 and 2 describe the card format input for elements that are accepted by LOKANGL and ROPP. Information which may be punched but is ignored by LOKANGL is shown double-lined out. The crossed-out columns are blank separators between fields. Figure 1 shows the original ADC format which was received by teletype. The sixth line was not provided. The one digit year is now used in LOKANGL to indicate a year in 1970. The Modified Julian Days on card 2 is the Julian Date plus fraction less 2400000.5 Thus the fraction is the UT in days. The integer part is optional and is shown dashed. In early 1974 ADC switched over to a 2-card teletype message and eliminated the semi-major axis and all derivatives of the elements. Only the first and second derivatives of the mean motion ($N/2$ and $N/6$) remain. This format is shown as Form No. 2 in Figure 2. A technical document⁽⁶⁾ outlined how the missing quantities could be recovered. This brought out a problem in the determination of the semi-major axis which was subsequently resolved (see Section 4.4).

Form No. 3 in Figure 2 is adapted for entering SCF position-velocity vector sets that are also available by teletype. Period Decay in seconds/rev. provides the drag estimate. Conversion of this data to mean Kepler elements for use in LOKANGL is described in Section 4.3.

AFCRL DATA ANALYSIS BRANCH
 ORBITAL DETERMINATION FORM NO. 1
 CRNA ELEMENT DATA SET-SIX

1 2 3 4 5 6 7 8 9 10 11 12 13 14 15 16 17 18 19 20 21 22 23 24 25 26 27 28 29 30 31 32 33 34 35 36 37 38 39 40 41 42 43 44 45 46 47 48 49 50 51 52 53 54 55 56 57 58 59 60 61 62 63 64 65 66 67 68 69 70 71 72 73 74 75 76 77 78 79 80											
Satellite Number	U	V	Element Number	YR	Name	Piece	Plot/ST Card Punch Control	Element Number	Revolution Number	Yr. No.	Inclination (i) - Deg.
1	X	X									
2	X	X									
3	X	X									
4	X	X									
5	X	X									
6	X	X									

Satellite Number	Mean Anomaly (M) - Deg.	Rt. Asc. of Node (Ω) - Deg.	Arg. of Perigeo (ω) - Deg.	Eccentricity (e)	Inclination (i) - Deg.	Element Number
1	X	X	X	X	X	
2	X	X	X	X	X	
3	X	X	X	X	X	
4	X	X	X	X	X	
5	X	X	X	X	X	
6	X	X	X	X	X	

Satellite Number	Mean Motion (n) - Revs/Day	0 - Deg./Day	ω - Deg./Day	ε - Deg./Day	i - Deg./Day	Element Number
1	X	X	X	X	X	
2	X	X	X	X	X	
3	X	X	X	X	X	
4	X	X	X	X	X	
5	X	X	X	X	X	
6	X	X	X	X	X	

Satellite Number	$\dot{n}/6$ - Revs/Day ³	$\ddot{n}/24$ - Revs/Day ⁴	$\ddot{\Omega}/2$ - Deg/Day ²	$\ddot{\omega}/2$ - Deg/Day ²	$\ddot{e}/2$ - Deg ² /Day ²	Element Number
1	X	X	X	X	X	
2	X	X	X	X	X	
3	X	X	X	X	X	
4	X	X	X	X	X	
5	X	X	X	X	X	
6	X	X	X	X	X	

Satellite Number	Semi Major Axis (a) - Earth Radii	0 - E.R./Day	$\dot{a}/2$ - E.R./Day ²	Element Number
1	X	X	X	
2	X	X	X	
3	X	X	X	
4	X	X	X	
5	X	X	X	
6	X	X	X	

Satellite Number	Anamolistic Period (P _a) - Min/Rev	Drag Term (C _D) - Days/Rev ²	Perigee Height Km.	Blm Initial Rev. Number	Blm Length	Bulletin Engine	Nodal Period (C _N) Days/Rev ²	Drag Term (C _D) Days/Rev ²	Element Number
1	X	X	X	X	X	X	X	X	
2	X	X	X	X	X	X	X	X	
3	X	X	X	X	X	X	X	X	
4	X	X	X	X	X	X	X	X	
5	X	X	X	X	X	X	X	X	
6	X	X	X	X	X	X	X	X	

Figure 1. ADC 5-card Element-set Format
 Crossed and double-lined entries are not required.

APOL DATA ANALYSIS BRANCH
ORBITAL DETERMINATION FORM NO. 2
ABC SPADATS ELEMENT DATA SET - TWO

Satellite #	Illumination	Ref.	ISSN	Ecc.	Avg. Perigee	Mean Anomaly	Mean Motion	Rv #
1	U	X						
2	U	X						
3	U	X						
4	U	X						
5	U	X						
6	U	X						
7	U	X						
8	U	X						
9	U	X						
10	U	X						
11	U	X						
12	U	X						
13	U	X						
14	U	X						
15	U	X						
16	U	X						
17	U	X						
18	U	X						
19	U	X						
20	U	X						
21	U	X						
22	U	X						
23	U	X						
24	U	X						
25	U	X						
26	U	X						
27	U	X						
28	U	X						
29	U	X						
30	U	X						
31	U	X						
32	U	X						
33	U	X						
34	U	X						
35	U	X						
36	U	X						
37	U	X						
38	U	X						
39	U	X						
40	U	X						
41	U	X						
42	U	X						
43	U	X						
44	U	X						
45	U	X						
46	U	X						
47	U	X						
48	U	X						
49	U	X						
50	U	X						
51	U	X						
52	U	X						
53	U	X						
54	U	X						
55	U	X						
56	U	X						
57	U	X						
58	U	X						
59	U	X						
60	U	X						
61	U	X						
62	U	X						
63	U	X						
64	U	X						
65	U	X						
66	U	X						
67	U	X						
68	U	X						
69	U	X						
70	U	X						
71	U	X						
72	U	X						
73	U	X						
74	U	X						
75	U	X						
76	U	X						
77	U	X						
78	U	X						
79	U	X						
80	U	X						
81	U	X						
82	U	X						
83	U	X						
84	U	X						
85	U	X						
86	U	X						
87	U	X						
88	U	X						
89	U	X						
90	U	X						
91	U	X						
92	U	X						
93	U	X						
94	U	X						
95	U	X						
96	U	X						
97	U	X						
98	U	X						
99	U	X						
100	U	X						

**AFCL DATA ANALYSIS BRANCH
ORBITAL DETERMINATION FORM NO. 3
CCE POSITION-VELOCITY DATA SET - TWO**

Figure 2. ADC 2-card and SCF Position-velocity Element-set Formats

When any of the three element sets are used in ROPP, derivative information is not required since the program includes a complete force model and analytically generates the trajectory. Program LOKANGL on the other hand operates primarily by polynomial extrapolation and interpolation of mean elements. In the case of SCF data, estimates of the rates of change of the elements must be made initially by semi-analytic means. This is also described in Section 4.3.

When successive sets of elements are available, rates of change can be tested against the new elements and adjustments made. This is discussed in Section 4.2.

The derivatives provided above for use by LOKANGL cannot include the long period perturbation in eccentricity ⁽³⁾ due to the progression of the argument of perigee over the northern and southern hemispheres. The mean mean eccentricity is therefore converted to mean eccentricity by

$$e = \bar{e} + \frac{.001066}{a} \sin w \sin i \quad (1)$$

before computation of osculating elements in LOKANGL. In the case of SCF data the mean eccentricity is initially further reduced to mean mean eccentricity by inverse application of the above equation 6. This finally makes the mean elements from the three sources consistent as far as possible. Some results of a study that was made to resolve these discrepancies are discussed in Section 4.4.

4.2 Use of Successive Sets of Elements

Satellites 7499 (S3-1) and 8468(S3-2) have been of particular interest because of a number of AFGL experiments on board. ADC and SCF element sets based on their full scale orbit determination programs are available by teletype in a timely fashion, allowing generation of ephemerides using a relatively high density of elements. In fact, since the telemetered data is not received for some time, the latest elements extend well beyond the available data. Program LOKANGL was modified to accept time-successive sets of elements in any mix, to adjust first derivatives of a set so as to match the subsequent mean Kepler element set at its epoch, and to generate a trajectory at any time based on the most recent corrected element set. The original single element set mode is automatically effective when no other elements follow since the last element set is not adjusted. Long term predictions beyond available sets are unreliable.

Higher order derivatives are not adjusted because of their smaller effect over a few days, and because of uncertainties over extended periods. For significant-drag orbits the rate of change of mean motion is adjusted to match the mean anomaly; in low drag cases the mean motion is adjusted instead. The original and revised first derivatives can be inspected for abrupt changes, which usually suggests a transcription error in a data set. Plots of satellite apogee-perigee such as Figure 1 in Section 5 can also point up poor element sets when the curves are abnormal.

High quality ephemerides were prepared for the above and other satellites using daily elements covering periods of a month or more. For reasons of consistency, earlier availability, and fewer discrepancies (see Section 4.4), the SCF position-velocity element sets have recently been favored.

4.3 Input of SCF Position-Velocity Vectors

Program LOKANGL has been altered to predict satellite ephemeris and look angles given initial values of position and velocity. Period decay (sec/rev) is also required. Subroutine DELEM has been added to handle the required conversion to SPADATS parameters

4.3.1 Computation of Initial Mean Elements.

Initial mean Keplerian Elements are computed from the input cartesian position and velocities by subroutines taken from program CADNIP⁽¹⁾. Initial position and velocity are assumed to be osculating. Mean motion is calculated in revs/day according to Escobal, ⁽²⁾

$$\dot{M} = \frac{1}{2\pi} \sqrt{\frac{\mu}{a^3}} \left[1 + \frac{1}{2} - \frac{J_2}{a^2(1-e^2)^{1.5}} \frac{(1-1.5\sin^2 i)}{1.5} \right] \times 86400. \quad (2)$$

where μ = Earth gravitation constant = $398603.2 \frac{\text{km}^3}{\text{sec}^2}$

J_2 = Second Harmonic = .0010827549

a = Semimajor axis

i = inclination

e = eccentricity

4.3.2 Derivatives

First and required higher order derivatives are computed from secular changes in the elements over the first 3 successive revolutions due to the second harmonic and drag. The derivatives of a function f are computed as (\dot{M}_i is in revs/day):

$$\begin{aligned} f'_1 &= (f_2 - f_1) \cdot \dot{M}_1 \\ f''_2 &= \left[(f_3 - f_2) \dot{M}_2 - f_1 \right] \cdot (\dot{M}_1 + \dot{M}_2) / 2 \\ f'''_3 &= \left\{ \left[(f_4 - f_3) \dot{M}_3 - (f_3 - f_2) \dot{M}_2 \right] \cdot (\dot{M}_2 + \dot{M}_3) / 2 \right. \\ &\quad \left. - f_2 \right\} \cdot (\dot{M}_1 + \dot{M}_2) / 2 \end{aligned}$$

where f_i is the value of f at the start of the i^{th} revolution.

4.3.2.1 Changes per Revolution

a) Drag

The secular changes per revolution in the elements due to atmospheric drag are computed according to King-Hele³

$$\frac{da}{de} = -a^2 \rho \delta \frac{(1 + e \cos E)^{3/2}}{(1 - e \cos E)^{1/2}} \quad (4)$$

$$\frac{de}{dE} = a \rho \delta \left(\frac{1 + e \cos E}{1 - e \cos E} \right)^{1/2} (1 - e^2) \cos E \quad (5)$$

where E is eccentric anomaly, ρ is the atmospheric density and δ is a drag factor determined from the input period decay. Changes in inclination, ascending node, and perigee argument due to drag are currently neglected since these are proportional to the Earth's rotational velocity. However, coding has been provided to include expressions for these (lines 19-21 in subroutine INTGND) if warranted.

The above expressions are integrated over one rev ($E=0$ to $E=2\pi$) by Simpson's rule⁽⁴⁾ using 1 degree integration steps. The elements are assumed constant during the integration of one revolution at the values assigned to them at the beginning of the revolution. The density is as given by the DENSEL model using subroutine DENSEL of CADNIP⁽¹⁾.

b) Determination of δ

The drag constant δ is determined by requiring the period decay for the first revolution to be the input value, i.e.

$$\delta = \dot{P} / (\dot{dP}/d\delta) \quad (6)$$

$$\frac{\dot{dP}}{d\delta} = \left(\frac{86400}{M_1^2} \right) \left(\frac{\partial \dot{M}}{\partial a} \Delta a + \frac{\partial \dot{M}}{\partial e} \Delta e + \frac{\partial \dot{M}}{\partial i} \Delta i \right)$$

where Δa , Δe , and Δi are the changes in the elements in the first rev computed from $\delta = 1$ and the partials of \dot{M} with respect to the elements are computed directly from Eq. (1).

c) Second Harmonic

The per rev changes due to the second harmonic J_2 are as in Escobal:⁽²⁾

Ascending node

$$\Delta\Omega = C \cos\lambda \quad (7)$$

Argument of Perigee

$$\Delta\omega = -C(2-2.5 \sin^2\lambda) \quad (8)$$

where

$$C = -3\pi T_2 / a^2(1-e^2)^2$$

4.4 Problems with ADC elements.

4.4.1 Mean Semi-Major Axis

A technical document⁽⁶⁾ provided at time of conversion from the 5-card to the 2-card set indicated how the mean (Kozai) semi-major axis \bar{a} could be recovered from the mean motion n and the other data, since it was now unavailable.

$$\bar{a} = a_0 \left[1 + \left(\frac{1}{3} \right) \delta_0 - \left(\frac{1}{3} \right) \delta_0^2 \right] \quad (9)$$

$$\text{where } a_0 = \left(\frac{\mu}{n^2} \right)^{1/3} \quad (10)$$

$$\text{and } \delta_0 = \left(-\frac{3}{2} \right) J_2 \left(\frac{a_e^2}{a_0^2} \right) \left(1 - e^2 \right) \left[1 - \left(\frac{3}{2} \right) \sin^2 i \right] \quad (11)$$

$$\mu = 398603.2, \quad J_2 = .0010827549, \quad a = 6378.165.$$

This equation is in fact consistent with \bar{a} and the mean motion n provided on the 5-card sets. Further, Jan. 1974 2- and 5- card element sets for satellites 1085 and 1620 are effectively identical, indicating no disparity due to the transition.

Investigation of first order secular perturbation theory⁽²⁾ however discloses that the Kozai mean semi-major axis is improper for use as the mean semi-major axis in programs LOKANL and ROPP. The oblateness of the earth is considered to perturb the mean motion but not the semi-major axis a .

$$\text{If unperturbed } n_0 = \sqrt{\frac{\mu}{a^3}}$$

$$\text{Then perturbed } n = n_0 (1 - \delta_0) \quad (12)$$

$$\text{As before, defining } a_0 = \left(\frac{\mu}{n^2} \right)^{1/3}$$

$$\text{We have } a = a_0 \left[1 - \left(\frac{1}{3} \right) \delta_0 - \left(\frac{1}{9} \right) \delta_0^2 \right] \quad (13)$$

Qualitatively, for inclinations near 90° δ_0 is positive and the perturbed mean motion n is lower than n_0 . Hence the fictitious a_0 must be larger than the mean semi-major axis a .

Figure 3 shows before and after printer-plots of the relative mean semi-major axes as obtained from ADC (A) and SCF (X) elements. Use of Equation 13 instead of Equation 9 makes the values from the two sources consistent.

4.4.2 Irregularities

Figure 4 shows inclination obtained from ADC and SCF elements over a 60 day span. Results of ROPP prediction runs using $\frac{C_D A}{M}$ adjusted to give a

matched initial nodal period are also included. A similar plot for eccentricity was shown in Figure 4 of Section 3. It can be seen that the ADC mean elements are much more erratic than the SCF derived values. The systematic sinusoidal difference in eccentricity seen in Figure 3 of Section 3 occurs because the ADC elements provide mean mean eccentricity, and the adjustment for the J_3 zonal is needed according to Equation 1.

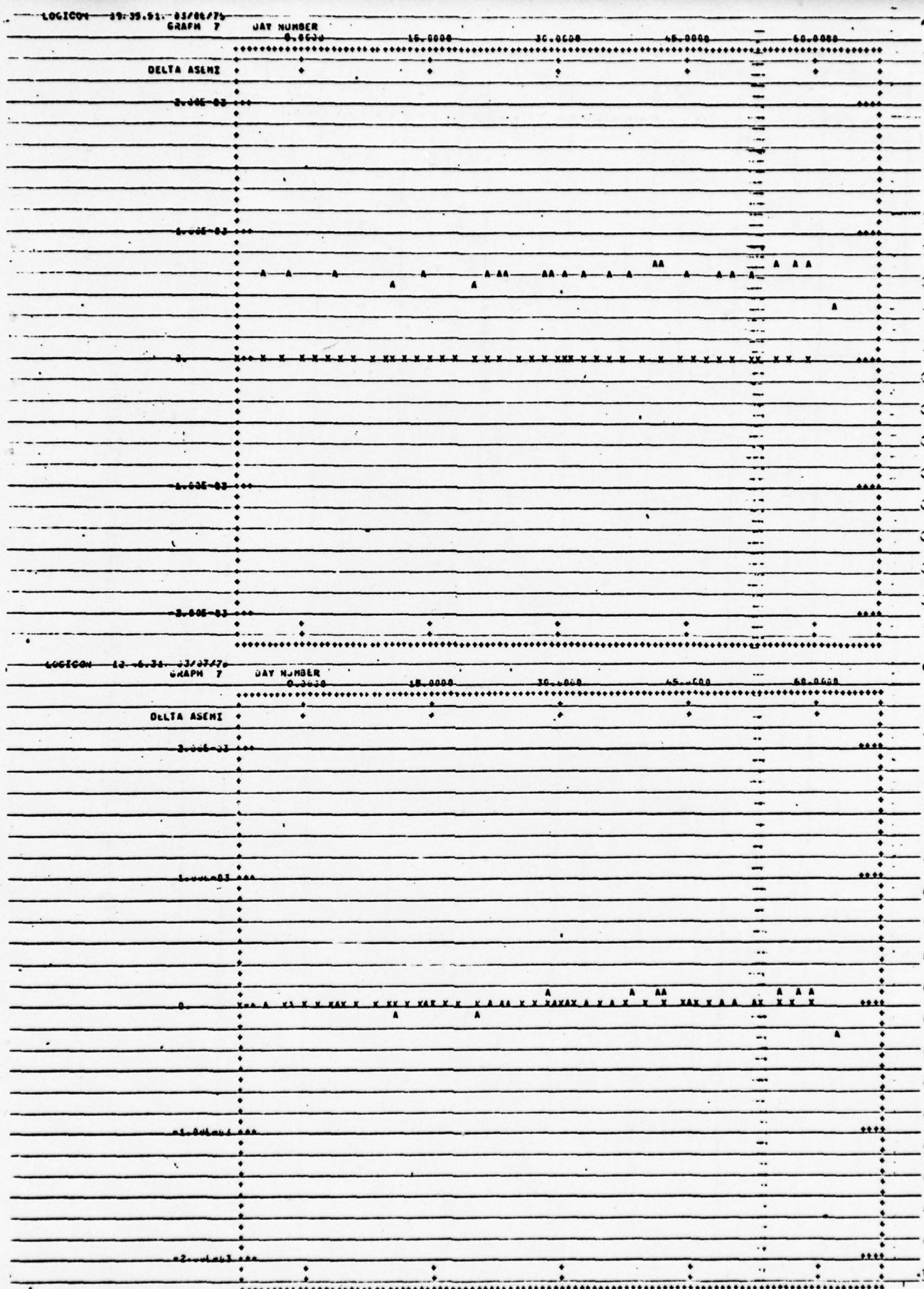


Figure 3. Comparison of ADC and SCF (X) Derived Semi-major Axes Before and After J_2 Correction to ADC Elements

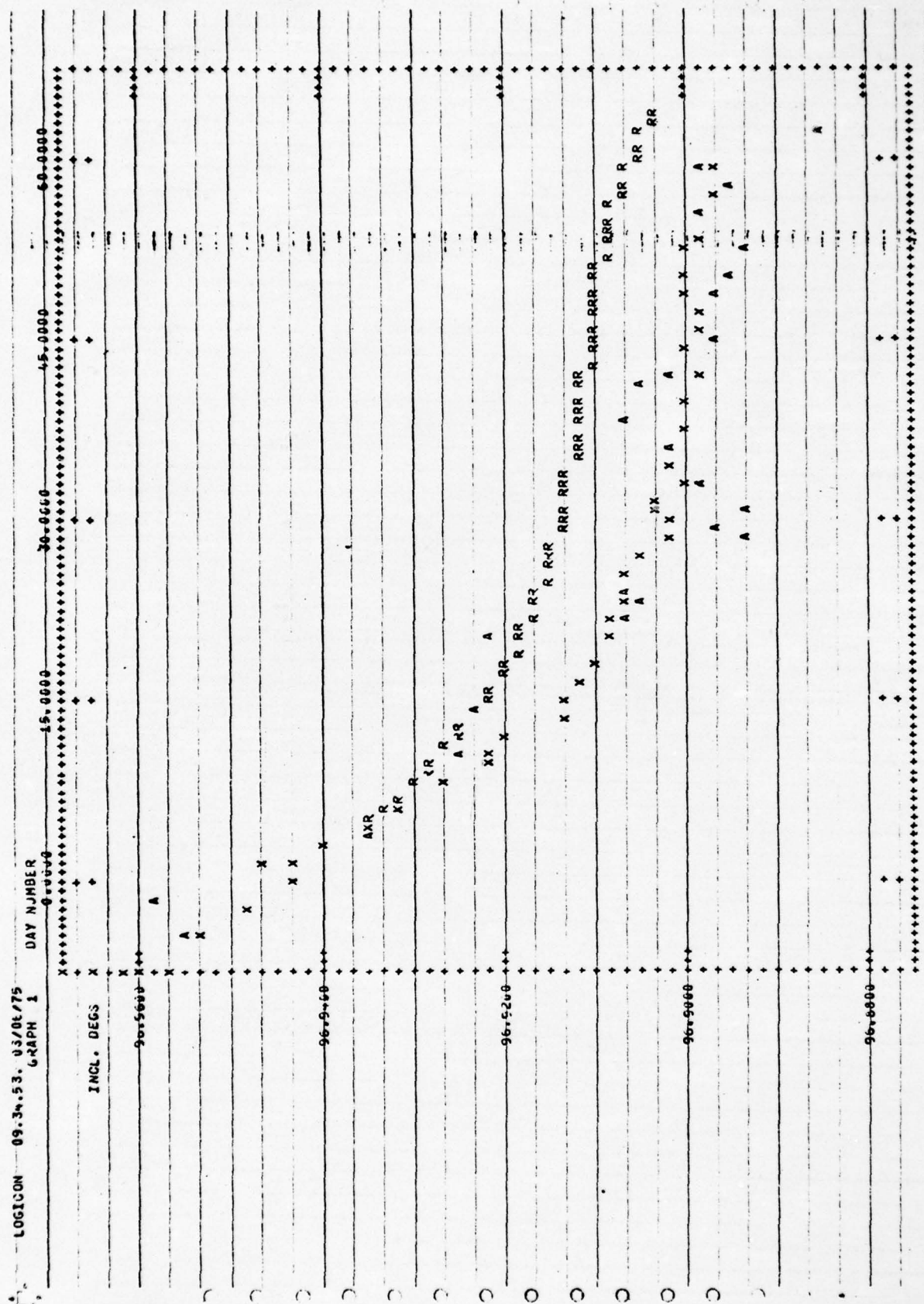


Figure 4. ADC, SCF and ROPP (predicted) Inclinations.

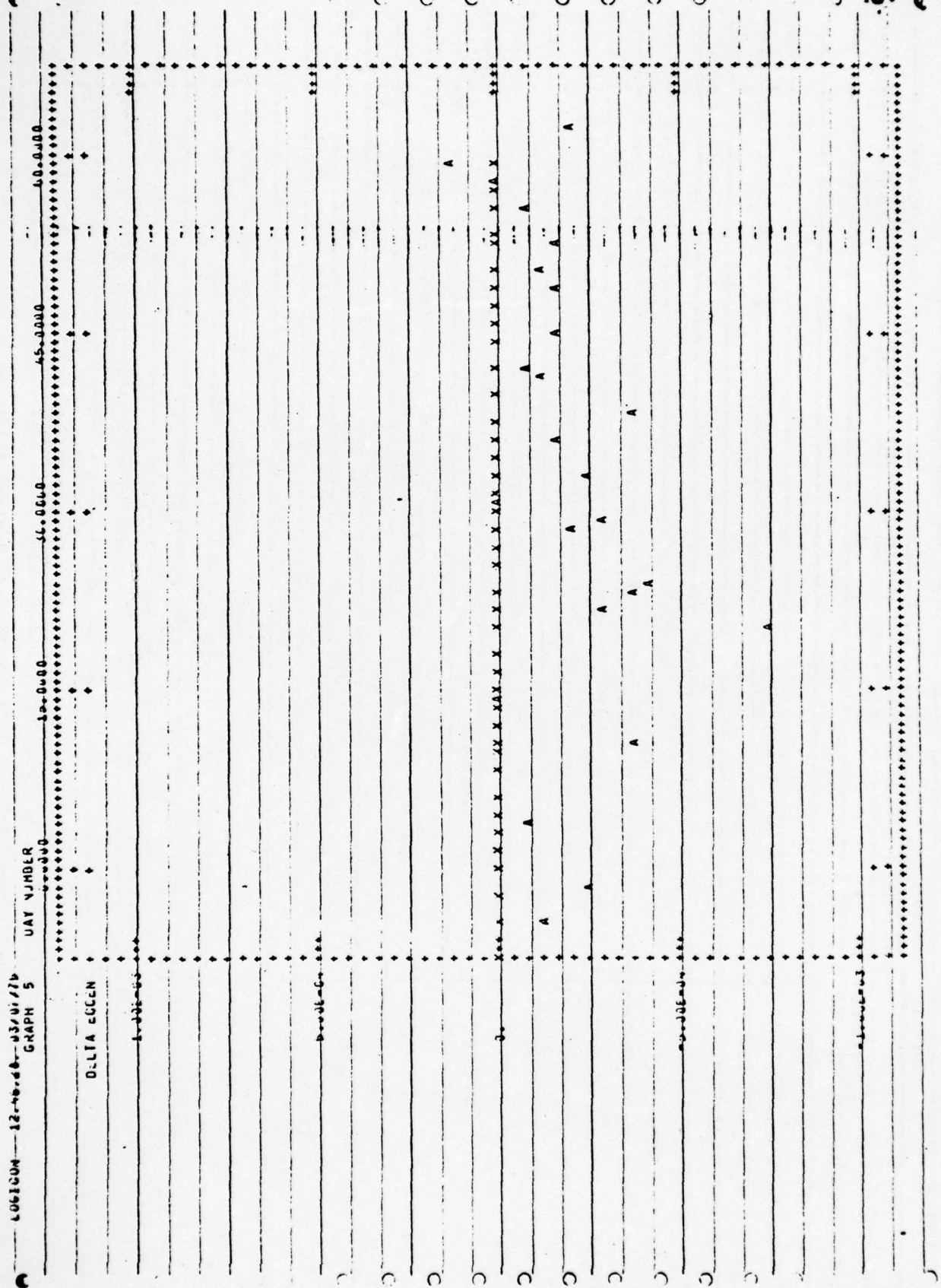


Figure 5. Comparison of ADC and SCF Eccentricities After J_3 Correction to ADC Elements
See Section 3, Figure 3 for pre-correction plot.

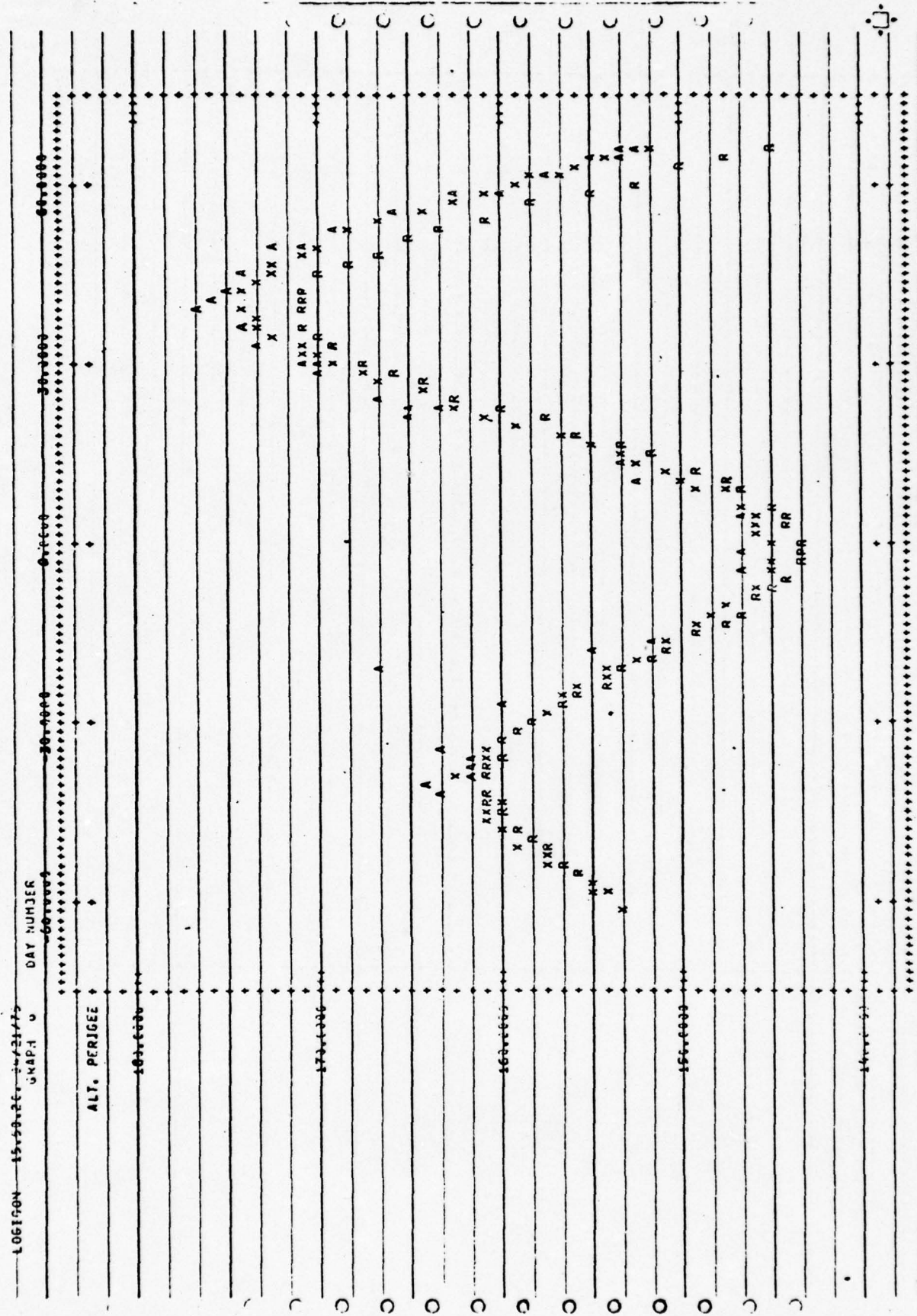


Figure 6. ADC, SCF and ROPP (predicted) Perigee Altitudes

Figure 5 compares the ADC and SCF eccentricities after the above correction has been applied. A small systematic difference is still present, and the irregularities are evident. Figure 6 compares the corresponding perigee altitudes over a 4 month period. The SCF values are seen to be consistently smoother. Incidentally, the lower density scale height is evident in ROPP from the faster altitude decay.

4.5 Other Modifications

Program LOKANGL was compacted by elimination of unused routines, variables, and some double precision code. A number of features were also added and are described below. Card input format has been modified minimally and is shown in Figure 7.

4.5.1 Output of Osculating Position-Velocity.

Routines taken from CADNIP⁽¹⁾ convert mean Keplerian elements to osculating elements which include the short period perturbations. Position and velocity are then directly obtained. Keplerian elements when requested are output as mean values.

4.5.2 Binary Ephemeris File

The binary output file (TAPE3) is identical in format to the file generated by DABOS⁽⁵⁾ except that the maximum number of stations has been limited to 20, and the observational data for all stations (up to 20) are included with the ephemeris record.

4.5.3 Sub-ionospheric Option in LOKANGL.

Subroutine SILL2 was optionally added to program LOKANGL in order to calculate azimuth, elevation, longitude, and geodetic latitude of the location below a given ionospheric height along the direction to the satellite. Subroutine SILL2 was provided by the Ionospheric Physics Laboratory.

4.5.4 Program LOKANGL has undergone a number of changes in order to adjust and present the input/output information in compact form. Also the subroutines WRTAP and WRSTA which generate observational printout were unified into one subroutine WRSTP which allows optional output by time or by station only.

C. ****
 C.
 C. INPUT FORMAT FOR PROGRAM LOKANGL
 C.
 C. ****
 C.
 C. DATA DECK SETUP
 C.
 C. CARD COLS DESCRIPTION
 C. 1 1 CODE OF ORBITAL DETERMINATION FORM
 C. 1=FORM NO. 3 \ SCF 2-CARD POS.-VEL. SET
 C. 2=FORM NO. 2 \ ADC 2-CARD ELEMENT DATA SET
 C. 5=FORM NO. 1 \ ADC 5-CARD DATA SET
 C.
 C. 2+ ONE OR MORE ELEMENT SETS
 C. 0-9 X OR U ON FIRST CARD OF ALL SUBSEQUENT ELEMENT SETS
 C.
 C. 3 1-3 NO. OF STATIONS. IF NO STATIONS USE 0
 C. 6 CODE 1 OR 0 FOR PRINT CONTROL OF STATION DATA
 C. 0=PRINT BY TIME ONLY
 C. 1=PRINT BY STATIONS
 C. 7-10 0=STANDARD
 C. IONOHT=SUPER-IONOSPHERIC ALTITUDE (KM) I3
 C.
 C. 3+ STATION LOCATION CARDS, IF NMS.GT.0
 C. 1-5 I.D. OF STATION (NUMBER)
 C. 8 CODE 2=GEODETI SYSTEM
 C. 9-23 STATION GEODETI LATITUDE. DEGREES
 C. 24-38 STATION LONGITUDE (POSITIVE WEST). DEGREES
 C. 39-53 STATION HEIGHT. METERS
 C. 61-72 NAME OF STATION
 C.
 C. 4 1-15 TIME INCREMENT IN SECONDS. F15.5
 C. 17-69 TIME INTERVAL FOR PRINT OR TAPE 3 WRITE
 C. START COLS\ 17-18;20-21;23-24;26-29;31-34;36-41
 C. FINAL COLS\ 43-44;46-47;49-50;52-55;57-60;62-67
 C. TIME MONTH; DAY; YEAR; HCUR; MIN; SEC
 C. FORMAT I2; I2; I2; F4.1; F4.1; F6.3
 C.
 C. 5 CODE FOR PRINT-OUT: 0=NO PRINT; 1=PRINT FOLLOWING
 C. 2 1=POSITION AND VELOCITY
 C. 4 1=SUPER-SATELLITE DATA
 C. 6 1=MEAN KEPLERIAN ELEMENTS
 C. 8 1=OBSERVATION DATA
 C. 9-10 TAPE 3 CONTROL; STANDARD=0
 C. 11-13 STANDARD=1.0
 C. 6 1-14 "END OF PROBLEM"
 C.
 C. ABOVE MAY BE REPEATED N TIMES
 C. LAST CARD\ "9" IN COL. 1
 C. ****

Figure 7. Card Input Description for Program LOKANGL

References:

- (1) A.S. Bramson, J.W. Slowey -Some Recent Innovations in Atmospheric Density Programs AFCRL - TR - 74 - 0370 (Aug., 1970).
- (2) P.R. Escobal, Methods of Orbit Determination, John Wiley & Sons, Inc., N.Y./London/Sydney (1965).
- (3) D. King-Hele, Theory of Satellite Orbits in an Atmosphere, Butterworths, London (1964).
- (4) F.B. Hildebrand, Introduction to Numerical Analysis, McGraw-Hill Book Co., N.Y. /Toronto/London (1956).
- (5) K. Minka, J. Fein, and B.E. Clemenz, "Orbit Determination and Ephemeris Computation", AFCRL-66-259, May, 1966.
- (6) ADC/DOFS Ltr., Proposed Element Set Format Revision, 19 Oct. 73 (and follow-up 28 Jan., 1975).

Section 5. Satellite Orbit Support Programs

5.0 Satellite Orbit Support Programs

Initiator: I. M. Hussey

Project No.: 0001

Problem No.: 4506, 4801

5.1 Apogee-Perigee Program AP

In order to graphically present and evaluate various satellite orbits, program LOKANGL is often executed simultaneously with program AP which calculates apogee/perigee data using the minute-by-minute binary ephemeris file TAPE3 generated by program LOKANGL. Program AP has undergone changes which allow simultaneous calculations of apogee and perigee data which permits more efficient use of the system of programs LOKANGL, AP & PLOTIT (Section 5.2). Poor quality element sets or transcription errors are readily identifiable as irregularities in the apogee-perigee plots.

Initiator: I. M. Hussey

Project No.: 0001

Problem No.: 4506, 4801

5.2 Program PLOTIT

Program PLOTIT performs three different types of plotting. They are, 1) individual, 2) summary, 3) multiple plots.

Individual plots have one curve only per graph. Summary plots contain several curves of the same variable, each curve representing the use of a different data set. Multiple plots contain several curves of different variables from the same data set. The program was originally developed by C. Foley (Boston College) and has undergone a number of changes. a) Option to read variable data from any tape (not only from punched cards) was added, which allows execution of PLOTIT in conjunction with other programs e.g. LOKANGL, AP. b) Appropriate subroutines of PLOTIT were modified in order to include satellite revolution number on the

***** DATA DECK SETUP *****
 C. GARD 33.5 FORMAT
 C. 1 1-2 "1" NPASS I2
 C. NPASS IS THE NUMBER OF PROBLEMS.
 C. THRUST CARDS ARE ENTERED NEXT AS FOLLOWS...
 C. 1-3 TIME IN DAYS OF THRUST OCCUR
 C. ENCE I3
 C. 5-9 SECONDS OF DAY OF THRUST I5
 C. .
 C. .
 C. .
 C. N LAST THRUST CARD.
 C. N+1 1-2 "-1"(INDICATES END OF THR.) I2
 C. N+2 1-2 VARIABLE FIELD NUMBER I2
 C. 4-9 VARIABLE ABBREVIATION A5
 C. 11-56 AXIS LABEL FOR VARIABLE 4A10
 C. 51-52 VAR. SYM. CODE NUMBER I2
 C. 54-56 FIX OR FLO A3
 C. 53-61 LOWER LIMIT OF VARIABLE F4.0
 C. 63-66 UPPER LIMIT OF VARIABLE F4.0
 C. 68-71 Y AXIS HGT. IN INCHES F4.0
 C. 73-74 NUMBER OF DIGITS TO RT. OF .I2
 C. IF COLS 54-56 ARE FLO, IF
 C. COLS 54-56 ARE FIX, THEN
 C. COLS 73-74 CONTAIN THE NUMBER OF DIGITS.
 C. .
 C. *****
 C. THERE MAY BE AS MANY AS 15 MORE "N+2" CARDS, ONE PER VARIABLE.
 C. NOTE...THE FIRST "N+2" CARD DESIGNATES THE X-AXIS.
 C. .
 C. IF THE FIRST "N+2" CARD HAS AS ITS VARIABLE ABBREVIATION "DAY",
 C. THEN THE DAY NUMBER (X-AXIS) IS CALCULATED ASSUMING THAT THE
 C. FIRST THREE FIELDS OF THE VARIABLE DATA CARD CONTAIN 1.) THE DAY
 C. NUMBER, 2.) THE HOUR, AND 3.) THE MINUTE.
 C. .
 C. N+3 1-90 BLANK(INDICATES END OF "N+2"
 C. CARDS)
 C. NCASES IS THE NUMBER OF DATA DECKS.
 C. MULTIP(I,K) CONTAINS THE VARIABLE FIELD NUMBER. IT ALLOWS UP TO
 C. 6 MULTIPLE PLOTS EACH HAVING AS MANY AS 5 VARIABLES (RT. JUSTIFICATION
 C. FIELD)
 C. IF(IPLT(I),EQ.1), THE FIELD CONTAINING THE "1" (E.G. THE 10TH
 C. I2 FIELD) WILL INSURE THE PLOTTING OF THE VARIABLE WHOSE FIELD
 C. NUMBER IS, IN THIS CASE, 10.
 C. N+4 1-32 NCASES,ISUMRY(I). 16I2
 C. N+5 1-50 MULTIP(I,K) 6(5I2)
 C. N+5 1-32 "15",IPLT(I) 16I2
 C. N+7 1-50 SATELLITE AND MODEL USED 6A10
 C. 63-70 VARIABLE DATA FILE NUMBER (1=CARD INPUT)
 C. *****
 C. NEXT COMES THE VARIABLE DATA
 C. FORMAT(I3,2I2,F2.0,2F5.1,F7.2,2E9.3,F7.2,E9.3,F6.3,
 C. F4.1,I2,F4.0,I4)
 C. THIS DATA MUST BE FOLLOWED BY AN END OF FILE, AND THE
 C. SATELLITE AND MODEL USED CARD, AND VARIABLE DATA
 C. (N+7 ON) IS REPEATED FOR NEXT NCASE
 C. *****
 C. *****

Figure 1. Card Input Description for Program PLOTIT

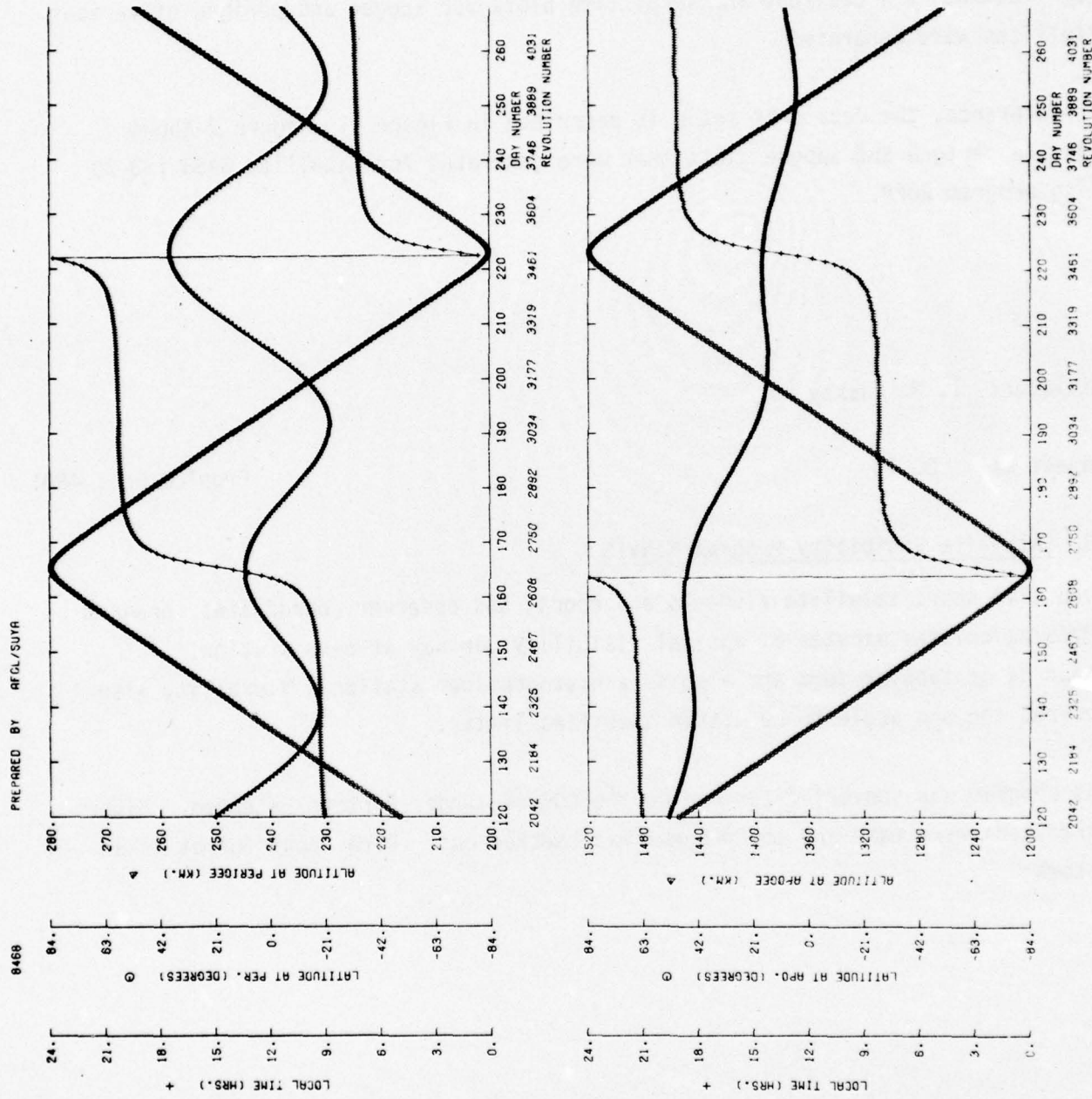


Figure 2. Perigee and Apogee Plots of Latitude, Altitude and Local Time

horizontal scale, as well as to allow correct numbering of the horizontal axis for day number over consecutive years. c) Thrust times can be indicated on the plots (see Figures in Section 7).

Program PLOTIT was regularly used in combination with a number of different programs (ROPP, LOKANG, AP) Latitude and local time plots for apogee and perigee of various satellites were generated.

For reference, the data deck setup is described in Figure 1. Figure 2 shows separate perigee and apogee plots that were generated for satellite 8468 (S3-2) using program ROPP.

Initiator: I. M. Hussey

Project No.: 0001

Problem No.: 4801

5.3 Satellite Visibility Program MINVIS

Given time span, satellite elements and epoch, and observer coordinates, program MINVIS calculates minutes of optical visibility per day at each station. (1)
Output is in tabular form and also as a histogram per station. Visibility also requires the sun angle to be within specified limits.

This program was converted for use on the CDC6600 under Fortran Extended. Minor corrections were made and the program was checked out. Card input format is as follows:

(1) Kellaher, J.G., "Satellite Observability", Analysis and Simulation Branch,
Problem 1444.

Card Input Format for Program MINVIS

CARD	VARIABLE	FORMAT
1	Run No.	I3
	Begin YR, MO, DY, HR, MN, SC	6I2
	End YR, MO, DY, HR, MN, SC	6I2
	Δt (sec)	I5
2	Satellite Ident.	3A6
3	Epoch of Elements YR, MO, DY, HR, MN, SC	6I2
4	Elements Semi-axis (km) Eccentricity Inclination (deg) Mean Anomaly (deg) Arg. of Perigee (deg) Asc. Node (deg)	6E13.8
5+	Station Cards (up to 60) Station Ident. Station Network Station No. Latitude (deg., min., sec.) E.Long. (deg., min., sec.) Altitude (meters) Minimum Sun Elevation (deg) Maximum Sun Elevation (deg)	A6 I1 I3 5X,3F5.0 3F5.0 F7.0 F4.0 10X,F6.0
Last	"END"	A3

Section 6. Satellite Orbit Determination Program-DABOS

6.0 Satellite Orbit Determination Program-DABOS

Initiator: I. M. Hussey

Project No.: 0001

Problem No.: 4801

Program DABOS (1,2) is unique compared to other programs used at AFGL such as CELEST, TRACE and CADNIP which conventionally optimize initial conditions to fit extensive models of the earth's geopotential and atmosphere to radar tracking or Doppler signals. In DABOS a Kalman filtering procedure is used which dynamically weights observations vs. model predictions along the trajectory in both forward and backward integration modes. This procedure is particularly desirable when good quality observations are available and the model is relatively poor. On the other hand a sequence of marginal observations from one station can cause offsets to build up in the trajectory, leading to erratic apogee-perigee altitudes and improper rejection of data elsewhere in the trajectory. A hybrid Kalman filtering and smoothing approach had been initiated but not debugged by the original investigator. Refinements were investigated including dynamic drag adjustment on low perigee satellites, smoothing over extended sets of observations, and integration of the station bias estimation program BIAS⁽³⁾ into DABOS. The latter was converted for operation on the CDC 6600. Other tasks that were completed allow input of SCF observational data in "DECOR" format, and incorporation of advanced geopotential and atmospheric models in DABOS.

Another valuable aspect of DABOS is its output and ephemeris tape compatibility with program LOKANL which itself was originally derived from DABOS. This plus its relatively modest operational requirements (110K with two overlays) permit flexibility in development and research investigations. Parallel development of these programs has promoted retention of these attributes.

6.1 Smoothing

Some difficulty arises in the use of program DABOS⁽¹⁾ over large time spans in which data is lacking and/or high geomagnetic activity occurs. For example, large adjustment in the state vector by the Kalman filter for the first few data points after such time spans occasionally produces noticeable jumps in perigee heights (1-2km). A recent version of DABOS which incorporates an ad-hoc smoothing technique⁽⁴⁾ was therefore tested

and found useful in alleviating these discontinuities. Changes and usage of this program are described here.

6.1.1 Smoothing Program

The smoothing version of DABOS uses the filtered state vectors at 6 data points to refine the vector at the 4th as,

$$\bar{x}_4(t_4) = \sum_{k=1}^6 2^{-|k-4|} x_k(t_4) / \sum_{k=1}^6 2^{-|k-4|} \quad (1)$$

where $x_k(t_4)$ is the state vector at t_4 obtained by integrating from the filtered state vector at t_k to time t_4 . Consecutive state vectors in Eq (1) must be separated by at least 10 minutes in time. The Keplerian elements rather than position-velocity are used in this procedure. The resulting smoothed vector is used for subsequent orbit prediction (in the filtering) but the original filtered vectors (not the smoothed vectors) are saved for subsequent smoothing.

An additional feature of the smoothing version of DABOS is the calculation of the state transition matrix by the "perturb and integrate" method:

$$\frac{\partial x_k}{\partial x_i} = \frac{x_k(x_i + \Delta x_i) - x_k(x_i)}{\Delta x_i}$$

where x_i is a component of the state vector at time t_i , and the state vector $x_k(x_i)$ is obtained by numerical integration from t_i to t_k .

6.1.2 Changes

For addition of atmospheric density subroutine DENS see Section 6.3.

For expanded geopotential models see Section 6.4.

For addition of DECOR input and other changes see Section 6.5.

6.1.2.1 Restricted BCD ephemeris output

A new input parameter NPRT has been added, specifying the ratio of BCD to binary ephemeris output interval when both BCD and binary output are requested. This permits a fine interval for the binary ephemeris when such is necessary for further processing such as for perigee computation, while at the same time avoiding an overly cumbersome BCD printout.

6.1.2.2 Variable number of points in smoothing

Coding has been added to vary the number of data points used in smoothing. In addition, smoothing can be suppressed.

6.1.2.3 Atmospheric Density Update

The smoothing version of DABOS was tested using 2, 4, and 6 smoothing points and found to be reasonably successful in removing perigee height jumps found previously. This however does not establish the accuracy of the resulting orbits. It is evident that the real cause of the orbital discontinuities encountered here are dynamic variations not properly accounted for. The smoothing technique will average over these variations but not reproduce their details. Furthermore, a DABOS - type run which includes atmospheric density updates, along with state vectors could produce a record of time variation of density which could serve as a useful research tool. For these reasons it was decided to introduce a coefficient C which multiplies the model density.

The procedure for updating this parameter is similar to that given on pages 32-4 of Ref. 1 for the determination of type 1 (dynamical) constants. However modification is necessary to account for the fact that the parameter to be determined here is not constant. This is done, in the calculation of the predictive covariance matrix, by adding to the density covariance a term P_c'' which represents the uncertainty in density variation since the previous observation. Thus Eqs. (60) and (62) are modified to read

$$P_{xc} = \theta_x P'_{xc} + \theta_{xc} (P'_c + P''_c), \quad (2)$$
$$P'_c = P'_c + P''_c$$

P''_c is currently treated as input with a value of .05 found to be most satisfactory.

6.2 Observation System Bias Estimation

Experience with satellite tracking has shown that observations usually contain biases or systematic errors in addition to the random noise. In modern tracking systems (particularly electronic systems), two more factors complicate the situation. The ratio of the random noise to the bias errors is usually small, and the functional (often time dependent)

form of the bias errors is almost impossible to predict and formulate. This is not due to any deficiencies in theory but simply to the fact that equipment can malfunction and often does in a manner that cannot be predicted or even recognized from the output. On the other hand, high frequency random noise and sudden large changes in the output parameters can be easily recognized and treated accordingly.

In the orbit prediction program DABOS, this problem was alleviated by estimating the system standard deviations inclusive of the bias errors by successive approximations using the minimum variance method in a multiple filtering process. While this method has certain advantages and might be the only practical method in many cases, it might not give sufficiently accurate estimates of the orbit in case the bias errors are very large and the number of observing stations is small.

It is possible to go one step further and try to estimate the biases simultaneously with the orbital elements. A development based on the minimum variance method and outlined in Ref. 1, pp 34 to 37 is utilized in the present program BIAS⁽³⁾. This program was reviewed and debugged for operation on the CDC 6600.

The program was found to yield satellite positions deviating from those of the original DABOS by up to 50 km, and station location biases of the same magnitude. These results have been attributed to incorrect calculation of the bias-orbit covariance, and this was corrected.

6.3 Atmospheric Density Models

An objective of acquiring and operating program DABOS was to facilitate atmospheric density studies through the calculation of the atmospheric drag on satellites. To further this end, several density models have been added to DABOS as optional alternatives (including the Jacchia 1964). This was done by adding subroutine DENS which had been written for program CADNIP⁽⁵⁾, another orbit determination program. Subroutine DENS contains the option to compute the density according to any of the models listed in the Input Format description at the end of this section. (The missing numbers correspond to other density models handled by CADNIP, but not in this subroutine.) These models contain explicit dependence on many of the following effects:

- (a) Solar activity
- (b) Geomagnetic activity
- (c) Diurnal effect

- (d) Semiannual effect
- (e) Polar bulge
- (f) Seasonal-latitudinal effects.

The density is computed by

$$\log_{10} \rho = \log_{10} f(T_{\infty}, h) + g$$

where h is the satellite height, $\log_{10} f$ is computed from a table supplied as input, and g and T_{∞} (exospheric temperature) are computed analytically as functions of the above-mentioned effects.

Upon an initialization entry, the requested density model table is read and the appropriate section of the solar and geophysical file is read. Upon a regular entry, the input position is converted to right ascension, declination, and height. The appropriate formulas for computing local exospheric temperature are exercised. Two dimensional quadratic interpolation in temperature and height yields the desired density which may be corrected for geomagnetic index, seasonal latitudinal variations, or semi-annual variations.

Program DABOS currently inputs the following values to DENS:

Initialization Inputs

EQTRD -equatorial radius (6378.165)
 PLRRD -polar radius (6356.783)
 TGRMJD -reference time in M.J.D. (40222.0)
 THET7R -sidereal angle of Greenwich at reference time in revolutions (.27907816)
 THETDT -modified rotation rate of Greenwich in revs/day (.27379093E-2)
 MODTYP -desired model number
 TAPE 8=NDENTP -logical number of file containing atmospheric table
 TAPE 9=NAPFTP -logical number of file containing solar and geomagnetic data
 TSTAPF -time in M.J.D. to start reading and accumulating solar and geophysical data = DJULN+33282

Regular Inputs

TIME - time in M.J.D. of desired density = DT0TSP+33282
 PV - position in normalized xyz inertial cartesian coordinates
 DENFAC - multiplicative factor to apply to densities
 Program DENS outputs the following values to subroutine MOTION:

Outputs

TE - exospheric temperature

HEIGHT - height

DENSIT - density in cgs (g/cc)

The significant part of new density facilities for program DABOS is subroutine APFTMP which computes array APFTAB of 19 x 200 values for storing 200 days of solar and geomagnetic activity data and also array FBAR of 308 values of F10.7. This subroutine has undergone changes which allow calculation of the above tables in case of early termination of the solar flux file. In this case unless the "insufficient data" message is printed the insufficient data is replaced in averaging calculations by the last record.

6.4 Earth's Gravitational Field. (GFORCE addition)

The mathematical model of the dynamical system is expressed by the equations of motion with terms representing the various forces acting on the satellite including Earth's gravitational field, atmospheric drag, Sun's and Moon's gravitational fields and solar radiation pressure.

6.4.1 Gravitational Model

The mathematical representation of the Earth's gravitational field is expressed by means of gravitational potential function which can be written as

$$U = \frac{\mu}{r} \left[1 + \sum_{n=1}^{\infty} \sum_{m=0}^n \left(\frac{R_E}{r} \right)^n P_n^m (\sin \theta) (C_{nm} \cos m\lambda + S_{nm} \sin m\lambda) \right]$$

$$C_{no} = -J_n = C_n, S_{no} = 0$$

where $\mu = G M_{\oplus}$

J_n , C_{nm} , and S_{nm} are numerical coefficients, R_E the mean equatorial radius of the Earth, r the distance of the satellite from the center of the Earth, θ the latitude, and P_n^m the associated Legendre polynomial

$$P_n^m (x) = (1-x^2)^{m/2} \frac{d^m P_n(x)}{dx^m}$$

where P_n is the Legendre polynomial. The longitude λ is to be counted positive to the east in this application.

The harmonics represented in the gravitational potential function are called spherical harmonics. If $0 < m < n$ they are called tesseral harmonics as a

special case of the spherical harmonics. If $m = 0$, they are called zonal harmonics, and if $m = n$, they are called sectorial harmonics. The gravitational potential for bodies with spherical symmetry can be expressed by the zonal harmonics only, i.e., the potential is a function of latitude and independent of longitude. For bodies of arbitrary shape, the potential must include the tesseral harmonics, which are dependent on both latitude and longitude.

6.4.2 Addition of GFORCE to DABOS

In order to examine various geopotential models and to extend the capabilities of DABOS subroutine GFORCE which includes calculation of tesseral harmonics was adapted from program CELEST. The SEIII and GEM models were tested against the single original model in DABOS, which included calculation of only the first six zonal harmonics of gravitational potential. For these large g.p. models the execution time increased by well over an order of magnitude.

Geopotential models for use by DABOS should be created on TAPE25. Format is similar to that used for input to CELEST:

	Variable	Format
Card 1	Alphabetic Ident	A10
	No. of Cards following(N)	E20.14
	m_{\max}, l_{\max}	-2E20.14
Cards 2 to N + 1	m, l $c_{\text{term}}, s_{\text{term}}$	5X,2I5 2E20.14

Note: If N is negative, print-out of the geopotential model terms is suppressed.

6.5 Other Changes

Program DABOS was changed in order to allow input of SCF observation data cards in "DECOR" format. Option to read cards in this format was also added to program BIAS and the smoothing version of DABOS.

Program DABOS was also modified to allow input of pre-launch elements in the same format as the Keplerian or the position-velocity elements.

The following pages describe the Input Format in effect following these various changes.

References

- (1) Minka, K., "Orbit Determination by the Minimum Variance Method," AFCRL-65-579, August 1965.
- (2) Minka, K., Fein, F., and Clemenz, B.E., "Orbit Determination and Ephemeris Computation", AFCRL-66-259, May 1966.
- (3) Minka, K., "Observation System Bias Estimation from Satellite Observations", AFCRL-67-0436, August 1967.
- (4) Frona Vicksell, private communication.
- (5) Bramson, A.S., and Slowey, J.W., "Some Recent Innovations in Atmospheric Density Programs", AFCRL-TR-74-0370 (1974)

C	INPUT FORMAT FOR PROGRAM DABOS					
C	VAR					
CD 1	TITLE					
COL 1-66	ANY DESCRIPTIVE TITLE					
C						
CD 2	MISC INFORMATION					
COL 1-5	NOSAT	SATELLITE NO.	I5			
COL 7-8	MODTYP	TYPE OF DENSITY MODEL	I3			
C						
	1=JACCHIA 1964					
C	2=1966 SUPPLEMENTS					
C	3=JACCHIA 1971					
C	4=1968 CHAMPION					
C	5=JACCHIA-WALKER-BRUCE					
C	6=JACCHIA-WALKER-BRUCE (KF=1)					
C						
	7=LOCKHEED/NASA					
C	8=CHANDRA-KRISHNAMURTHY					
C	12=JACCHIA 1970					
C	13=JACCHIA 1973					
COL 11	NOB	1=REJECT OBS. WITH ELEVATION NOT WITHIN LIMITS SET ON CARD 10	I3			
C	0=DO NOT REJECT ANY OBSERVATION CARD					
COL 14	NAT	1=CORRECT ELEVATION, RANGE, RANGE RATE FOR REFRACTION				
C	0=NO CORRECTION					
COL 17	MERASE	1=INPUT CARDS 11&12-ZONAL HARMONICS & EARTH CONSTANTS				
C	0=NO INPUT					
COL 20	KO3SPR	1=PRINT FILTERING OUTPUT	I3			
C	0=NO PRINT					
COL 21-23	KCOUNT	NO. OF OBS. TO BE FILTERED MORE THAN ONE	I3			
COL 26	ISM004	1=APPLY SMOOTHING	I			
C	0=NO SMOOTHING					
COL 28-29	NSTPRT	NO. OF STATIONS IN EPHEMERIS PRINTOUT	I3			
COL 30-32	PASS	1.0=SINGLE CORRECTION OF RANGE FOR REFRAC.	E15.8			
C	2.0=DOUBLE CORRECTION					
COL 60-65	IREVL	REVOLUTION NO. AT TIME OF INPUT ORBITAL ELEMENTS				
COL 66-74	TIMTO	SYSTEM TIMING ERROR (SEC.)	F9.3			
COL 76	IDR	ELEMENT TYPE INPUT				
C	0=ELEMENTS INPUT					
C	1=POSITION & VELOCITY INPUT					
C	-1=PRE LAUNCH INPUT					
C						
CD 3+	STATION DATA CARDS (NMS CARDS)					
COL 2-5	NUMSTA	STATION NUMBER	I5			
COL 10	NSG	1=EL. & AZ. IN GEOCENTRIC SYSTEM	I1			
C	2=EL. & AZ. IN GEODETIC SYSTEM					
COL 16-31	PHILAT	STATION GEODETIC LATITUDE (DEGREES)	E15.8			
COL 31-45	S.ON	STATION WEST LONGITUDE (DEGREES)	E15.8			
COL 46-60	A.T	STATION ALTITUDE (M.)	E15.8			
C						
CD 3++	END OF STATION DATA					
COL 73-78	ENDSTA		A6			
C						
CD 4	SATELLITE INFORMATION					
COLUMNS	1-15	16-31	31-45			

Figure 1. Card Input Description for Program DABOS
1 of 4

C.VAR	OMSAT CONTENT	SSAT MASS (KG.)	AREA (SQ.M.)	CDRAG DRAG COEFFICIENT	3E15.3
C					
CD 5	TIME OF INPUT ELEMENTS				
COLUMNS	2-3	5-6	8-9	11-14	16-19
CONTENT	YEAR	MONTH	DAY	HOUR	MINUTE
C.FORMAT				F3.1	F3.1
C					F5.3
CD 6	ORBITAL ELEMENTS				
C	E13.7	CLASSICAL	PJS.=VEL.	PRE LAUNCH	
C	I0R=0	(COL. 76, CD. 2)	IJR=1	I0R=-1	
COL	1-13	AXSEMT	XPOS(KM)	GEOD. LATITUDE (RAD)	
COL	14-26	ECCEN	YPOS (K4)	RADIUS (FT)	
COL	27-39	DINCL	ZPOS (K4)	TOTAL VEL. (FT/SEC)	
COL	40-52	WASC	XVEL (K4/SEC)	LONGITUDE (RAD)	
COL	53-65	WPERI	YVEL (K4/SEC)	AZIMUTH (RAD)	
COL	66-78	XMEAN	ZVEL (KM/SEC)	FL. PATH ANGLE (RAD)	
C					
CD 7	INITIAL ESTIMATE OF POSITION & VELOCITY ERRORS				
COLUMNS	1-13	14-26	27-39	40-52	53-65
C.VAR	P4AT(1,1).....6E13.7.....PMAT(6,6)
C					
CD 8	MEASUREMENT ERRORS (STANDARD DEVIATIONS)				
COLUMNS	1-3	9-16	17-24	25-32	33-40
C.VAR	QP(1)	QP(2)	Q(1).....9=8.4.....Q(7)
CONTENT	DEF1 RT.ASC ELEV		AZIM	RANGE	R.RATE ELRATE AZRATE RANGEAC
C					
CD 9	NO. OF SIGMAS TOLERATED				
COLUMNS	1-3	9-16	17-24	25-32	33-40
CONTENT	DEF1 RT.ASC ELEV		AZIM	RANGE	R.RATE ELRATE AZRATE RANGEAC
C.VAR	CT(1).....9F8.4.....CT(3)
C					
CD 10	ELEVATION ANGLE ALLOWED				
C	USE IF COLUMN 11 ON CARD 2 EQUAL 1				
COLUMNS	1-15		16-30		
CONTENT	MIV. ELEVATION		MAX. ELEVATION		
C.VAR	ELEMIN		ELEMAX		
C					
CD 11	COEFFICIENTS OF ZONAL HARMONICS				
C	USE IF COLUMN 17 ON CARD 2 EQUAL 1				
COLUMNS	1-15	16-30	31-45	46-60	61-75
C.VAR	J(2)	J(3)	J(4)	J(5)	J(6)
C					5E15.3
CD 12	EARTH DATA				
C	USE IF COLUMN 17 ON CARD 2 EQUAL 1				
COLUMNS	1-15		16-30		31-45
C.VAR	REARTH		F		OMU
CONTENT	EARTH RADIUS (KM)		EARTH FLATTENING		3E15.3
C					GRAVIT. NUMBER
CD 13	EPHEMERIS PRINT INFORMATION				
COL	1-15	OPRINT	PRINT INTERVAL (SEC)		E15.8
C	INITIAL AND FINAL PRINT TIMES				
COLUMNS	17-18	29-21	23-24	26-29	31-34
C.VAR	JMPRT	JDYPRT	JYRPRT	HPRPT	XMPRT
CONTENT	MONTH	DAY	YEAR	HOUR	MINUTE
COLUMNS	43-44	46-47	49-50	52-55	57-60
C.VAR	JMPRT	JDYPRT	JYRPRT	HPRPT	XMPRT
					SECPRT (2)

Figure 1. Card Input Description for Program DABOS
2 of 4

CONTENT	MONTH	DAY	YEAR	HOUR	MINUTE	SECOND	-FINISH
COL 69-71 NOSPRI	NO. OF SPECIAL PRINT TIMES.						0
COL 73 JTYPRT	TYPE OF EPHEMERIS PRINTOUT						
C 0=NO EPHEMERIS							
C 1=PRINT POSITION, VELOCITY							
C 2=PRINT POSITION, VELOCITY, ELEMENTS							
C 3=PRINT POSITION, VELOCITY, ELEMENTS, STATION OBS. DATA							
C 4=PRINT POSITION, VELOCITY, STATION OBSERVATION DATA							
C 5=PRINT STATION OBSERVATION DATA							
COL 75-76 KEYTAP	TYPE OF EPHEMERIS TAPE						
C -1=BCD TAPE ONLY							
C 0=BINARY AND BCD TAPE							
C 1=BINARY TAPE ONLY							
CD 14	SPECIAL PRINT TIMES						
C INPUT IF NOSPRI (COL. 70 CD. 13) NON ZERO							
COL 2-3	5-6	8-9	11-14	16-19	21-25		
C.VAR JSP10	JSPDA	JSPYR	SPHR	SPMI	SPSEC		
CONTENT MONTH	DAY	YEAR	HOUR	MINUTE	SECOND		
C							
CD 15+	OBSERVATION CARDS, SPADATS FORMAT						
COL 2-6 ERASE	SATELLITE NUMBER						I5
COL 7-9 MJBS	STATION NUMBER						I3
COL 10-11 MJBS	YEAR LAST 2 DIGITS OF 19XX						I2
COL 12-14 DAYS	DAY OF YEAR DIGITS OF 19XX						F3.0
COL 15-16 ZDAT	HOUR OF ZULU TIMES OF 19XX						F2.0
COL 17-18 ZDAT	MINUTE OF ZULU TIME						F2.0
COL 19-23 ZDAT	SECOND OF ZULU TIME						F5.3
COL 24-29 DBSM	ELEVATION OR DECLINATION (OVERPUNCH OK)						
COL 31-32 ERASE	AZIMUTH OR RT. ASC.						F2.0
COL 33-34 ERASE	AZIMUTH OR RT. ASC.						F2.0
COL 35-37 ERASE	AZIMUTH OR RT. ASC.						F3.1
COL 39-45 DBSM	RANGE						F7.5
COL 46 IEX	EXPONENT (RANGE=RANGE*10.**IEX)						I1
COL 49-54 DBSM	RANGE RATE (OVERPUNCH OK)						F7.5
COL 56-60 DBSM	ELEVATION RATE (OVERPUNCH OK)						F5.4
COL 62-66 DBSM	RANGE ACCELERATION (OVERPUNCH OK)						F5.4
COL 68-72 DBSM	RANGE ACCELERATION (OVERPUNCH OK)						F5.5
COL 75	TYPES OF OBSERVATIONS						
C 1=ELEVATION AND AZIMUT							NTP=2
C 2=ELEVATION, AZIMUT AND RANGE							NTP=3
C 3=ELEVATION, AZIMUT, RANGE, RANGE RATE							NTP=4
C 4=LEVATION, AZIMUT, RANGE, RANGE RATE, FLEV.							
C RATE, AZIMUTH RATE, RANGE ACCELERATION							NTP=7
C 5=DECLINATION AND RIGHT ASCENSION							NTP=1
COL 76	YEAR OF EQUINOX						
C							
CD 15+	OBSERVATION CARDS, DECDR FOMAT						
COL 1-5 NUVEH	VEHICLE NUMBER						A5
COL 7-8 ANTEN	ANTENNA (STATION TYPE)						
COL 10-13 NJSTA	STATION NUMBER						I4
COL 15 NJVR	UNITS OF YEAR						I1
COL 17-19 NJMO	MONTH OF YEAR						I2
COL 20-21 NUDAY	DAY						I2
COL 23-24 NJHO	HOUR						I2
COL 26-27 NJMIN	MINUTES						I2
COL 29-33 SECON	SECONDS						F5.3
COL 35-40 E-EV	ELEVATION (DEGREES)						F6.3

Figure 1. Card Input Description for Program DABOS
3 of 4

COL	42-47	AZIM	AZIMUTH (DEGREES)	F6.3
COL	48-57	RANGE	RANGE (KM.)	F9.3
COL	59-67	RGRAT	RANGE RATE (KM/SEC)	F9.7
COL	68-73	NJNEN	NETWORK NUMBER	I2
COL	71	N)DATA	DATA TYPE IDENTIFIER	I1
C	1=ELEVATION AND AZIMUT			
C	2=ELEVATION, AZIMUT AND RANGE			
C	3=ELEVATION, AZIMUT, RANGE, RANGE RATE			
C	4=ELEVATION, AZIMUTH, RANGE RATE			
COL	80	NTIP	INTEGER "9" INDICATING DEC02 FORMAT	
C				
CD 15++	END OF OBSERVATIONS CARD			
COL	73-78	ENDDAT		
C				
C				
C.....TAPE 1 IS TEMPORARY STORAGE OF OUTPUT (1,0), AND OF TENTATIVE				
C.....EPHEMERIS (2,0).				
C.....TAPE 2 IS EPHEMERIS FOR PRINTING (CAN BE PHYSICAL TAPE)				
C.....TAPE 3 IS BLOCKED BINARY EPHEMERIS (CAN BE PHYSICAL TAPE)				
C.....TAPE 4 HOLDS THE OBSERVATIONS				
C.....TAPE 7 IS FOR THE SEASONAL DENSITY TABLES.				

Figure 1. Card Input Description for Program DABOS
4 of 4

Section 7. Atmospheric Density Studies

7.0 Atmospheric Density Studies

Initiator: K. Champion

Project No.: 6690

Problem No.: 4547

Program CELEST is a satellite trajectory data processing program developed by Naval Surface Weapons Center (NSWC) for navigational and geodetic satellites. The program accurately determines the trajectory of a satellite from Doppler beacon data. CELEST has been obtained by AFGL and modified for use in atmospheric density determination ⁽¹⁾. Modifications include adaptations to the operating system (SCOPE 3. 4) used at AFGL, addition of the Jacchia 1964 ⁽²⁾ and other density models, and the determination of perigee (position where geocentric distance minimizes) and related density calculations.

7.1 Results

CELEST was used to analyze data from satellites DB-7, DB-8, and DB-9 to determine atmospheric density by least squares adjustment of a scale factor (or drag coefficient) multiplying the model density. For comparison a parallel study was performed with program CADNIP ⁽³⁾ for the same satellites and time periods. The same density model (Jacchia 1964) was used in both studies, but CADNIP employed a smaller geopotential model and ADC skin-track observations.

7.1.1 Perigee Latitudes and Heights

Consistent disagreement was found in perigee latitudes and heights (Figures 1-4) for satellites DB-7 and DB-8. This was ultimately traced to the CADNIP definition of perigee as the location of zero mean mean anomaly. The definition employed in CELEST, given previously, is equivalent to zero osculating mean anomaly. The difference between osculating and mean mean anomaly is

$$\Delta M = C_2 X / 8 ea^2 (1 - e^2)^{\frac{1}{2}}$$

$$\text{where } X = 2 (3 \cos^2 i - 1)(1 + X') (1 - e^2)^{\frac{1}{2}} \sin E / (1 - e \cos E)$$

$$+ 3 \sin^2 i [(1 - X') \sin (V + 2W) + (X' + 1/3) \sin (3V + 2W)]$$

$$\text{with } X' = \frac{1}{1 - e \cos E} \left(\frac{1 - e^2}{1 - e \cos E} + 1 \right)$$

E = mean eccentric anomaly

V = mean true anomaly

W = mean argument of perigee

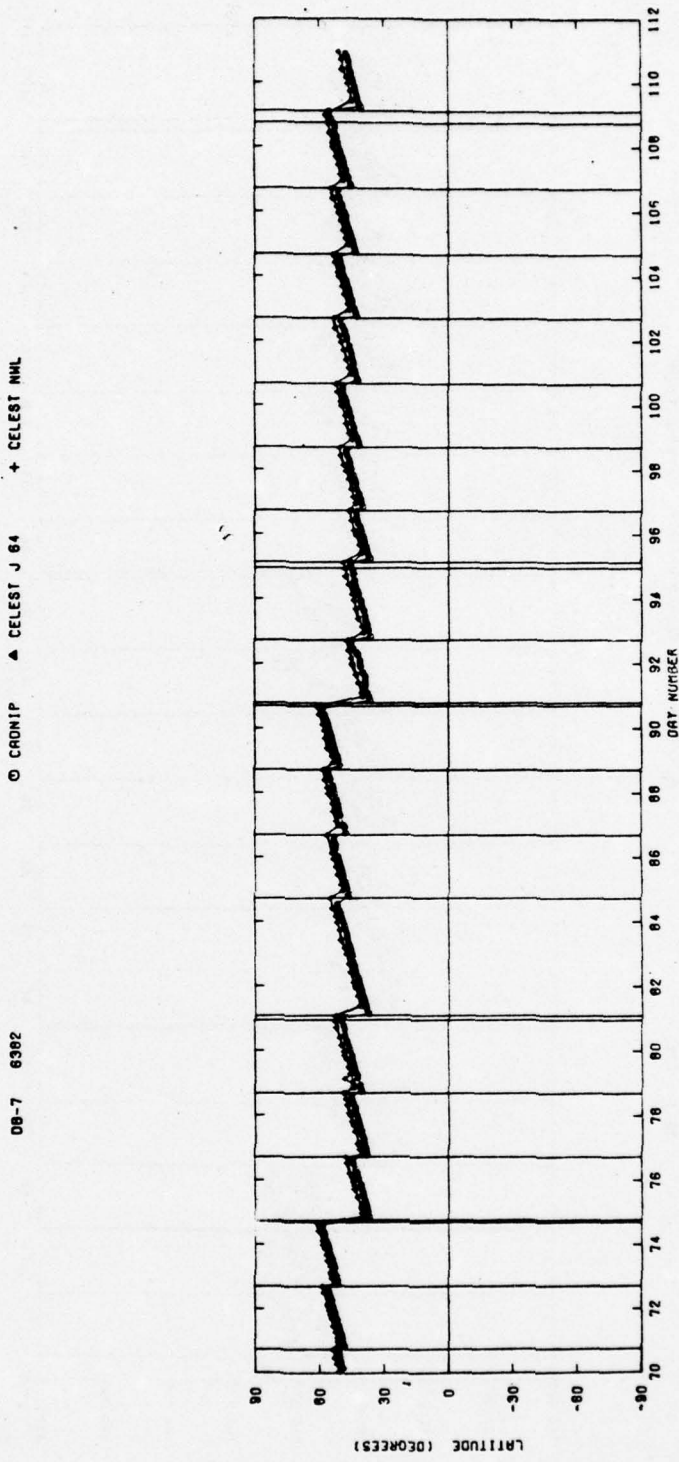


Figure 1. Perigee Latitudes for Satellite DB-7. Vertical lines show thrust times

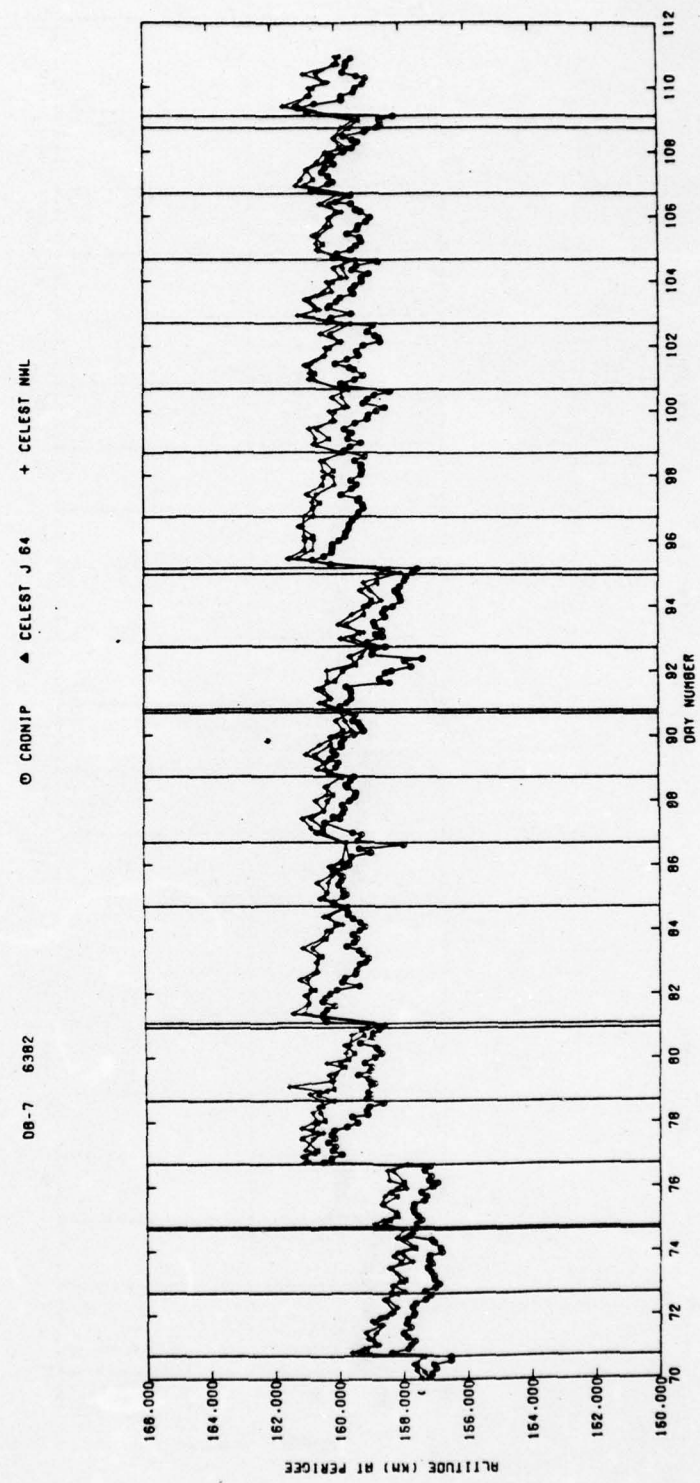


Figure 2. Perigee Heights for Satellite DB-7

© CROWN © CELESTI

06-8 6727

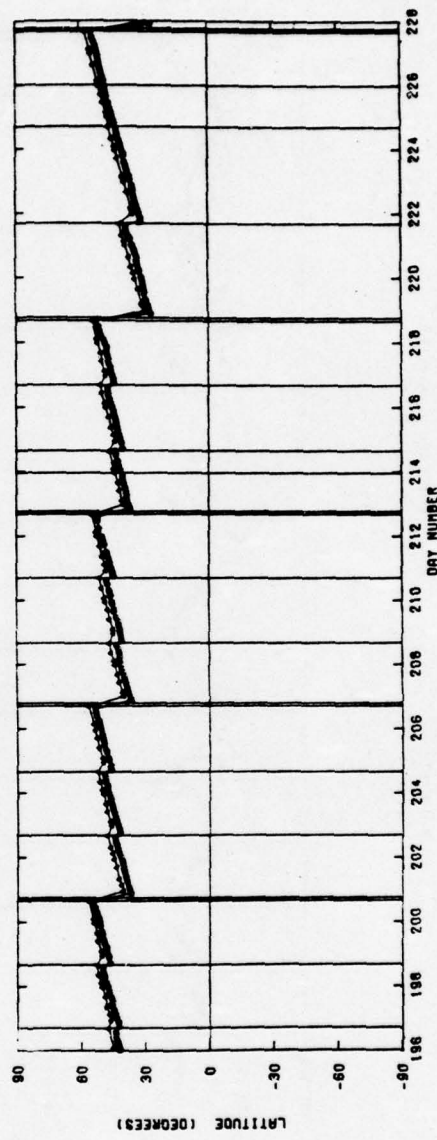


Figure 3. Perigee Latitudes for Satellite DB-8

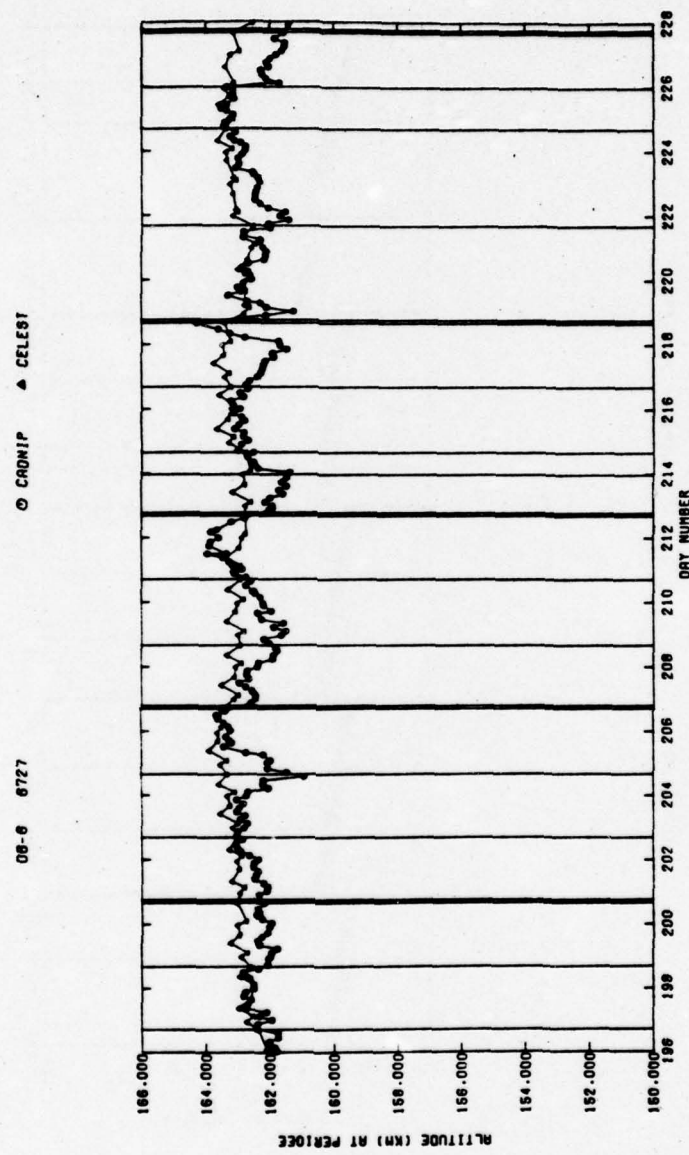


Figure 4. Perigee Heights for Satellite DB-8

i = mean inclination

a = mean semi-major axis (Earth radii)

e = mean eccentricity

C_2 = second harmonic coefficient

For zero mean mean anomaly, values of the other elements ($W = 135^\circ$, $i = 96^\circ$, $a = 6590$ km, $e = .009$) typical for these DB satellites, and $C_2 = -1082.645 \times 10^{-6}$, there results $\Delta M = 3.15^\circ$, which is clearly consistent with the results shown.

CADNIP was therefore modified to define perigee for vanishing osculating mean anomaly. The improved agreement with CELEST (Figures 5-6) for satellite DB-9 verified the above conclusion.

7.1.2 Atmospheric Density

As shown in Figure 7, densities obtained from the two programs were generally in good agreement. The largest differences occur near times of thrusts, the parameters of which can be optimized with least squares adjustment by CELEST but not by CADNIP. Correlation of density model ratio increases with large geomagnetic activity increases (Figure 8) are seen for both sets of results, indicating a deficiency in the density model.

References

- 1) James N. Bass, Krishin H. Bhavnani, and Isabel M. Hussey, Atmospheric Density Determination from Analysis of Doppler Beacon Satellite Data, AFCRL-TR-75-0176, 1975.
- 2) L. G. Jacchia, Static Diffusion Models of the Upper Atmosphere with Empirical Temperature Profiles, Smithsonian Astrophysical Observatory Special Report No. 170, 1964.
- 3) Arnold S. Bramson and Jack W. Slowey, Some Recent Innovations in Atmospheric Density Programs, AFCRL-TR-74-0370, 1974.

Figure 5. Perigee Latitudes for Satellite DB-9

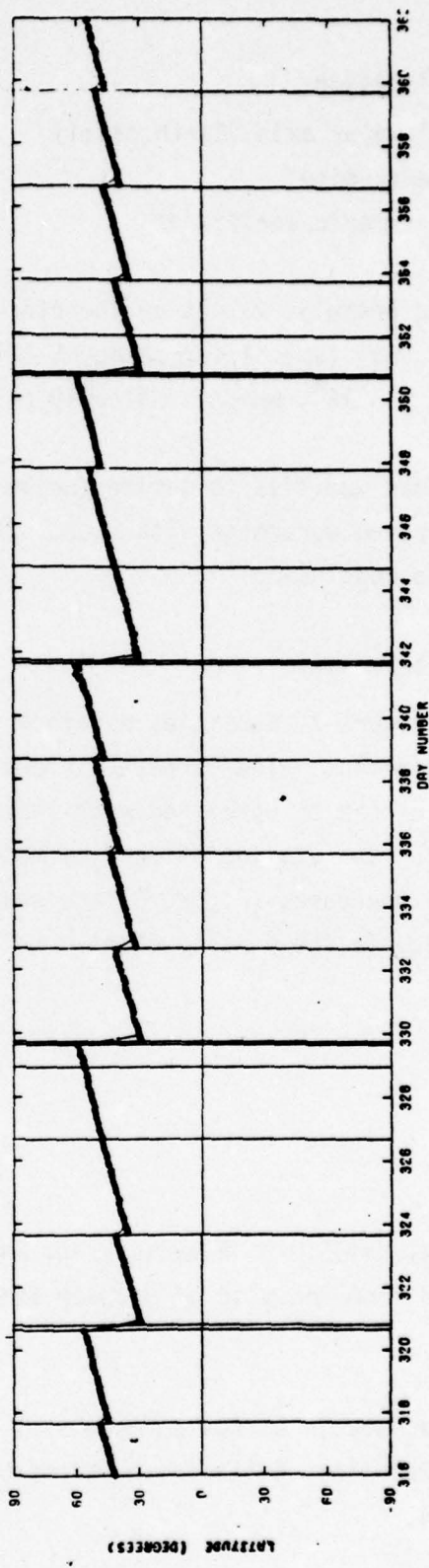
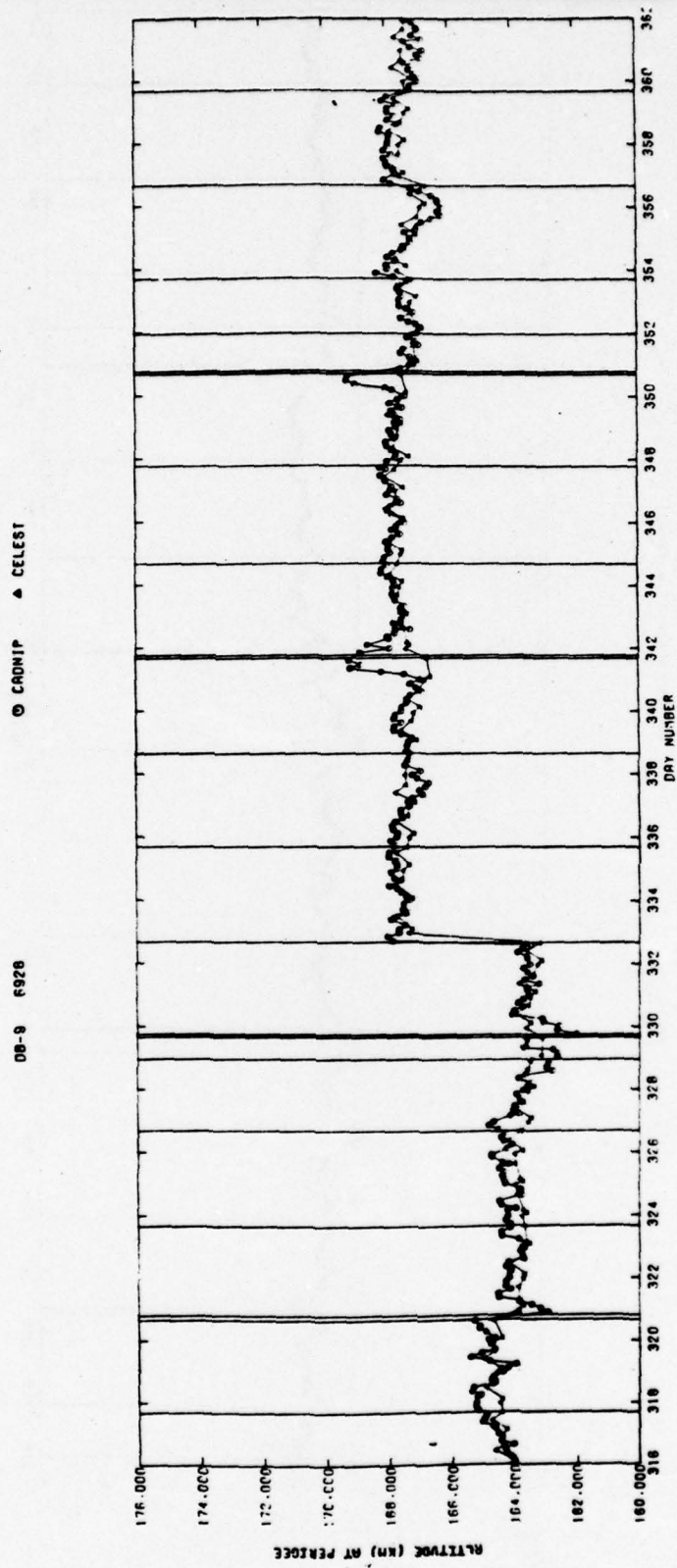
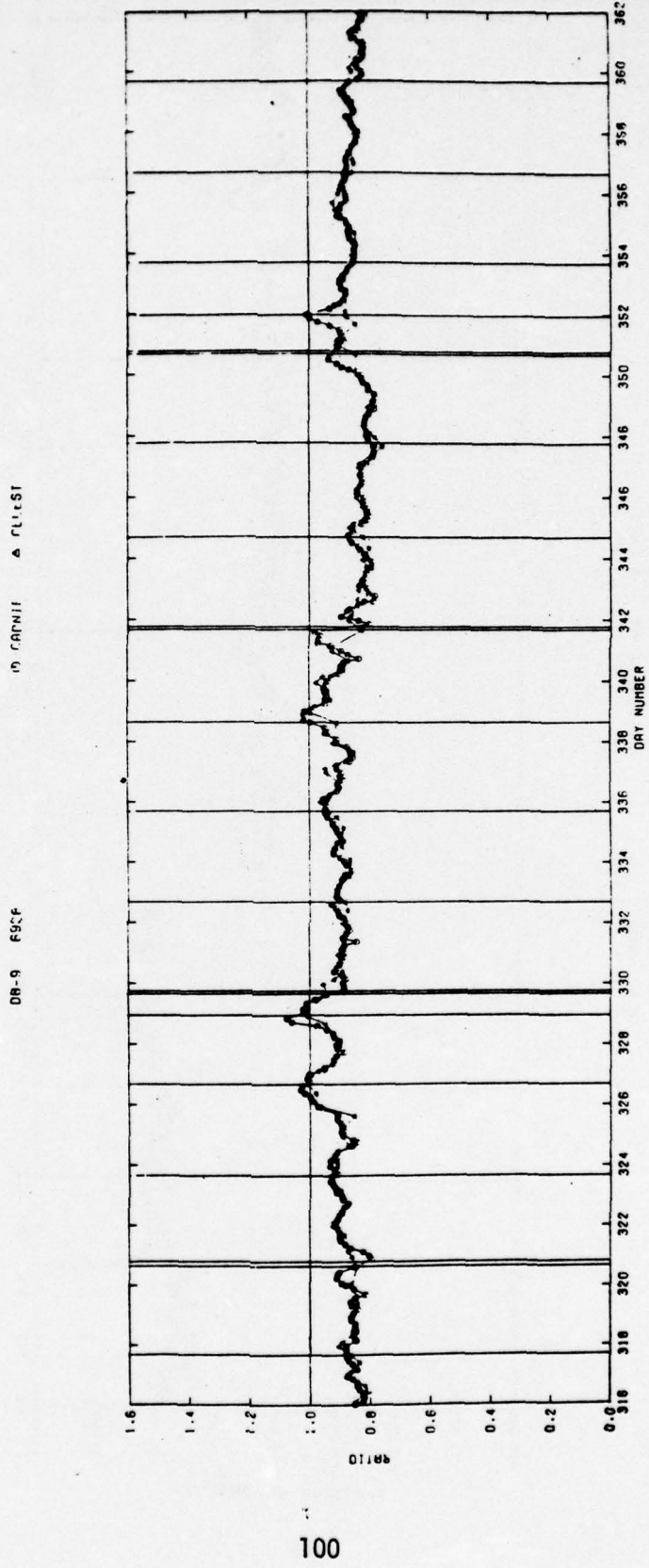


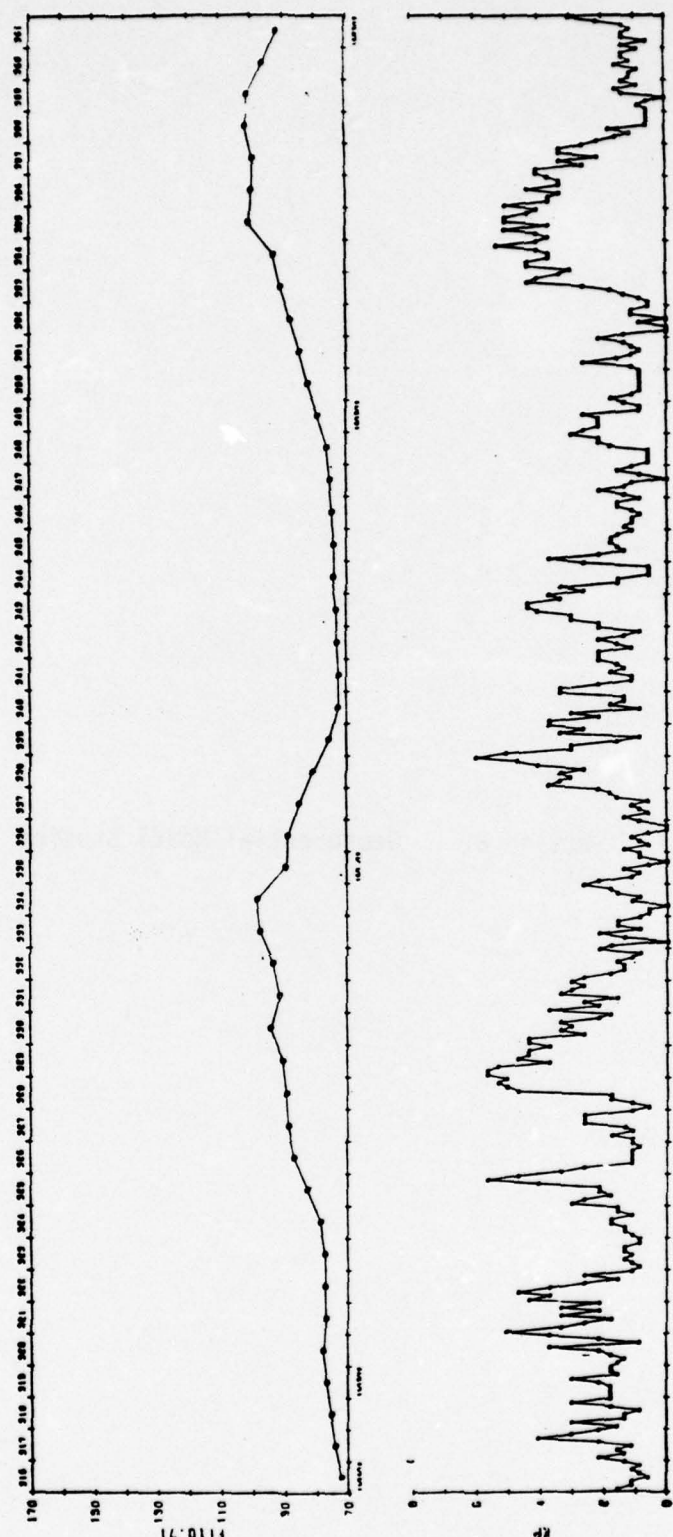
Figure 6. Perigee Heights for Satellite DB-9





100

Figure 7. Model Ratios for Satellite DB-9



101

Figure 8. Solar Flux and K_p Index During DB-9 Flight

Section 8. Geopotential Model Studies

8.0 Geopotential Model Studies

Initiator: K. Champion

Project No.: 427M

Problem No.: 4867

A crucial element in satellite orbit determination is the selection of force models. The most significant forces effecting an artificial close-earth satellite are the Earth's gravitational attraction and atmospheric drag. The determination of the gravitational field (geopotential) in terms of spherical harmonics is straightforward; however a large number of terms are required for accurate representation. On the other hand, lack of knowledge of the dynamics of time dependent atmospheric density variations, particularly in the presence of geomagnetic disturbances, has been a major stumbling block in accurate prediction of satellite position.

It is therefore apparent that, in many cases, particularly low-altitude satellites, the use of large geopotential expansions may not be justified in view of computation time and memory requirements, save for the inclusion of "resonance" terms. It is therefore desirable to know the accuracy of various published geopotential expansions (models), the effects of truncating a model, and the effects of various resonance terms.

The work reported here is a continuation of the geopotential model evaluation underway at AFGL as described by Garrett, et al.⁽¹⁾ Satellites DB-7 (6382), DB-8 (6727), and DB-9(6928) have been chosen for this study, because of the availability of high quality doppler beacon data at AFGL. Thus a comparison of results for different types of data is possible. Several geopotential models are compared as to their orbit determination and prediction capabilities. Modifications by truncation and exclusion of resonance terms are also considered. Uncertainties in Earth contents (geopotential constant, radius, flattening ratio) are also sources of errors in orbit determination and prediction, and are also explored in this report.

8.1 Procedure

Doppler beacon data obtained from Naval Surface Weapons Center (NSWC), Dahlgren Laboratory was processed by program CELEST^(2, 3). Data were fit over approximately 27 hour time spans by least-squares adjustment of 6 orbital parameters and a drag factor. A second fit was obtained in each case for a time-span beginning at approximately the midpoint of the first time span and extending to 16 hours after the end of the first span. Prediction errors were thus obtained from

positional differences between the orbit obtained from the first time span and that obtained from the second.

These procedures were carried out for the geopotentials listed in Table 1 and described in Reference 1, and for time spans, selected for varying levels of geomagnetic activity, listed in Table 2. Constants were input as prescribed for each model. Tests described later however showed that variations of these parameters over the ranges of published values produced little change in the results. The Jacchia 1964⁽⁴⁾ atmospheric density model was used.

Table 1. Geopotential Models

Model	Maximum Degree
Gaposchkin	8
STEM 68R	15
SEIII	23
WGS 72	28
14th Aerospace	12

Table 2. Satellites and Fit Spans Studied

Satellite (perigee Height)	Fit Span (1973)	Average Kp	
		Fit	Prediction
DB7 (157-162 Km)	March 14	1.0	1.0
	March 16	2.5	2.0
	March 18	4.0	6.0
	March 23	5.5	5.5
DB8 (162 Km)	July 26	4.5	4.0
	August 3	1.5	2.0
	August 8	2.5	1.5
	August 10	1.5	1.0
DB9 (164-168Km)	November 14	2.0	2.0
	November 29	1.5	1.5
	December 6	2.5	2.0
	December 22	4.5	4.0

8.2 Results

Prediction errors obtained are typified by Figures 1-3. The most visible features are the general increasing trend of the total and in-track errors, upon which are superimposed oscillations with a period of one orbital revolution. These are due to phase and amplitude differences in the oscillation of true anomoly about mean anomoly for the two approximately elliptical orbits being differenced (See Section 8.3). They are removed by plotting differences in mean anomoly plus argument of perigee (Figure 3). Errors in components perpendicular to in-track were generally less than 200 m.

8.2.1 Statistical Analysis

The total error has been analyzed as described in Reference 1. The following quantities have been computed for each model at 5, 10 and 15 hours beyond the fit span

$$\bar{ER} = \frac{1}{N} \sum_{i=1}^N ER_i$$

$$SD = \sqrt{\frac{\sum_{i=1}^N (ER_i - \bar{ER})^2}{N-1}}$$

$$\bar{|ER|} = \frac{1}{N} \sum_{i=1}^N |ER_i|$$

where ER_i is the total error for the i^{th} case, having the sign of the in-track error.

Tables 3-5 contain the results for 12 cases processed by program CELEST. As expected, the mean total error \bar{ER} is generally small. The more significant quantities, the standard deviation SD and the mean magnitude of error $\bar{|ER|}$ both indicate a marginal preference toward the higher order models SE III and WGS72. This is in general agreement with the results of Reference 1, except for the good performance of the SE III and the poor performance of 14th Aerospace 12 x 12 model. The errors obtained here are also much smaller than those found in Reference 1.

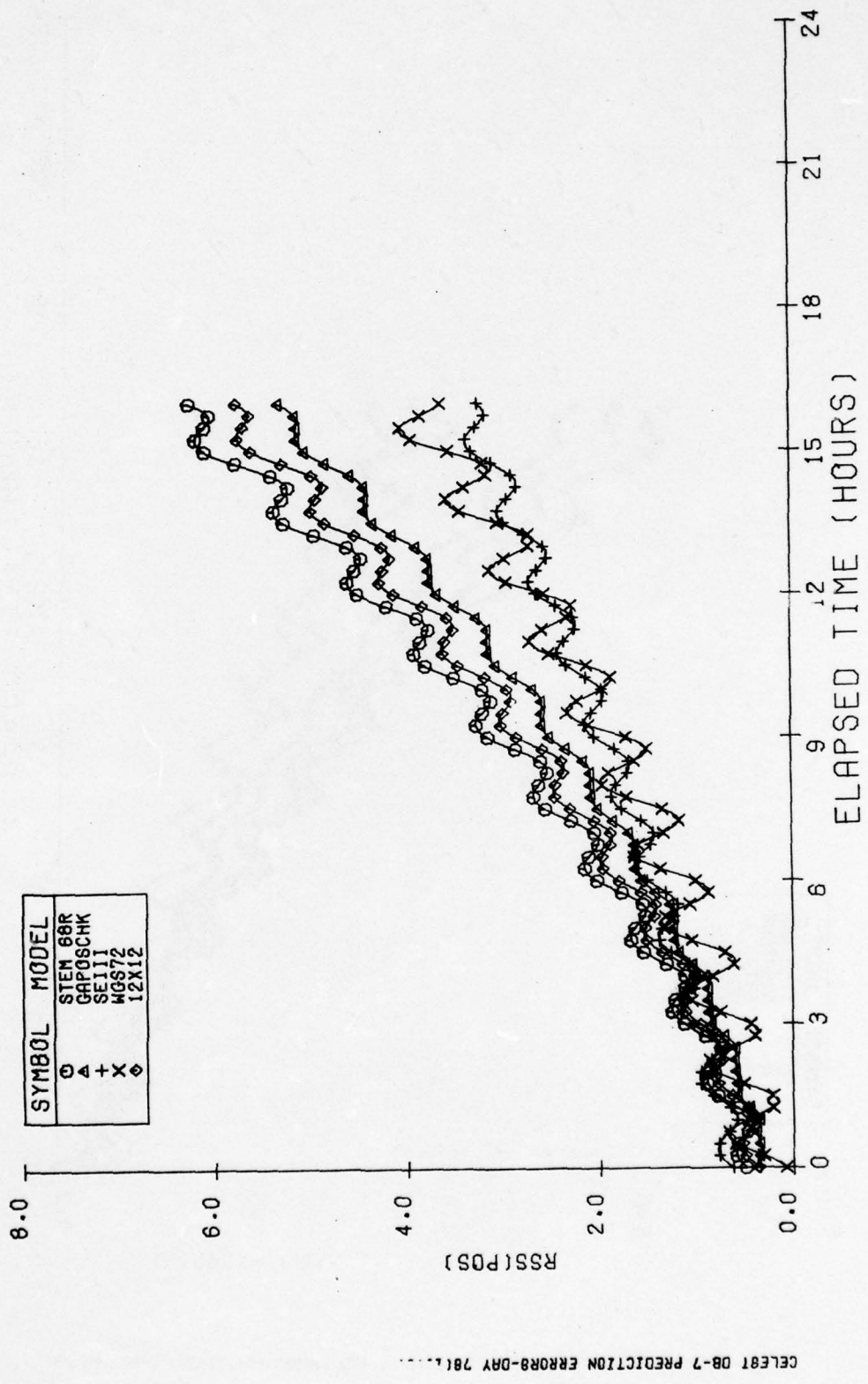


Figure 1. Total Prediction Error (km)-Satellite DB7, Day 76 (1973)

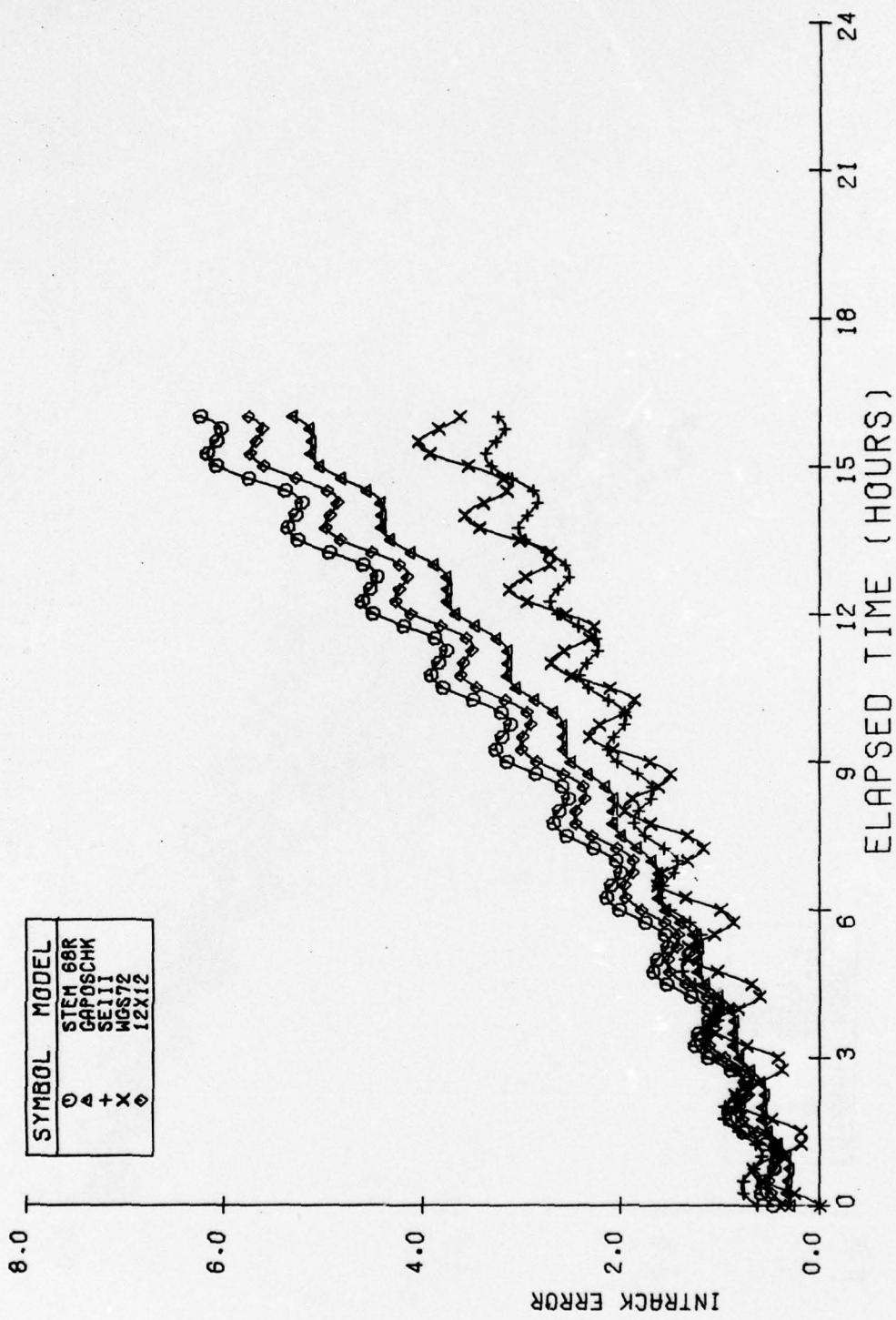


Figure 2. In-track Component of Prediction Error (km)-Satellite DB7, Day 76 (1973)

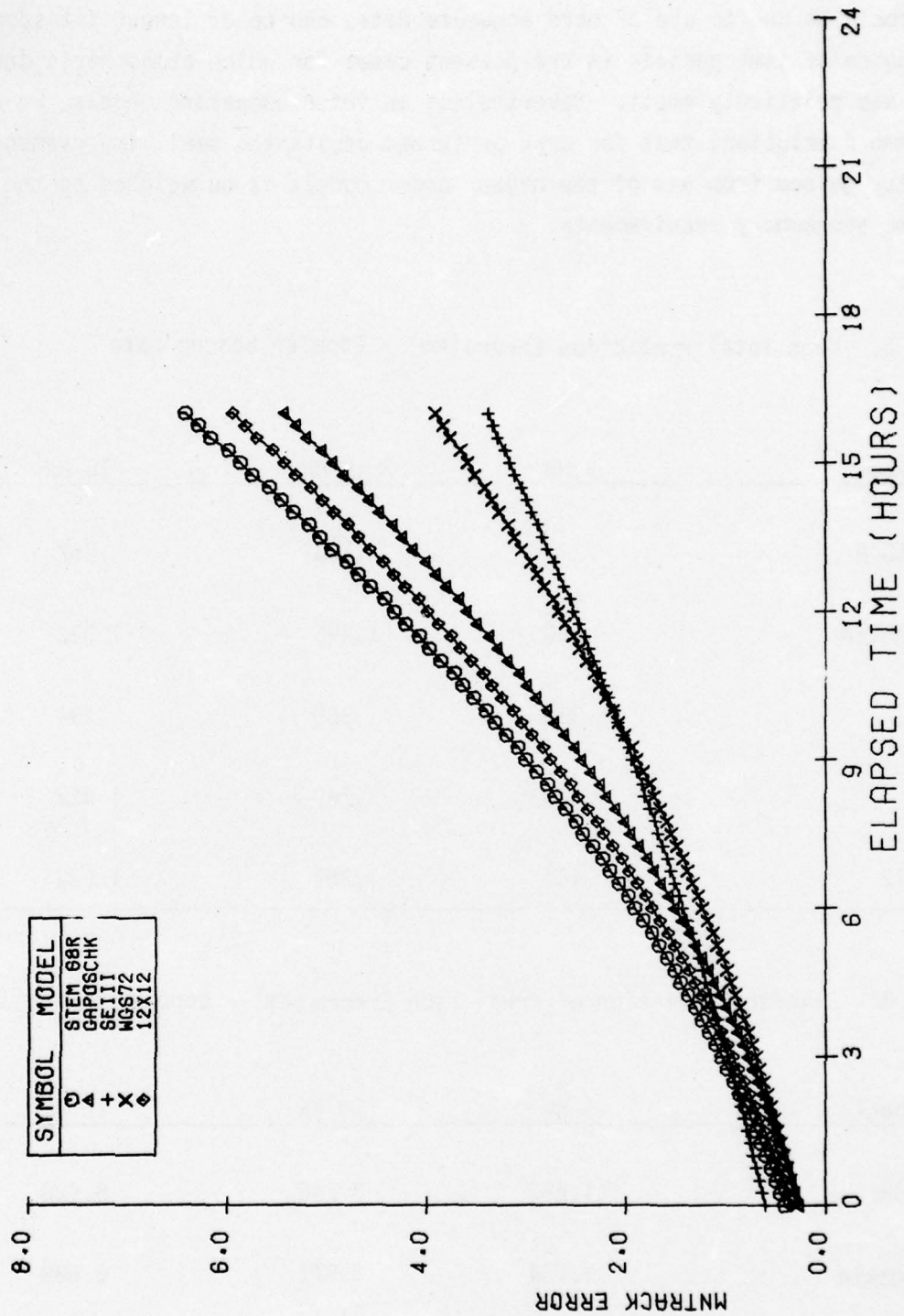


Figure 3. Mean Track Prediction error (km): Product of Semi-major Axis and Error in Sum of Argument of Perigee and Mean Anomaly-Satellite DB7, Day of 76 (1973)

This could be due to use of more accurate data, choice of longer fit spans, or the choice of time periods in the present cases for which atmospheric drag error was relatively small. Nevertheless in inter-comparing models, we reach the same conclusion, that for drag perturbed orbits the small improvement in accuracy gained from use of the higher order models is outweighed by the increase in time and memory requirements.

Table 3. Mean Total Prediction Errors (km) - Doppler Beacon Data

<u>Gp. Model</u>	5 HR	10 HR	15 HR
STEM 68 R	.241	.168	.257
Gaposchkin	.600	1.395	1.332
SE III	.335	.360	.594
WGS72	.425	.749	1.022
12 x 12	.460	1.359	1.322

Table 4. Standard Deviation of Prediction Errors (km) - Doppler Beacon Data

<u>Gp. Model</u>	5 HR	10 HR	15 HR
STEM68R	1.682	3.745	6.628
Gaposchkin	1.654	3.571	6.689
SEIII	1.435	3.030	5.308
WGS72	1.462	3.338	6.074
12 X 12	1.737	3.720	6.969

Table 5. Mean Absolute Value of Prediction Error (km) - Doppler Beacon Data

Gp. Model	5 HR	10 HR	15 HR
STEM68R	1.214	2.499	4.193
Gaposchkin	1.181	2.595	4.436
SEIII	0.930	1.822	3.005
WGS72	1.004	2.084	3.699
12 X 12	1.266	2.630	4.599

8.3 Comparison of Close Orbit Characteristics

Studies of satellite orbit determination programs where the force model, or the set of observations and the time span, or the program itself is varied result in close but not identical orbits which must be compared to evaluate the effects of the variations.

Comparison consists of determining total, in-track (ITE), radial, and cross-track errors between the observed (or reference) orbit and the calculated (or predicted) orbit. Since the trajectories are known in terms of geocentric ECI position and velocity as a function of time, these errors may be directly computed as below.

Let the observed and predicted position and velocity vector components be

$$x_o \quad y_o \quad z_o \quad \dot{x}_o \quad \dot{y}_o \quad \dot{z}_o$$

$$x_p \quad y_p \quad z_p \quad \dot{x}_p \quad \dot{y}_p \quad \dot{z}_p$$

$$\text{Let } v_o = \sqrt{\dot{x}_o^2 + \dot{y}_o^2 + \dot{z}_o^2}$$

The radius vectors are given by

$$R_o = \sqrt{x_o^2 + y_o^2 + z_o^2} \quad \text{and} \quad R_p = \sqrt{x_p^2 + y_p^2 + z_p^2}$$

Then,

$$\text{Total Error} = \sqrt{(x_o - x_p)^2 + (y_o - y_p)^2 + (z_o - z_p)^2} \quad (1)$$

In-Track Error including sign (ITE)

$$= \frac{(x_o - x_p) \dot{x}_o + (y_o - y_p) \dot{y}_o + (z_o - z_p) \dot{z}_o}{v_o} \quad (2)$$

$$\text{Radial Error} = R_o - R_p \quad (3)$$

$$\text{Cross-Track Error (CTE)} = \frac{R_x \dot{x}_o + R_y \dot{y}_o + R_z \dot{z}_o}{v_o} \quad (4)$$

$$\text{Where } R_x = \frac{y_o z_p - y_p z_o}{R_o}, \quad R_y = \frac{z_o x_p - z_p x_o}{R_o}, \quad R_z = \frac{x_o y_p - x_p y_o}{R_o}$$

Positive CTE is in the direction of the orbit spin axis.

Note that the observed and calculated velocity components may be used interchangeably as available, with negligible change in results.

It should be observed that the three error components above do not form an orthogonal coordinate system. This however was not relevant to the studies made here. In-track error in the velocity direction gives a direct timing error which is useful.

(6)

Aerospace's TRACE orbit determination program defines in-track error as

$$\frac{(x_n - x_o) T_x + (y_n - y_o) T_y + (z_n - z_o) T_z}{\sqrt{T_x^2 + T_y^2 + T_z^2}}$$

Where n designates "nominal" orbit and o designates observed orbit, and the vector \vec{T} is given by

$$\vec{T} = (\vec{R}_n \times \vec{V}_n) \times \vec{R}_n$$

The difference between these two definitions of in-track error becomes significant only for highly eccentric orbits where the velocity vector is not normal to the radius vector.

In drag dependent orbit studies, the total error turns out to be almost completely due to the in-track error, while the radial or altitude error and the cross-track error remain consistently small. This in-track error will generally include four components:

- 1) An average in-track error - offset
- 2) Oscillations in the in-track error
- 3) A linear increase in the error
- 4) An exponential component in the error

Figures 1 and 2 show typical total and in-track error computer plots where fit to observed data has been compared to predicted orbit over a 16 hour period for five different geopotential models. The oscillations are clearly evident, and the other three components are present in varying degrees.

Orbit determination programs generally also provide classical orbital elements at one or more epochs. It is possible from a comparison of these elements to quantitatively determine the relative behavior of close orbits over a number of revolutions. The four components of in-track error are primarily due to

differences in the semi-major axis (a), eccentricity (e), argument of perigee (w), mean anomaly (m), and the drag factor (C_D). The inclination and the longitude of the ascending node are factors which primarily affect cross-track error.

In-track error at any time is given by

$$ITE = R(\Delta w + \Delta v) \quad (5)$$

where R = radius vector
 v = true anomaly.

The difference in true anomaly Δv may be expressed in terms of ΔM and Δe using the relationships

$$M = E - e \sin E \quad (6)$$

$$\tan \frac{v}{2} = \sqrt{\frac{1+e}{1-e}} \tan \frac{E}{2} \quad (7)$$

where E is the eccentric anomaly.

If we let $\eta = \tan \frac{E}{2}$ and $\xi = \sqrt{\frac{1-e}{1+e}}$

we obtain

$$\Delta v = \frac{\left(\frac{1+\eta^2}{1-e \cos E} \right) \Delta M + \left\{ \frac{(1+\eta^2) \sin E}{(1-e \cos E)} + \frac{\eta}{1-e^2} \right\} \Delta e}{\xi \left(1 + \frac{\eta^2}{\xi^2} \right)} \quad (8)$$

The differences Δw , ΔM , and Δe coupled with the radius vector R oscillating at the orbit period thus produce the in-track error and its variations.

8.3.1 Estimation of Typical In-track Errors for Low Altitude Satellites.

Application of equations 5 and 8 for an orbit with $a=1.3$ and $e=.2$ shows that differences Δw or ΔM of 0.01, or Δe of 0.0001 result in ITE magnitudes of

about 1 Km. This error is accompanied by oscillations that peak near 180° , 0° , or 90° true anomaly. Further, unless $(\Delta w + \Delta M)$ is nearly zero, an average ITE offset is also associated with these oscillations.

ITE due to Argument of Perigee - Δw

$$\text{ITE}_{\max} = a(1+e)\Delta w \text{ at } M=180^\circ \quad (9)$$

$$\text{ITE}_{\min} = a(1-e)\Delta w \text{ at } M=0^\circ$$

ITE due to Mean Anomaly - ΔM

$$\text{ITE}_{\max} = \frac{a\sqrt{1+e}}{\sqrt{1-e}} \Delta M \text{ at } M=0^\circ \quad (10)$$

$$\text{ITE}_{\min} = \frac{a\sqrt{1-e}}{\sqrt{1+e}} \Delta M \text{ at } M=180^\circ$$

ITE due to Eccentricity - Δe

$$\text{ITE Amplitude} \approx \frac{a(3+2e)}{2} \sqrt{1-e^2} \Delta e \quad (11)$$

Max for $v \approx 90^\circ$; min for $v \approx -90^\circ$.

Differences Δa and ΔC_D result respectively in linear and exponential growth in ITE. The latter phenomenon is essentially caused by a linear growth in Δa due to differing drag or atmospheric density models for the two orbits.

ITE due to Semi-Major Axis - Δa

$$\Delta \text{ITE per revolution} = -3\pi \Delta a. \quad (12)$$

Thus a 0.1 Km difference causes a 1Km per revolution build up in ITE.

ITE due to Drag Coefficient - ΔC_D

The monotonic decrease in 'a' and the orbital period is due to the drag. The ratio $\Delta C_D/C_D$ gives the portion of this rate of change of 'a' that will persist and show up as a near parabolic increase in ITE. If f is the fraction decrease per day in the semi-major axis, and n is the orbital period in revolutions per day,

ITE value attained in one day

$$= \frac{\Delta C_D}{C_D} \cdot \frac{3}{2} \pi f n a \quad (13)$$

Thus, for $a = 1.3$, $n = 11.5$ revs/day and semi-major axis decay rate of 0.1% per day, a 1% difference in the drag coefficient will show up as an ITE of 4.5 Km after one day.

8.4 Resonant Terms

It is evident from the results obtained here that one may indeed often reduce the size of the geopotential model without adversely affecting prediction accuracy. To gauge the extent to which a geopotential can be reduced and to see which terms may be omitted it is useful to have a method of estimating the influence of individual geopotential terms on prediction accuracy.

8.4.1 Geopotential

As stated previously the geopotential is expressed as an expansion of spherical harmonics

$$V(r) = -\frac{GM}{r} \left[1 + \sum_{l=2}^{\infty} \sum_{m=0}^{l} \left(\frac{a_e}{r} \right)^l P_l^m (\sin \chi) \cdot \left(\sum_{l_m} \cos m\gamma + S_{l_m} \sin m\gamma \right) \right]$$

where

GM = Earth's gravitational constant

r = radius vector

a_e = radius of earth

X = latitude

Y = longitude (East)

P_{ℓ}^m = associated Legendre function

8.4.2 Influence of Individual Terms

The effects of individual geopotential terms on satellite orbits fall into 2 classes⁽⁵⁾

1) Secular ($m=0$ only)

2) Periodic

$$A \cos 2\pi f t$$

$$f = (\ell - 2p) \dot{\omega} + (\ell - 2p+q) n + m (\dot{\Omega} - \dot{\theta})$$

where

$\dot{\omega}$ = precession in argument of perigee

$\dot{\Omega}$ = precession in ascending nod

$\dot{\theta}$ = sidereal rotation rate of Earth

p = integer ($0 \leq p \leq \ell$)

q = integer ℓ

$$\frac{A e e^{|q|}}{f}$$

e = eccentricity

The most important of the secular corrections comes from the $\ell=2$, $m=0$ term since c_{20} is 1000 times as big as the higher order coefficients. These include the precession of perigee and ascending node appearing in the periodic effects.

The amplitudes A of the periodic effects are functions of the orbital elements, which are slowly varying; hence A may be considered constant over sufficiently short time spans. Since ω and Ω are much smaller than n or $\dot{\theta}$ it is evident that resonance occurs for

$$n \text{ (revolutions/day)} \approx m.$$

Thus the DB satellites (16.2 revs/day) are near resonant for $m=16$ terms in the geopotential.

8.4.3 Effects on Predicted Orbit

The resulting influence of a particular geopotential term on a predicted orbit based on least-squares adjustment of orbital parameters is given by

$$de(t) = \left(\Phi \frac{\partial P}{\partial C} + \frac{\partial e}{\partial C} \right) c$$

where

$$e = \begin{pmatrix} e_1 \\ e_2 \\ \vdots \\ \vdots \\ e_6 \end{pmatrix}$$

$e_i = i^{\text{th}}$ orbital element

$$\Phi = \begin{pmatrix} \frac{\partial e}{\partial P_1} & \dots & \frac{\partial e}{\partial P_n} \\ \vdots & & \vdots \\ \vdots & & \vdots \\ \frac{\partial e_6}{\partial P_1} & \dots & \frac{\partial e_6}{\partial P_n} \end{pmatrix}$$

$$P = \begin{pmatrix} P_1 \\ \cdot \\ \cdot \\ \cdot \\ P_n \end{pmatrix}$$

$P_i = i^{\text{th}}$ orbital parameter

C = coefficient of geopotential term

The first term accounts for the dependence on the geopotential of the orbital parameters obtained in a least squares fit, while the second term is directly obtainable from the perturbation theory described in 8.4.2.

8.4.4. Dependence of Orbital Parameters

It is assumed that the change in orbital parameters due to omission of a term in the geopotential will be such as to provide a least squares-adjustment to the perturbations in the orbit due to that term.

Since the dominant prediction errors are in-track (Figures 1-3) we concentrate on this component. We assume a 3-parameter fit function for in-track position.

$$S(t) = \sum_{i=1}^3 P_i t^{i-1}$$

with P_1 representing the initial orbital longitude, P_2 proportional to the mean motion (function of the semi-major axis), and P_3 proportional to the rate of change of mean motion, as produced by atmospheric drag.

It is evident that secular corrections mentioned in 8.4.2 will be fit perfectly in so much as they are limited to first time derivatives of the elements. Their effects on the predicted orbit would thus cancel out. We therefore concentrate on the periodic corrections.

Then we find that the changes dP_i due to a periodic orbital term $A \cos(at + q_0)$ are

$$dP_1 = -\frac{A}{aT} \left[12(2 \sin q - 3 \sin q_0) + \frac{1}{aT} (2 \cos q + 3 \cos q_0) \right. \\ \left. - \frac{60}{(aT)^2} (\sin q - \sin q_0) \right],$$

$$dP_2 = \frac{A}{aT^2} \left[12(2 \sin q - 3 \sin q_0) + \frac{1}{aT} (168 \cos q + 192 \cos q_0) \right. \\ \left. - \frac{360}{(aT)^2} (\sin q - \sin q_0) \right],$$

$$dP_3 = -\frac{A}{aT^3} \left[30(\sin q - \sin q_0) + \frac{180}{aT} (\cos q + \cos q_0) \right. \\ \left. - \frac{360}{(aT)^2} (\sin q - \sin q_0) \right],$$

where

T = length of fit span,

$q = aT + q_0$.

8.4.4 Results

Figure 4 shows the rms change in prediction error (averaged over phase q_0).

It is seen to depend on the ratio of fit span T to the period of the perturbation, and the ratio of the prediction time measured from the end of the fit span to the fit span T . The effect on prediction error is largest for those perturbations with periods nearly equal to the fit span. This is illustrated in Table 6. Satellite DB7 has a mean motion of 16.2 revs/day and is thus near-resonant for $m=16$ terms (principal perturbation has 5 day period.). The $m=17$ terms contribute a perturbation with a 30-hour period.

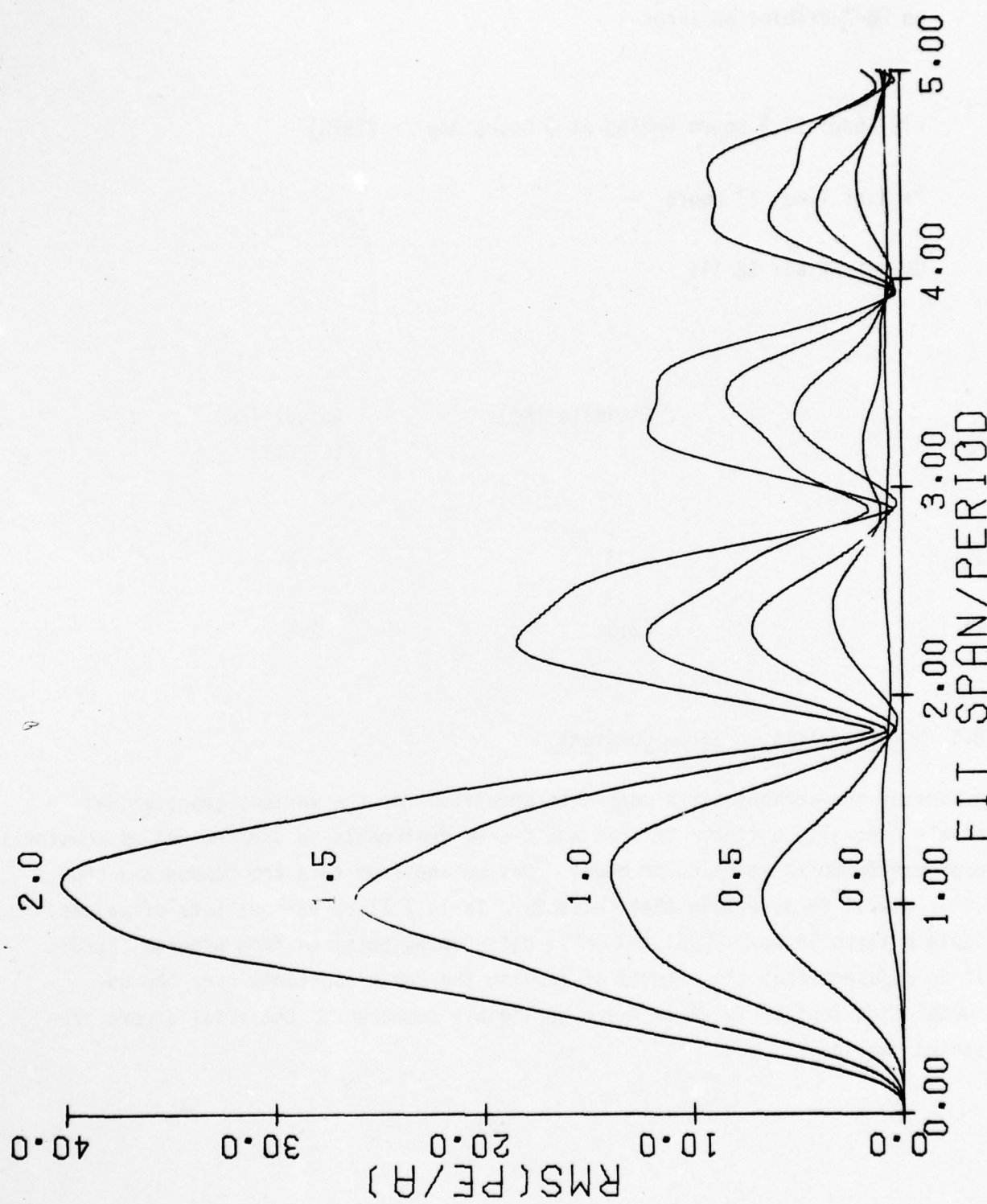


Figure 4. R.M.S. of the Ratio of Prediction Error Effect to Perturbation Amplitude for Periodic Perturbation. The number above each curve is the ratio of predict time, measured from the end of the fit span, to the length of the fit span.

Table 6. Influence of $m = 16$ and 17 Terms
on DB-7 Prediction Error

Fit Span: 27.5 hours ending at 0 hours day 76 (1973)

Predict Time: 17 hours

Geopotential: SE III

m	Estimate (Km)	Actual (Km) (CELEST)
16	- .3	- .5
17	-2.3	-2.5

8.5 Uncertainties in Earth Constants

Values of the various Earth constants specified for the various geopotential models generally differ. Thus it would seem desireable to use the set of constants appropriate to the particular model. Deviations from this are common and thus it is useful to ascertain their effects. Table 7 lists various sets of values. Table 8 lists 16-hour predicted orbit differences obtained from program CELEST. It is apparent that the effects of varying the Earth constants over the uncertainties implied in Table 7 are negligible compared to the total errors presented earlier.

Table 7. Earth Constants

	a_e^a (km)	$1/f^b$	GM (km ³ /sec ²)
Gaposchkin	6378.145	298.25	398601.2
STEM68R	6378.145	298.25	398601.2
SE III	6378.140	298.256	398601.3
WG\$72	6378.135	298.26	398600.5
14 th Aerospace 12 x 12	6378.145	298.25	398601.2

^aEquatorial Radius

^bFlattening Ratio

Table 8. Effect of Constant Changes on SE III Fit and Predict

Δa_e^a (m)	5	-5	5
Δf^{-1}	-.0005	.004	-.006
ΔGM (km ³ /sec ²)	0	0	-.8
Δx_0^b (m)	1	-1	4
Δy_0 (m)	0	1	-3
Δz_0 (m)	-1	-1	-1
Δx_1^c (m)	2	5	1

Table 8. (continued)

ΔY_1 (m)

0

-3

2

ΔZ_1 (m)

-1

0

4

a Measured from SE III constants (row 3 of Table 7)

b From fit initial conditions 8/11/73 20 hr 40 min. for satellite DB-8

c From predicted position 8/13/73, 16 hr. for satellite DB-8

Geopotential coefficients for orbit determination programs are encountered with 3 types of normalization in common practice:

- 1) Unnormalized
- 2) APL or partially normalized
- 3) Kaula or fully normalized

Expressions relating the coefficients for the various normalizations are:

$$\begin{aligned} C_{nm}^A &= \sqrt{\frac{(n+m)!}{(n-m)!}} C_{nm}^U \\ C_{nm}^K &= \sqrt{\frac{(n+m)!}{(2n+1)(2-\delta_{m0})(n-m)!}} C_{nm}^U \\ C_{nm}^K &= \sqrt{\frac{1}{(2n+1)(2-\delta_{m0})}} C_{nm}^A \end{aligned}$$

Where the superscripts U, A, K imply unnormalized, APL-normalized and Kaula-normalized coefficients respectively, and

$$\begin{aligned} \delta_{m0} &= 1, m = 0 \\ &= 0, m \neq 0 \end{aligned}$$

The unnormalized coefficients only are required by CELEST and CADNIP, while any of the 3 may be used in TRACE provided the flag NFORM is properly set. The APL normalization was used by Guier and hence applies to the Guier deck.

Most labs (SAO, Spacetrack, NSWC) seem to prefer the Kaula normalization. Hence it must be determined what normalization has been used for each deck transmitted to us from the outside.

A word of warning: in some cases, the normalization of zonals ($m=0$) is not the same as non-zonals, rather the J_r coefficients

$$J_n = -C_{n0}^U$$

are given while APL or Kaula normalization is used for the non-zonals. Thus the well-defined (2,0) coefficient should always be checked in addition to the normalization.

References

- 1) H. B. Garrett, 1 Lt., USAF, J. M. Forbes, and K. S. W. Champion, (U) Geopotential Model Effects on Low-Altitude Satellite Ephemeris Prediction, AFGL-TR-76-0014 1976.
- 2) Naval Surface Weapons Laboratory (Dahlgren, VA), CELEST Working Papers (unpublished).
- 3) James N. Bass, Krishin H. Bhavnani, and Isabel M. Hussey, Atmospheric Density Determination from Analysis of Doppler Beacon Satellite Data, AFCRL-TR-75-0716, 1975.
- 4) L. G. Jacchia, Static Diffusion Models of the Upper Atmosphere with Empirical Temperature Profiles, Smithsonian Astrophysical Observatory Special Report No. 170, 1964.
- 5) W. M. Kaula, Theory of Satellite Geodesy, Blaisdell Publ. Co., Waltham, MA., 1966.
- 6) TRACE, Trajectory Analysis and Orbit Determination Program, The Aerospace Corp., SAMSO-TR-71-141, (1974).

Section 9. Rocket Trajectory System

9.0 Rocket Trajectory System

Initiator: E. Robinson

Project No.: 0001

Problem No.: 4517

In parallel with a continuing active use of the AFGL Rocket Trajectory System, requirements for improvements in nearly all phases of this system were identified. A combined report and user's guide is in preparation⁽¹⁾ in order to present a current document of procedures and pertinent analytical backup. Significant additions and changes since the last report⁽²⁾ are outlined here.

9.1 Editor - Preprocessor (DRIVEA)

Occasionally the raw radar data contains biases or extended deviations in range, azimuth or elevation which are discernible by inspection of the preprocessed plots. A capability was implemented in DRIVEA to specify one or more time spans over which it is desired to bridge any one or more of these measurements by a smooth spanning cubic polynomial. The cubic satisfies readings at the two times specified plus two readings 5 seconds outside the span of discarded readings.

9.2 Filter (DRIVEB)

The main developmental effort took place in this area where statistical filtering, rocket dynamics modeling, digital integration, and output considerations are combined.

9.2.1 Operating Modes

Figure 1 shows the types of operation of DRIVEB that are available by input of the variable KEYOPT. Inputting of TB, TC, TE, and TF relative to TLNCH and TSTART establishes regions for the consecutively numbered integrating, filtering, or reproducing phases. Geocentric position and velocity initial conditions are required, except that launch azimuth and elevation can replace velocity information at launch. KEYOPT = 3 provides a run identical to the original DRIVE 3 run, and KEYOPT = 4 matches the original DRIVE5. KEYOPT = 1 is normally used now and is discussed below.

9.2.2 Integration - Filtering Mode

Reliable radar data is generally not available till some time into launch. The original DRIVE 3⁽³⁾ and DRIVE 5⁽²⁾ programs filtered data from some preselected time on, and attempted to obtain the trajectory from launch to that time by integrating backwards.

KEYOPT	Type of Run	T0	T1	T2	T3	Geoc. Position PV(1-3) km.	Geoc. Velocity PV(4-6) km/sec.
		Forward Integ. Limit.	End Filter	TF	TE	use Launchcoords.	If PV(5)=Launch Elevation PV(4)=Launch Azimuth In If PV(6)=0, use Launch coords.
0	Pure Integ.	INTEG3	INTEG1	INTEG2			
2	Data Reprod.	INTEG3	REPROD1	INTEG2			
3	Single Filter	INTEG3	FILTER1	INTEG2			
4	Double Filter	INTEG4	FILTER1	INTEG2			
1	Normal Integ-Filter (optimize launch conditions to time TC) -1	INTEG1	FILTER3 FILTER2	INTEG3			
			FILTER4				

NOTE 1: For KEYOPT=1 (or -1), since launch conditions are required,

If PV(6)=0 and launch AZ, EL are given; PV(1-3) are ignored.

If PV(6)≠0, PV(1-3) at time TC are used to estimate launch AZ, EL; and PV(4-6) are ignored.

TB is ignored in either case.

NOTE 2: Filter time points are trimmed internally to correspond to data sample times; except when pure integrating, when the time points correspond to TC. Numbers after functions indicate execution sequence.

Figure 1. Description of DRIVEB Filter Time Limits, KEYOPT, Geoc. Position & Velocity Card Input.

This procedure inevitably leads to an unresolvable mismatch at launch. The solution to this is to search for proper launch conditions so as to achieve the closest possible match to subsequent radar position information. Then "pseudo" radar data is generated from launch allowing a full filtering run with no backward integration. The search for optimum launch determines thrust ratio (fraction of nominal), launch azimuth and elevation, and time delay before onset of the thrust phase. The square sum of the residuals of geocentric coordinates at three time points near the start of good radar data is minimized iteratively.

Briefly, let m be the number of variables being optimized and n the number of observations ($n > m$). Let x_0 be the vector of initial settings of the m variables. The corresponding residual vector for the n observations is $(r_{01} \ r_{02} \dots \ r_{0n})$. m separate trials are carried out with small increments in the m variables one at a time. Let these increments be given by $\Delta q_1, \Delta q_2, \Delta q_m$, where q_i is in the units of x_i . The augmented $(m+1)xn$ residual matrix R is

$$R = \begin{bmatrix} r_{01} & r_{11} & \cdots & r_{m1} \\ r_{01} & r_{1n} & \cdots & r_{mn} \end{bmatrix}$$

Solve for q from

$$\tilde{R}R \begin{bmatrix} q \\ q_1 \\ \vdots \\ q_m \end{bmatrix} = 0$$

where \tilde{R} is the transpose of R and $q_0 + q_1 + \dots + q_m = 1$ since the optimization is to be an adjustment about x_0 .

Then, if the x_i are changed by $q_i \Delta x_i$, the original residual vector r_0 will be minimized in a least squares sense. Since the rocket trajectory is a non-linear process the optimization is generally iterative. The m trials provide the necessary partials without analytic methods, and are considered applicable to successive iterations. Taking each of the rectangular

coordinates as an independent observation, the result is the minimization of spatial separation between the observations and the computed trajectory.

Highly satisfactory results have been obtained with consistent values of thrust ratio and delay when fitting to the radar data at different times. Additional process "unknowns" such as wind can be added to the search as experience identifies and warrants these variables.

9.2.3 Driving Noise Uncertainty \mathbf{Q}

The driving noise uncertainty in the velocity vector was originally taken to be proportional to $(ACC \times DT)^2$ where ACC is the instantaneous acceleration and DT is the integration step size. Corresponding position vector uncertainty is

$$Q_p = Q_v \sqrt{(DT^2/4)}$$

It was found that the dynamic model was more unreliable at re-entry since the integration - filtering mode alleviated the launch data uncertainty. Q_v is now taken as proportional to $OVR \sqrt{|ACC| \cdot DT^2}$ where OVR is the vehicle range. Q_p is calculated as before.

9.2.4 Rocket Dynamics Modeling

Drag coefficient determination as a function of Mach number has been refined. The universal curve

$$C_D = 1.0 + \frac{1}{V_{mach}}^4 \quad (V_{mach} \leq 1)$$

$$C_D = \frac{4.0}{V_{mach} + 1.0} \quad (V_{mach} \geq 1)$$

is multiplied by a rocket and stage-dependent C_D multiplier. V_{mach} is given by V_{rocket}/V_{sound} . The U.S. Standard Atmosphere, 1962 provides a piece-wise linear estimate of the speed of sound as a function of altitude and this has been incorporated satisfactorily.

Thrust, mass and drag characteristics of additional rockets were added to the file. The repertory with rocket key numbers is given in Table 1. Test integration runs and adjustments have been made in several cases based on computer runs provided with the nominal specifications.

Table 1.

Rocket	Key
AEROBEE 150	03
AEROBEE 170	04
NIRO	07
NIKE TOMAHAWK	08
UTE TOMAHAWK	09
PAIUTE TOMAHAWK	10
BLACK BRANT IV-B	16
BLACK BRANT V -A	17
BLACK BRANT V -B,C	18
JAVELIN	19
NIKE JAVELIN	20
NIKE HYDAC	11
SERGEANT-EXCEDE	25
ASTROBEE D	30
AEROBEE 350	35
CASTOR	40
CASTOR-LANCE	41
-----	-----
ARBITRARY UNPOWERED	NONE

9.2.5 Integration Step Size

Some raw radar data tapes were received with samples at 1 second rather than the usual 0.1 second intervals. It was found that if the integration step size was allowed to increase to this data rate, there was a significant build up of error in the 4th order Runge-Kutta integration procedure. Step size less than 0.1 second resulted in negligible change. Subroutine RK was consequently modified to loop a selectable number of times with a specified step size. The maximum step size is set at 0.1 second.

9.2.6 Output Report Data File

The format of the output tape was substantially revised in order to a) include all possible trajectory variables that were desired b) allow REGEN to run using WRITER with no further computations. The original TAPE 8 and TAPE 9 data has been concentrated onto TAPE 4, with a header that minimizes card input with REGEN or DRIVE C (previously DRIVE 4). Table 2 gives the format. Subroutine GENER 8 now calculates the trajectory and residuals in geocentric, launcher, and radar coordinate systems, instead of only the ones selected for printing. The resulting TAPE 4 may be used by WRITER either immediately in DRIVE B or DRIVE C, or subsequently in REGEN. (See Table 2.)

9.3 Multi-Radar Trajectory (DRIVE C)

Program DRIVE C was developed as a revision of program DRIVE 4⁽³⁾. The card input requirements are greatly reduced, using instead the header information on TAPE 4 generated in program DRIVE B (TABLE 2).

The primary function of the multi-radar program is to combine the results of two separate radar observations of a given rocket flight to give a composite trajectory. The methods used to accomplish this data combination are linear; therefore, an arbitrary number of different sets of radar data pertaining to the same flight may be combined by repeated execution of the program. The graphical, printed report and file outputs of this program are identical in all respects to the outputs of Program DRIVE B.

Specific functions of Program DRIVE C include the following:

- Process two input files to produce a single composite trajectory written on an output file

Table 2.

Output Report data file written on TAPE 4. The first record contains flight information for use by Program Regen, which reproduces printed and plotted output. The remaining records contain data to be printed and plotted by either DRIVE C subroutines or by REGEN. If IOPT=1, all data points are written on TAPE 4, if IOPT=0, every ISKIPTH point is written.

FIRST RECORD		
WORD(S)	SYMBOL	DESCRIPTION
1-8	TITLE (1-8)	80 character alphanumeric identification
9-10	DAT(1-2)	Run date, blank
11-16	TITLE 2(1-4)	Further identification
	TITLE 2(5-6)	Payload (KG), Rarea (KM**2)
17-20	DAT(3)	CD
	DAT(4)	Launch date
21-23	DAT(5-6)	Rocket ID
24	HRAD	Height of radar
25	RLODEG	
26	RLOMIN	
27	RLOSEC	Radar position
28	RLADEG	
29	RLAMIN	
30	RLASEC	
31	AALT	Launcher altitude
32	ALODEG	
33	ALOMIN	
34	ALOSEC	
35	ALADEG	Launcher position
36	ALAMIN	
37	ALASEC	
38	UHRS	
39	UMIN	Universal time

40	USEC
41	DT
42	TLI
43	TLF
44	TSKIP

Initial print time from launch
Final print time from launch
Tape written every TSKIP secs.

Table 2. (cont'd)

SUBSEQUENT RECORDS

WORD(S)	SYMBOL	DESCRIPTION
1	GMT	Universal Time (Hours)
2	TIME	Time After Launch (Seconds)
3	SN	Signal to Noise Ratio
4	RAG	Right Ascension of Greenwich(RAD)
5-7	P2(1-3)	Geocentric Position Components(Filtered)
8-10	P2(4-6)	Geocentric Velocity Components(Filtered)
11-13	ACC(1-3)	Geocentric Acceleration(Filtered)
14-16	ACC(4-6)	Magnitudes of Geocentric Vectors
17-19	OVR(1-3)	Radar Range, AZ, EL (Filtered)
20-22	OVR(4-6)	Radar Range, AZ, EL Rates(Filtered)
23	GEOALT	Altitude Above Sub Earth Point
24	GEOLON	Longitude of Sub Earth Point
25	GEOLAT	Latitude of Sub Earth Point
26-28	GPV(4-6)	Geocentric Spherical Coordinates
29-64	XSI(1-36)	Complete Error Covariance Matrix
65-67	DVR(1-3)	Raw Data Vector Range, AZ, EL
68	RANGE	Ground Range Along Spheriod
69	RESALT	Altitude Residual (Raw-Filtered)
70-72	XR,YR,ZR	Radar Centered Coordinates
73-75	XL,YL,ZL	Launcher Centered Coordinates
76	RLMAG	Filtered Launcher Vector Residuals
77-79	SRSG,YRSG,ZRSG	Geocentric Position Vector Residuals
80	GRSG	Geocentric Vector Magnitude Residual
81-83	XRSL,YRSL,ZRSL	Launcher Position Vector Residuals
84	GRSL	Launcher Vector Magnitude Residual
85-87	XRSG,YRSG,ZRSG	Radar Position Vector Residuals
88	GRSR	Radar Vector Magnitude Residual
89-91	P2(4-6)	Geocentric Velocity Component

Table 2. (cont'd)

92-94	DVG(4-6)	Launcher Velocity Components
95-97	OVR(4-6)	Radar Velocity Components
98	RRMAG	Radar Range Magnitude [$=OVR(1)$]
90	ALT	Raw Altitude

- Determine the type of data region being read for each file
- Use the region types to select proper mode for combination equations
- Evaluate combination equations, depending on the particular mode, to produce the composite observation vector and covariance matrix
- Complete the calculations for the remainder of each output file record using composite values
- Generate a printed summary of the combination process, i.e., an event log for the resulting output file
- Produce an output tape file containing the composite trajectory
- Generate printed and graphical reports in the same format as DRIVEB.

For each radar tracking coverage of a rocket a conventional DRIVEB trajectory vector $P(k)$ with its associated error covariance matrix $\Psi(k)$ is generated for each time point k . Two radar tracks of the same rocket may be statistically merged using DRIVEC to provide the best estimate

$$\hat{P}(k) = [\Psi_1^{-1}(k) P_1(k) + \Psi_2^{-1}(k) P_2(k)] [\Psi_1^{-1}(k) + \Psi_2^{-1}(k)]^{-1}.$$

The associated joint error covariance matrix is given by

$$\hat{\Psi}(k) = [\Psi_1^{-1}(k) + \Psi_2^{-1}(k)]^{-1}.$$

This program now operates in only one of two basic modes. When filtered or integrated data is available on both tapes the above merging procedure applies. Filtering and integration regions are not distinguished except through the error covariance matrices. When data is absent on one tape the parameters from the other tape are directly copied. Check-out of the system was underway, with promising early results.

9.4 Operating System

The rocket trajectory operating system was modified to reduce the need for complete binary programs of DRIVEA, DRIVEB, DRIVEC, and REGEN. The SCOPE - EDITLIB facility is used to provide one binary library for all subroutines. The main program with the LIBRARY instruction then causes unsatisfied externals to be loaded. Program maintenance thus requires only one file of source routines in UPDATE form.

References:

- (1) Bhavnani, K.H. and Robinson, E.C., "Functional and Operational Advances in the AFGL Rocket Trajectory System - I" AFGL Technical Report (to be published).
- (2) "Analysis and Programming for Scientific Research", Logicon, Inc. Final Report, AFCRL-TR-74-0480, September, 1974.
- (3) Schonbein, William R., "Analysis of Rocket Trajectory Data from Tracking Radars," AFCRL Technical Report No. 72-0679, 1973.

Section 10. Satellite Wire-Boom Dynamics

Section 10.0 Satellite Wire-Boom Dynamics

Initiator: M. Smiddy

Project No.: 8617

Problem No.: 4702

For the purpose of control information, mode frequencies determination, stability analysis, and damping characteristics, a comprehensive mathematical analysis and digital computer simulation on coupled satellite-boom dynamics has been performed. Since the full details are reported elsewhere (1, 2, 3, 4), only the salient features of this work are outlined in this chapter.

The dynamics of a satellite boom system is generated from its Lagrangian⁽⁵⁾. For dynamics in the spin plane, the Lagrangian L is derived as

$$L = L_0(\dot{\theta}, \dot{x}, \dot{y}) + \sum_{i=1}^4 L_i(\dot{\theta}, r_i, \dot{r}_i, \dot{\theta}_i, \dot{\phi}_i, \dot{x}, \dot{y}), \quad (1)$$

where L_0 is the Lagrangian of the hub, L_i is that due to pure rotation, L'_i is that due to cross effect of rotation-translation, the arguments of the Lagrangians are the canonical variables, dots denote time derivatives, and subscript i labels boom number. The time development of the dynamics of the system is determined by the Lagrangian equations of motion, viz.,

(a) the hub equation: $\frac{d}{dt} \frac{\partial L}{\partial \dot{\theta}} - \frac{\partial L}{\partial \theta} = -K_\theta \dot{\theta}, \quad (2)$

(b) the boom equations: $\frac{d}{dt} \frac{\partial L}{\partial \dot{\theta}_i} - \frac{\partial L}{\partial \theta_i} = -K_{\theta_i} \dot{\theta}_i \quad (i=1, \dots, 4) \quad (3)$

(c) the tension equations:

$$\frac{d}{dt} \frac{\partial L}{\partial \dot{r}_i} - \frac{\partial L}{\partial r_i} = -T_i \quad (i=1, \dots, 4) \quad (4)$$

and (d) the translation equations:

$$\frac{d}{dt} \frac{\partial L}{\partial \dot{x}} - \frac{\partial L}{\partial x} = 0, \quad (5)$$

and

$$\frac{d}{dt} \frac{\partial L}{\partial \dot{Y}} - \frac{\partial L}{\partial Y} = 0. \quad (6)$$

where L is given in Equ. (1).

The algebraic details of the above equations are rather lengthy⁽¹⁾. . However, these coupled nonlinear differential equations can be solved simultaneously and numerically using Hamming's predictor-corrector method⁽⁶⁾. The solutions represent the time development of the canonical variables of the system, depending on various given initial and boundary conditions.

Figure 1 displays the development in time of the canonical variables under typical initial and boundary conditions.

Analytically, the Lagrangian equations Equs. (2) to (6) can be solved for harmonic oscillation modes. Matrix formulation of the eigenvalue equation is used. Simultaneous diagonalization of the kinetic and potential energy matrices (with dimensions 7x7) yield the eigenvectors and the mode frequencies. Table 1 summarizes the analytical results of harmonic (normal) modes in the spin plane.

Due to the presence of a very effective wobble damper, oscillations out of the spin plane are negligible⁽⁷⁾. However, for the benefit of future design and for the worst event of damper failure in flight time, out of spin plane dynamics have also been analyzed. The methods as outlined in the preceding paragraphs on spin plane dynamics are used. Table 2 summarizes the results of harmonic mode out of spin plane. Figure 2 shows the frequencies of various in plane and out of plane modes as functions of boom length.

For each mode excited at an initial time, the transient response of the system can be obtained by using Laplace transforms. The forced oscillation is

$$\mathcal{L}[D\theta] = [F(t) \theta(t)] \quad (7)$$

where D is a nonlinear time differential operator obtained from the Lagrangian, \mathcal{L} is the Laplace operator, $F(t)$ is the forcing function, and $\theta(t)$ is the step function

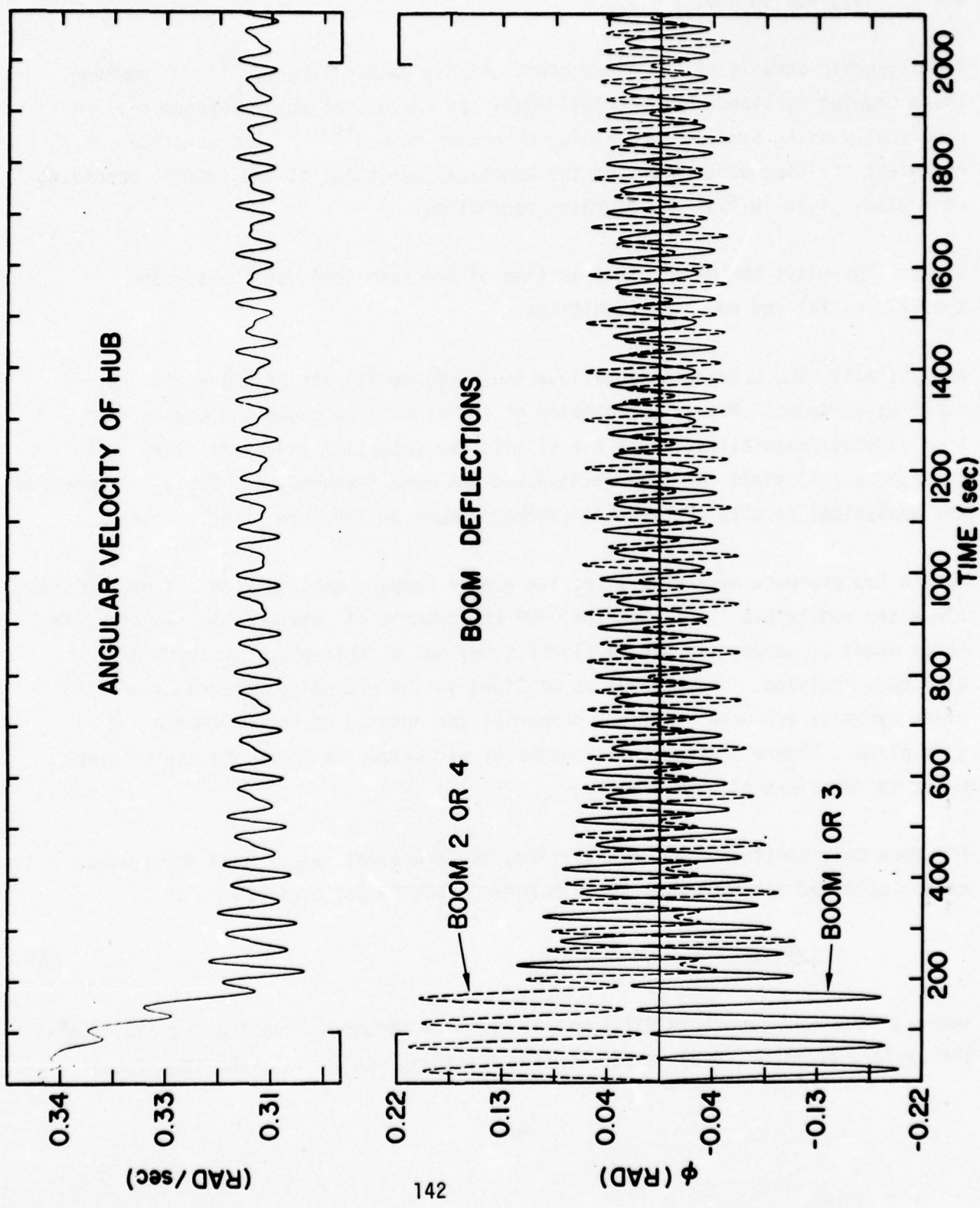


Figure 1. Simulation of Hub Angular Velocity and Boom Deflections Following a Disturbance Extension of booms (1,3) and simultaneous retraction of booms (2,4) by the same lengths.

Table 1. Normal Modes of Satellite with Pairwise Equal Length Wire Booms - Including Translational Oscillation of Hub

Classification of Mode	Shape of Mode (Characterized by the relative amplitudes of harmonic variables)						Harmonic Frequency	Limiting value of Harmonic Frequency: zero wire mass and spring constant
	a_1	a_2	a_3	a_4	a'	x'		
Partially Coupled Mode	μ_-	1	μ_-	1	v_+	0	$(p_1/a_1)^{1/2} / (1 + b_1 v_+ / a_1)^{1/2}$	$\omega_0 (r_0/r_1)^{1/2}$ for $r = r_1$
Uncoupled Mode with Translation	0	1	0	-1	0	4	$s_1 [(p_1/a_1) (1 + \frac{2q_1}{p_1}) / (1 - \frac{2(mr_1 + pr_1^2/2f)}{m(pr_1^2 + pr_1^3/3)})]^{1/2}$	$\omega_0 (r_0/r_1)^{1/2} [1 + \frac{m}{M} \frac{r + r_0}{r_0} + \dots]$ for $m(r_1 r_0) \ll M r_0$
Uncoupled Mode with Translation	-1	0	1	0	0	-8	$t [(p/a) (1 + \frac{2q_1}{p}) / (1 - \frac{2(mr + pr^2/2f)}{m(pr^2 + pr^3/3)})]^{1/2}$	$\omega_0 (r_0/r_1)^{1/2} [1 + \frac{m}{M} \frac{r + r_0}{r_0} + \dots]$ for $m(r + r_0) \ll M r_0$
Coupled Mode	μ_+	1	μ_+	1	v_+	0	$(p/a)^{1/2} / (1 + b_1 v_+ / a)^{1/2}$	$\omega_0 (r_0/r_1)^{1/2}$ for $r = r_1$
Pure Rotation Mode (Trivial)	0	0	0	0	0	1	0	0
Pure Translation Mode (Trivial)	0	0	0	0	0	0	0	0
Pure Translation Mode (Trivial)	0	0	0	0	0	0	0	0

Table 2. Normal Modes Out-of-spin-plane of Satellite with Four Equal Length Wire Booms - Including Translational Oscillation of Hub

Classification of Mode	Shape of Mode (Characterized by the relative amplitudes of harmonic variables)						Harmonic Frequency	Limiting value of Harmonic Frequency: zero wire mass and spring constant
	ψ_1	ψ_2	ψ_3	ψ_4	ψ_1	ψ_2		
Uncoupled Saddle Mode	-1	1	1	-1	0	0	$(q/a)^{1/2}$	$\omega_0 [(r + r_0)^2 / r]^1/2$
Coupled Mode	1	0	1	0	$-\frac{2\pi}{1}$	0	$(q/a)^{1/2} / (1 - 2\delta^2/r_0)^{1/2}$	$\omega_0 [(r + r_0)^2 / r]^1/2$
Coupled Mode	0	1	0	1	0	$-\frac{2\pi}{2}$	$(q/a)^{1/2} / (1 - 2\delta^2/r_0)^{1/2}$	$\omega_0 [(r + r_0)^2 / r]^1/2$
Jelly-Fish Mode	-1	-1	1	1	0	0	$(q/a)^{1/2} / (1 - \epsilon\delta^2 / a^2)^{1/2}$	$\omega_0 [(r + r_0)(1 + \epsilon\delta^2) / r]^1/2$
Pure Rotation Mode (Trivial)	0	0	0	0	1	0	0	0
Pure Rotation Mode (Trivial)	0	0	0	0	0	1	0	0
Pure Translation Mode (Trivial)	0	0	0	0	0	0	1	0

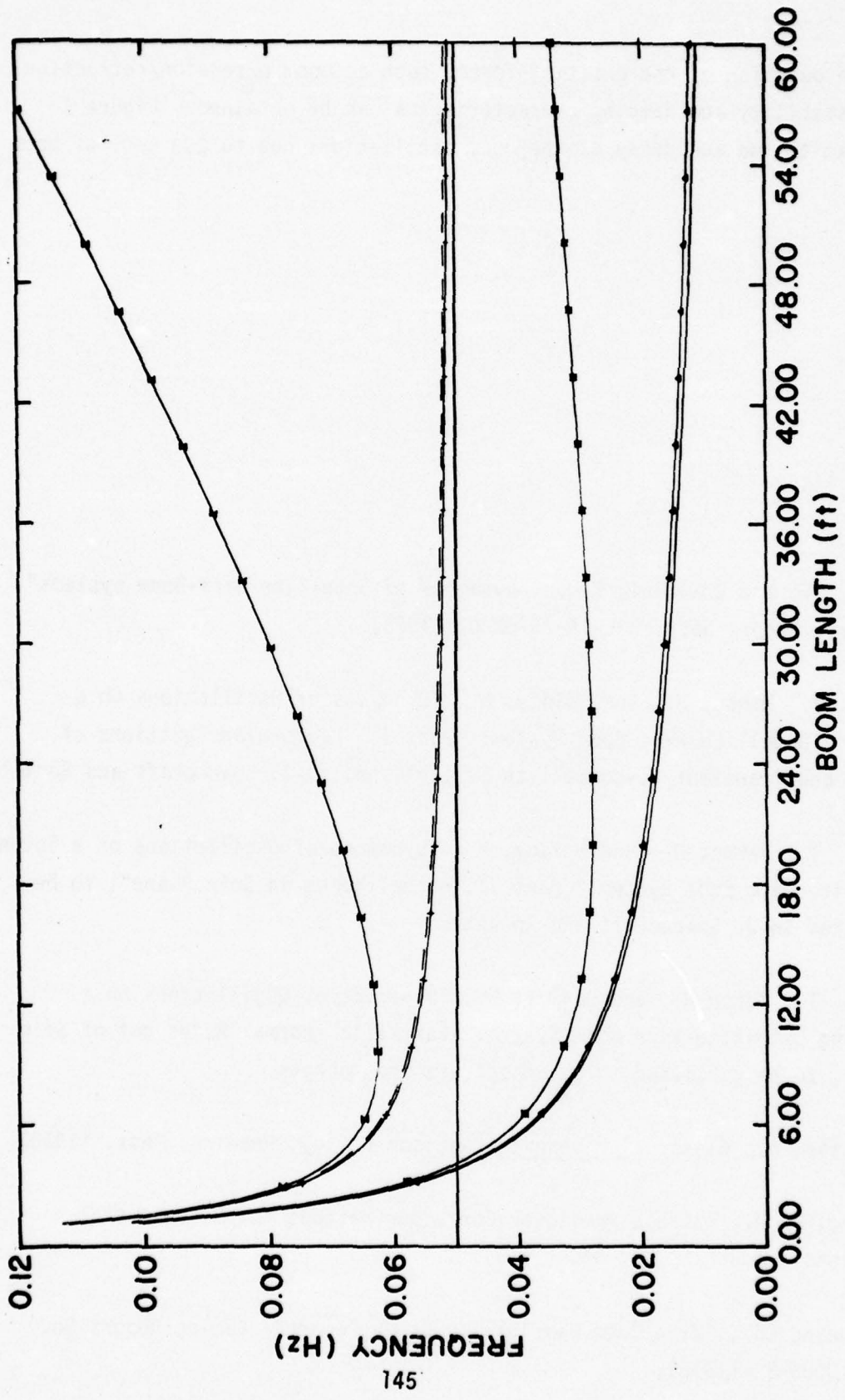


Figure 2. Nontrivial Harmonic Frequencies of Satellite System Spinning at 3 RPM
 The curves, in the order of descending frequency, represent out-of-plane coupled mode, out-of-plane jelly-fish mode, out-of-plane uncoupled saddle mode, inplane coupled mode, inplane uncoupled mode with translation, and inplane uncoupled mode, respectively. The horizontal line at 0.05 c.p.s. is the hub spin frequency.

AFCRL PHOTO

55-401

defining the duration of the exciting force, such as boom extension/retraction. Insight on stability and damping characteristics can be obtained. Figure 1 shows the excitation and decay of the boom oscillations due to 200 sec. of boom deployment.

References

- (1) Lai, S. T., and Bhavnani, K.H., "Dynamics of Satellite Wire-Boom Systems", Air Force Report No. AFCRL-TR-75-0220, (1975).
- (2) Lai, S. T., Mahon, H., and Smiddy, M., "Dynamics of Oscillations on a Spinning Satellite-Wire Boom System. Part I: Lagrangian Equations of Motion and Transient Response", to be published in J. Spacecraft and Rockets.
- (3) Lai, S. T., Mahon, H., and Smiddy, M., "Dynamics of Oscillations on a Spinning Satellite-Wire Boom System. Part II: Normal Modes in Spin Plane", to be published in J. Spacecraft and Rockets.
- (4) Lai, S. T., Mahon H., and Smiddy, M., "Dynamics of Oscillations on a Spinning Satellite-Wire Boom System. Part III: Normal Modes out of Spin Plane", to be published in J. Spacecraft and Rockets.
- (5) Goldstein, H., Classical Mechanics, Addison-Wesley, Reading, Mass. (1950).
- (6) Hamming, R. W., "Stable Predictor-Corrector Methods for Differential Equations", J.A.C.M., 6, 37, (1959).
- (7) The Boeing Co., "Wire Boom Feasibility Study Report", Boeing Report No. D233-10085-1, (1972).

Section 11. Ionospheric Field Mapping

11.0 Ionospheric Field Mapping

Initiator: M. Smiddy

Project No.: 8617

Problem No.: 4702

This work supports AFGL research projects on satellite sensing and mapping of the global distribution of electric fields in magnetospheric regions. Extensive analytical and computational procedures are required, and this work is still in process. Schematically, the scope of this work is outlined in the flow chart in Figure 1.

Data reduction considerations including handling of various instrumental and environmental factors are discussed below. Preliminary graphical presentations of the results are also included.

11.1 Data Reduction

For data reduction and computation, three types of input data are required. They are 1) electric field experiment data, 2) satellite sensor attitude (OM) data, and 3) ephemeris/magnetic field (ORMAG) data. The structures of these data are tabulated in the references^(1,2,3).

The electric field experiment data are in the fifth file of every tape of the satellite's raw data. The experiment data contain six channels of sensor signals with various high and low gains. These signals are given in telemetry counts, which can be converted to voltages by a simple conversion factor.

Calibration sequences show up every 512 sec to enable the updating of temperature correction coefficients, vehicle potentials, and plasma sheath impedance, and the checking of their statistical deviations for various channels.

11.2 Instrumental and Environmental Factors

Before the genuine electric field vectors along the trajectory of the satellite can be computed, various instrumental and environmental factors must be recognized, treated, and processed. Intermediate variables with physical significance are thereby developed and made available to the researchers.

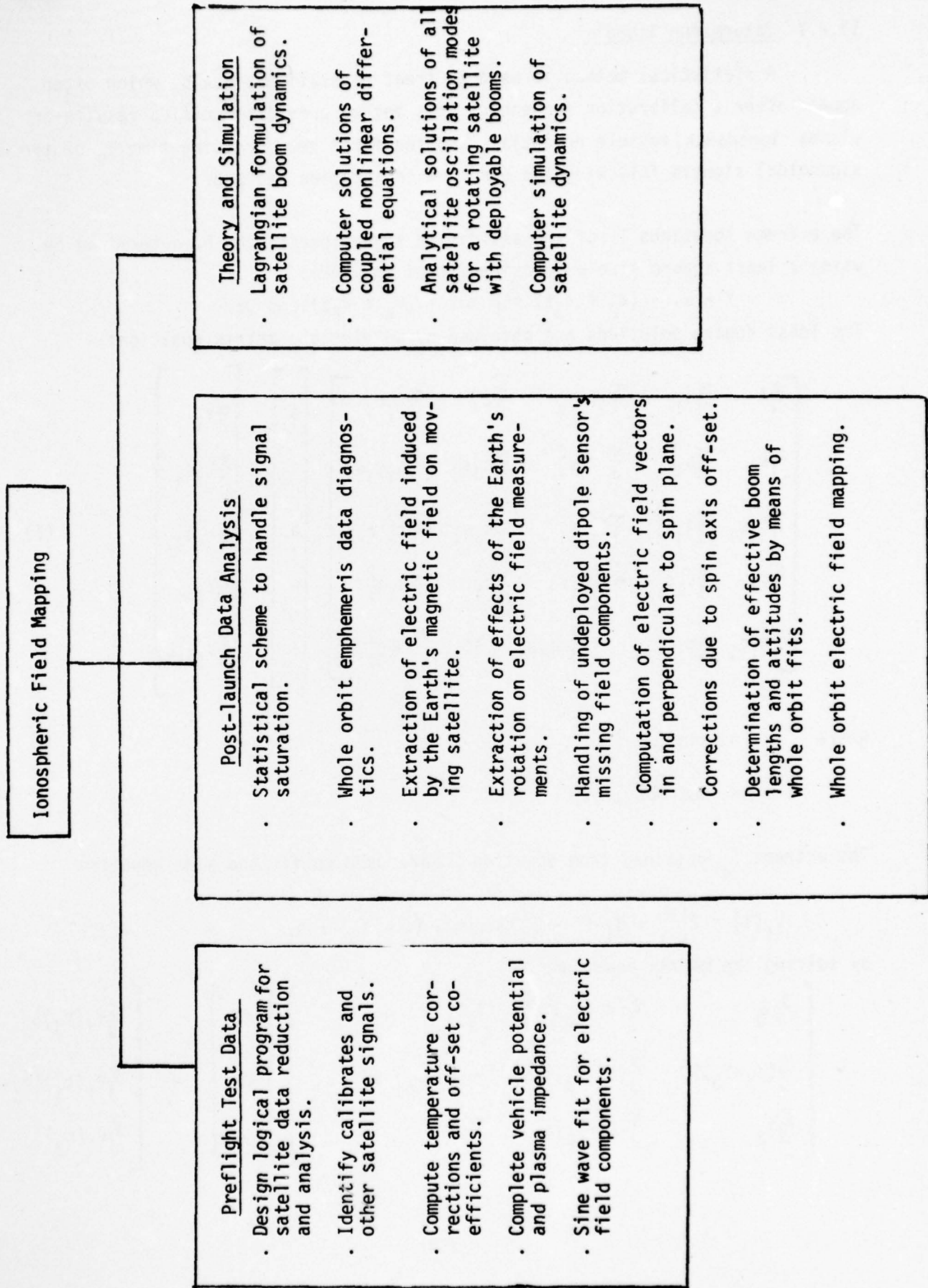


Figure 1. Task Outline for Ionospheric Field Mapping Project

11.2.1 Saturation Signals

A statistical method is used to treat saturation signals, which often appear after a calibration sequence. This method provides modified results on plasma impedance, vehicle potential, and the first zero crossing time T_0 of the sinusoidal signals following the end of a calibration sequence.

The extrema locations T_i of the saturation signal period can be determined by using a least square sine and cosine fit of the form:

$$Y = a_1 + (a_2 + a_3 t) \sin \omega t + (a_4 + a_5 t) \cos \omega t$$

The least square solutions are obtained by solving the matrix equation: -

$$\begin{bmatrix} \sum_i^1 & \sum_i s_i & \sum_i t_i s_i & \sum_i c_i & \sum_i t_i c_i \\ \sum_i s_i & \sum_i s_i^2 & \sum_i t_i s_i^2 & \sum_i c_i s_i & \sum_i t_i c_i s_i \\ \sum_i t_i s_i & \sum_i t_i s_i^2 & \sum_i t_i^2 s_i^2 & \sum_i c_i s_i t_i & \sum_i t_i^2 c_i s_i \\ \sum_i c_i & \sum_i c_i s_i & \sum_i t_i c_i s_i & \sum_i c_i^2 & \sum_i t_i c_i^2 \\ \sum_i t_i c_i & \sum_i t_i c_i s_i & \sum_i t_i^2 c_i s_i & \sum_i t_i c_i^2 & \sum_i t_i^2 c_i^2 \end{bmatrix} \begin{bmatrix} a_1 \\ a_2 \\ a_3 \\ a_4 \\ a_5 \end{bmatrix} = \begin{bmatrix} \sum_i Y_i \\ \sum_i Y_i s_i \\ \sum_i Y_i c_i \\ \sum_i Y_i c_i \\ \sum_i Y_i t_i c_i \end{bmatrix} \quad (1)$$

Where $s_i = \sin(\omega t_i)$

$c_i = \cos(\omega t_i)$

The extrema T_j obtained from equation (1) are used to fit the sine equation:

$$v_i(t) = 2[c_i + d_i(t - T_0)] \sin \omega(t - T_0) + e_i \quad (2)$$

by solving the matrix equation: -

$$\begin{bmatrix} \sum_j s_j & \sum_j (t_j - T_0) s_j^2 & \sum_j s_j \\ \sum_j (t_j - T_0) s_j^2 & \sum_j (t_j - T_0)^2 s_j^2 & \sum_j (t_j - T_0) s_j \\ \sum_j s_j & \sum_j (t_j - T_0) s_j & \sum_j 1 \end{bmatrix} \begin{bmatrix} 2c \\ 2d \\ e \end{bmatrix} = \begin{bmatrix} \sum_j v_i(t_j) s_j \\ \sum_j v_i(t_j)(t_j - T_0) s_j \\ \sum_j v_i(t_j) \end{bmatrix}$$

where $s_j = \sin [\omega(t_j - T_0)]$,

and T_0 is the time of the first zero crossing given by equation (2) with offset e_i removed, and is given by

$$T_0 = \left[\frac{1}{m} \sum_{k=1}^m T_k \right] - \frac{\pi}{2\omega} \left\{ \left[\frac{2}{m} \sum_{k=1}^m k \right]^{-K} \right\}$$

where $K=3$ if the T_1 corresponds to a minimum, and $K=1$ if T_1 corresponds to a maximum.

The plasma impedance $\langle R^i \rangle$ is calculated as

$$\langle R^i \rangle = \frac{1}{2} \left[\langle R_{k,1}^i \rangle + \langle R_{k,2}^i \rangle \right]$$

$$\text{where } R_{k,1}^i = 10^{10} \left(\frac{1 - c_{k,1}^i}{c_{k,1}^i} \right) \quad \text{and} \quad R_{k,2}^i = 10^6 \left(\frac{1 - c_{k,2}^i}{c_{k,2}^i} \right)$$

$$c_{k,1}^i = \frac{1}{24} \left[v_{k,1}^i - v_{k,2}^i - v_{k,3}^i + v_{k,4}^i - A_{k,1}^i + A_{k,2}^i + A_{k,3}^i - A_{k,4}^i \right] + 1 ,$$

$$c_{k,2}^i = \left[1 + \frac{1}{24} \left(v_{k,5}^i - v_{k,6}^i - v_{k,7}^i + v_{k,8}^i \right) \right] / \left[1 + \frac{1}{24c_{1,k}} \left(A_{k,5}^i - A_{k,6}^i - A_{k,7}^i + A_{k,8}^i \right) \right] .$$

$$A_{k,j}^i = \left[c^i + d^i(t_k - T_0) \right] \sin \omega(t_k - T_0), \quad i=1,4$$

$$A_{k,j}^i = \left[c^i + d^i(t_k - T_0) \right], \quad i=3,6$$

and j corresponds to the j th interval of a calibration sequence. Similarly, the vehicle potential $\langle \phi^i \rangle$ is given by

$$\langle \phi^i \rangle = \frac{1}{2} \left[\langle \phi_{k,1}^i \rangle + \langle \phi_{k,2}^i \rangle \right]$$

$$\text{where } \phi_{k,1}^i = \frac{1}{4} \left\{ v_{k,1}^i - v_{k,2}^i + v_{k,3}^i - v_{k,4}^i - A_{k,1}^i + A_{k,2}^i - A_{k,3}^i + A_{k,4}^i \right\}$$

$$\theta_{k,2}^i = \frac{1}{2} \left\{ (v_{k,5}^i - v_{k,6}^i + v_{k,7}^i - v_{k,8}^i) - \frac{c_{2,k}}{c_{1,k}} (a_{k,5}^i - a_{k,6}^i + a_{k,7}^i - a_{k,8}^i) \right\}$$

The statistical deviations of these quantities are also calculated.

11.2.2 Effect of Earth's Rotation

The electric field induced in the dipole sensors of a satellite is of sine wave form because of the spin of the satellite. In the regions of low latitude (equatorial) and low altitude, it is well known that electric field is small due to lack of significant plasma motion, so that the predominant electric field is due to the Earth's rotation. The two laws invoked in this case are:

1. The electric field \underline{E} measured in a moving frame is related to the electric field \underline{E}_0 in a rest frame by ⁽⁴⁾

$$\underline{E} = \underline{E}_0 + \underline{V} \times \underline{B} \quad (3)$$

where \underline{B} is magnetic field in the rest frame, and velocity \underline{V} is assumed small ($V \ll C$) otherwise there is an additional relativistic factor in the denominator.

2. The velocity \underline{V}_r in a rotating frame r is related to the velocity \underline{V} in a fixed frame by ⁽⁵⁾

$$\underline{V}_r = \underline{V} - \underline{\omega} \times \underline{r} \quad (4)$$

where $\underline{\omega}$ is the rotation angular velocity and \underline{r} is the position vector.

Thus, the induced electric field due to the Earth's rotation is

$$\underline{E} = \underline{V}_r \times \underline{B} \quad (5)$$

where \underline{V}_r is given by eq.(4).

This induced field \underline{E} is always subtracted out in order to bring out the genuine electric field from the processed result.

11.2.3 The Case of the Missing Dipole

Satellite signals show that one pair of dipole sensors on the satellite S3-2 is not functioning properly. This poses a problem on the determination of three dimensional electric field vector because one component is always missing. However, since the satellite is spinning, a method can be worked out to overcome this problem. When the electric field is maximum in the xy-plane defined by two dipole pairs \underline{r}_1 and \underline{r}_2 on a spinning satellite, it is reasonable to assume that the electric field in the z-direction is zero.

However, r_1 and r_2 need not be orthogonal at flight time, causing the vector algebra manipulation to be nontrivial. The result is

$$\underline{E} = E_1 \hat{x} + \frac{\{E_2 - (\hat{r}_1 \cdot \hat{r}_2) E_1\} \hat{y}}{|\hat{r}_1 \times \hat{r}_2|} + 0 \hat{z}$$

where $\hat{\cdot}$ denotes the unit vector.

This gives the electric field vector, inspite of the missing dipole.

11.2.4 Effective Frequency and Boom Lengths

The information on the frequency ω of the spin of a satellite is given by Boeing's OM data tape. The electric field measured by the satellite dipole sensors is predominantly ($V \times B$) where the velocity V has to be corrected for the effects of Earth's rotation. The value of frequency ω from OM data often turns out to be slightly different from the electric field variation. Hence, a curve fitting is carried out in case one needs very accurate indication of ω .

Furthermore, the amplitude of the induced electric field in a dipole depends on the attitude and boom length of the dipole. However, the information on these items as given by the satellite signal data tape may not be perfectly accurate, due to the possibility that the booms of a dipole may not be colinear and that the spin axis tilts and precesses. These uncertainties of satellite information have to be treated by curve fitting.

For orbit #52, an analytical computation has been performed assuming that the non-colinear booms of a dipole are simply perpendicular to the instantaneous spin axis, with offset angles as supplied by Aerospace Inc. The effective boom lengths and attitude agree quite well with the least square curve fitting of the function $R_o(V \times B)$ against satellite data.

11.2.5 DC Offsets

Analysis of the data of satellite S3-2 shows considerable DC offsets in the electric field data. This phenomenon has never been noticed before because no experiment using such a high sensitivity instrument had been performed previously. Further analysis shows that there exist correlations between DC offsets, electron density and oxygen ion population in the satellite environment. Since the ambient electric

field is mainly associated with drifting plasma⁽⁶⁾ in the polar and auroral regions, the DC offset is fitted in the equatorial region by means of a high order polynomical (e.g. 13th) order, which is then subtracted from the computed E-field results which has induced field $(V - \mathbf{w} \times \mathbf{r}) \times \mathbf{B}$ already removed.

11.3 Graphical Presentations

11.3.1 E-Field Strip Chart

Figure 2 shows the computed ambient electric field during an orbit. A number of estimates are made during each satellite spin, resulting in the bar pattern. The total and components in ECI, geomagnetic (GM), and solar magnetic (SM) coordinates are plotted together with environmental information.

11.3.2 E-Field and Drift Current Polar Maps

A typical mapping plot of electric field vectors in the polar region is shown in Fig. 3, and the corresponding $(\mathbf{E} \times \mathbf{B})/B^2$ drift current pattern is shown in Fig. 4.

11.3.3 Combination Strip Chart

It is quite often useful, when analyzing data, to have a graphic presentation of other physically related parameters. In the E-field experiment, parameters such as the ambient plasma density, the heavy-ion density, and the high-energy (1-5 kev) particle flux are of particular interest, since each can affect the measurement in its own particular way. Another parameter, the orientation of the measuring antenna w.r.t. the ambient magnetic field, is useful in determining whether or not a particular anomaly is due to particle streaming along the field lines. A program, BILD3, has been developed to merge and present all parameters and data of interest.

Functional Description

The plasma and ion densities and particle flux can be obtained from on-board experiments. The antenna-field orientation, however, must be derived from model-field calculations and satellite attitude data. BILD3 accesses the pertinent data, ephemeris, and altitude files, unpacks the data, performs the necessary conversions and tranformations, plots on one graph the above-mentioned parameters together with

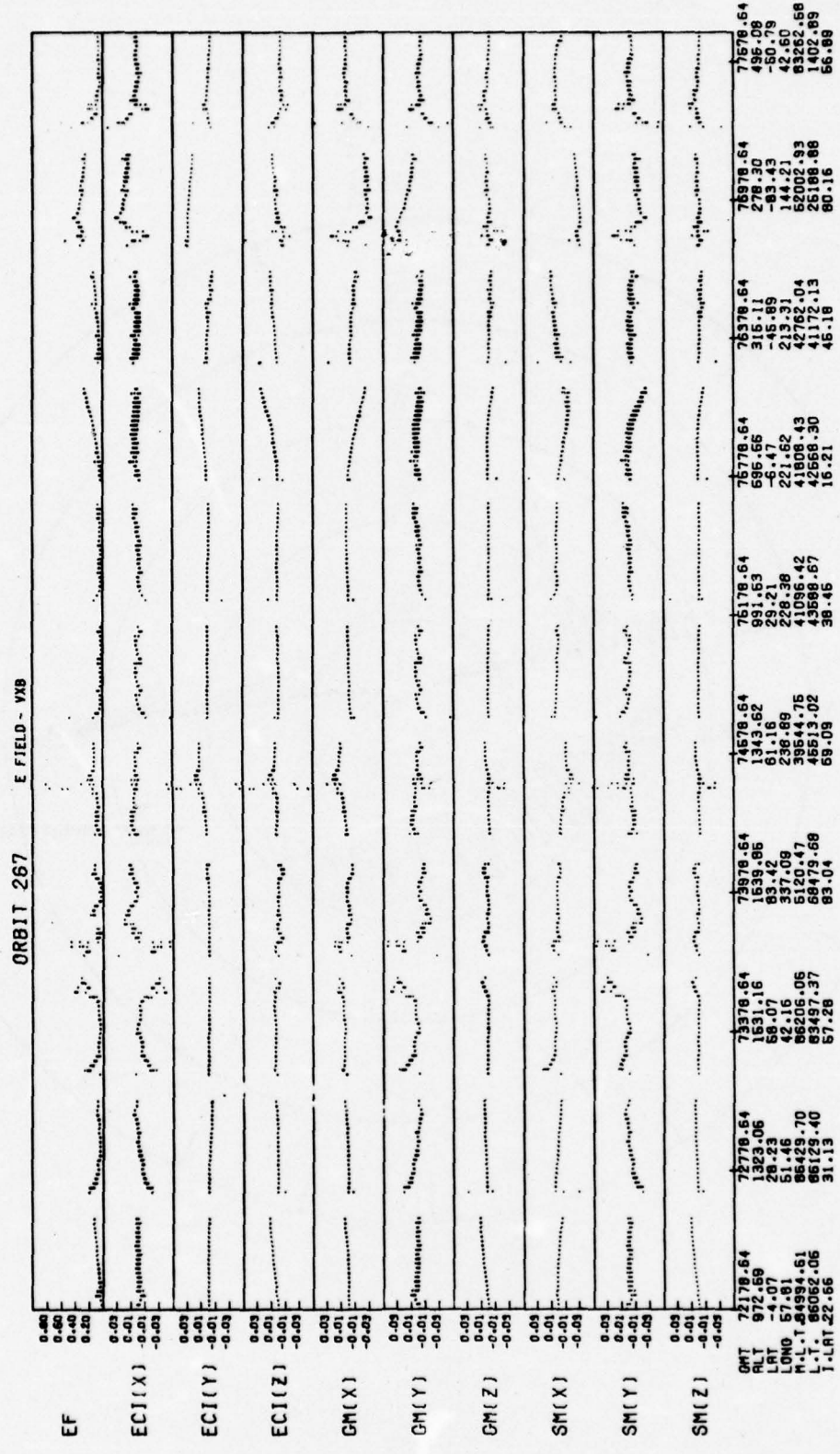


Figure 2. Computed Ambient Electric Field During an Orbit

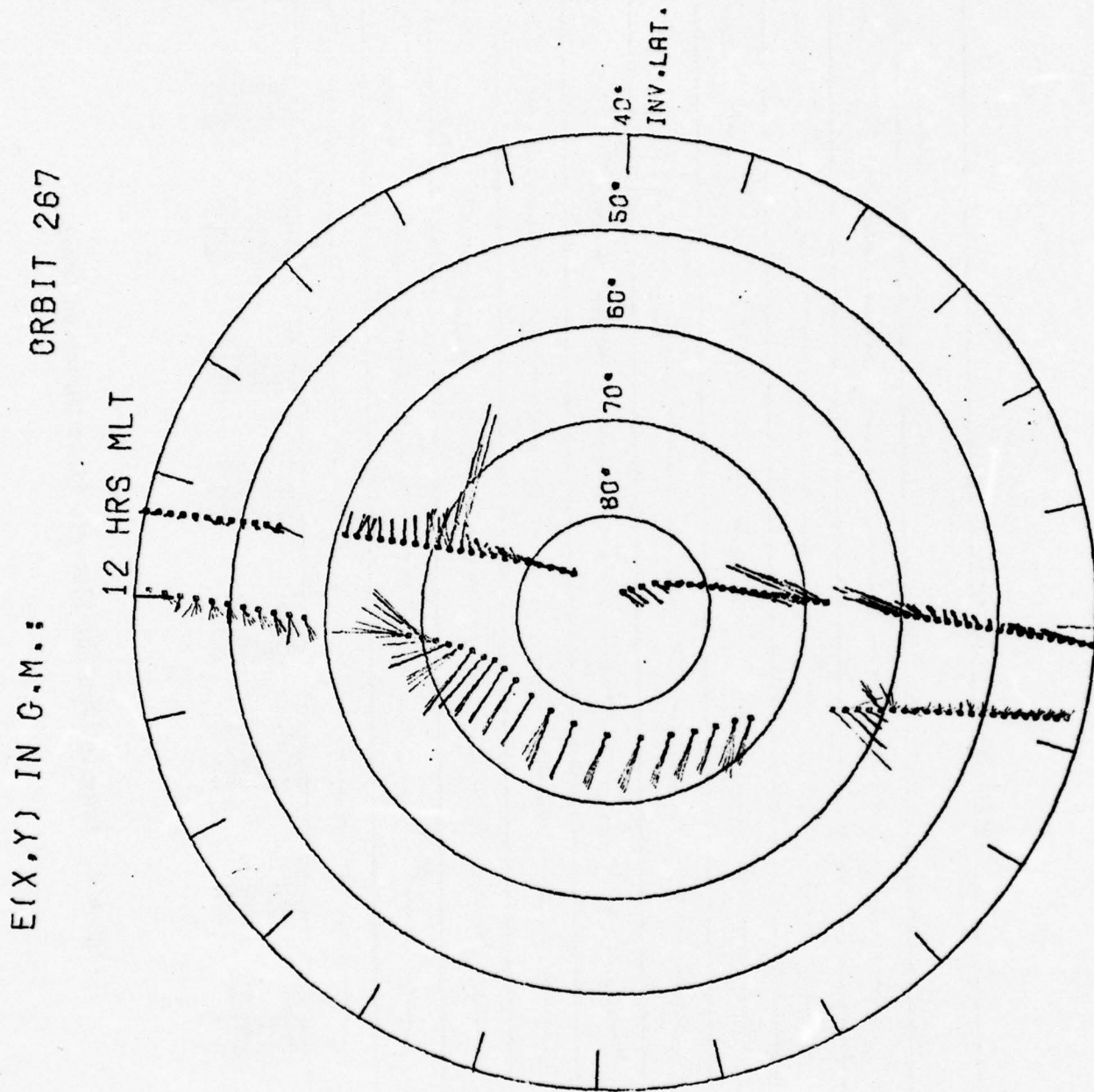
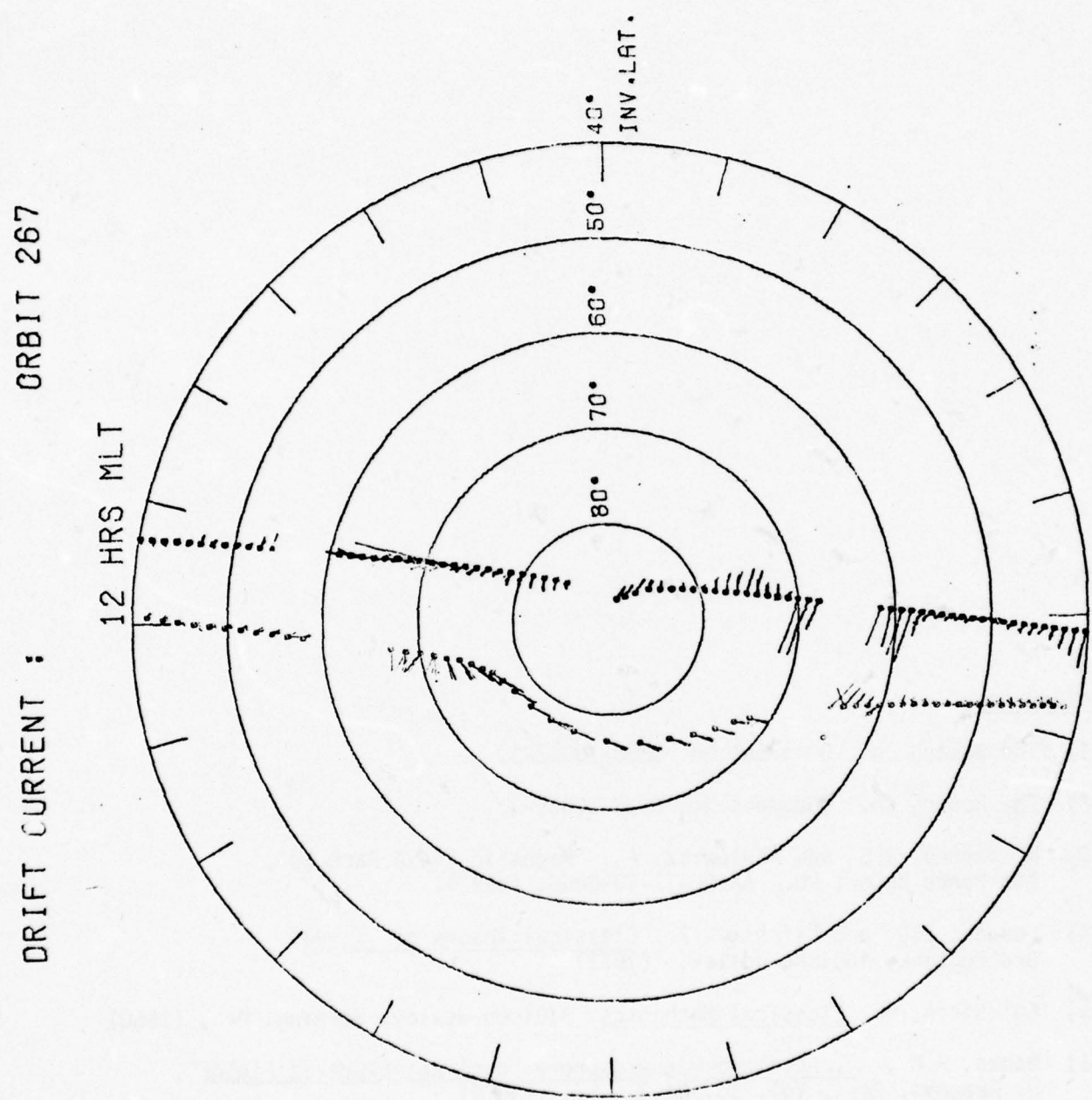


Figure 3. Polar Plot of Electric Field Vectors During an Orbit
Plot on the left is for the Southern Hemisphere.

Figure 4. Polar Plot of Computed Drift Current During an Orbit



E-field data, and labels the X-axis with geophysical coordinates such as universal time, altitude, local time, and invariant latitude. Although short stretches of time can be plotted, as in Figure 5, the program is more often used for entire orbits, producing graphs six to eight feet long.

References

- (1) The Boeing Co., Document No. D233-10002-1.
- (2) The Boeing Co., Document No. D233-10036-2.
- (3) McInerney, R.E. and Abelowitz, A., "Magnetic Field Package", Air Force Report No. AFCRL-TR-73-0356, (1973).
- (4) Landau, L.D. and Lifshitz, I., Classical Theory of Fields, 3rd Edition, Addison-Wesley, (1973).
- (5) Goldstein, H., Classical Mechanics, Addison-Wesley, Reading, Ma., (1950).
- (6) Banks, P.M., "Ionosphere-Magnetosphere Coupling: Electric Fields", J. Geophys. Res., Vol. 13, No.3, 874 (1975).

ORBIT NO. 1997 DATE 04/25/76

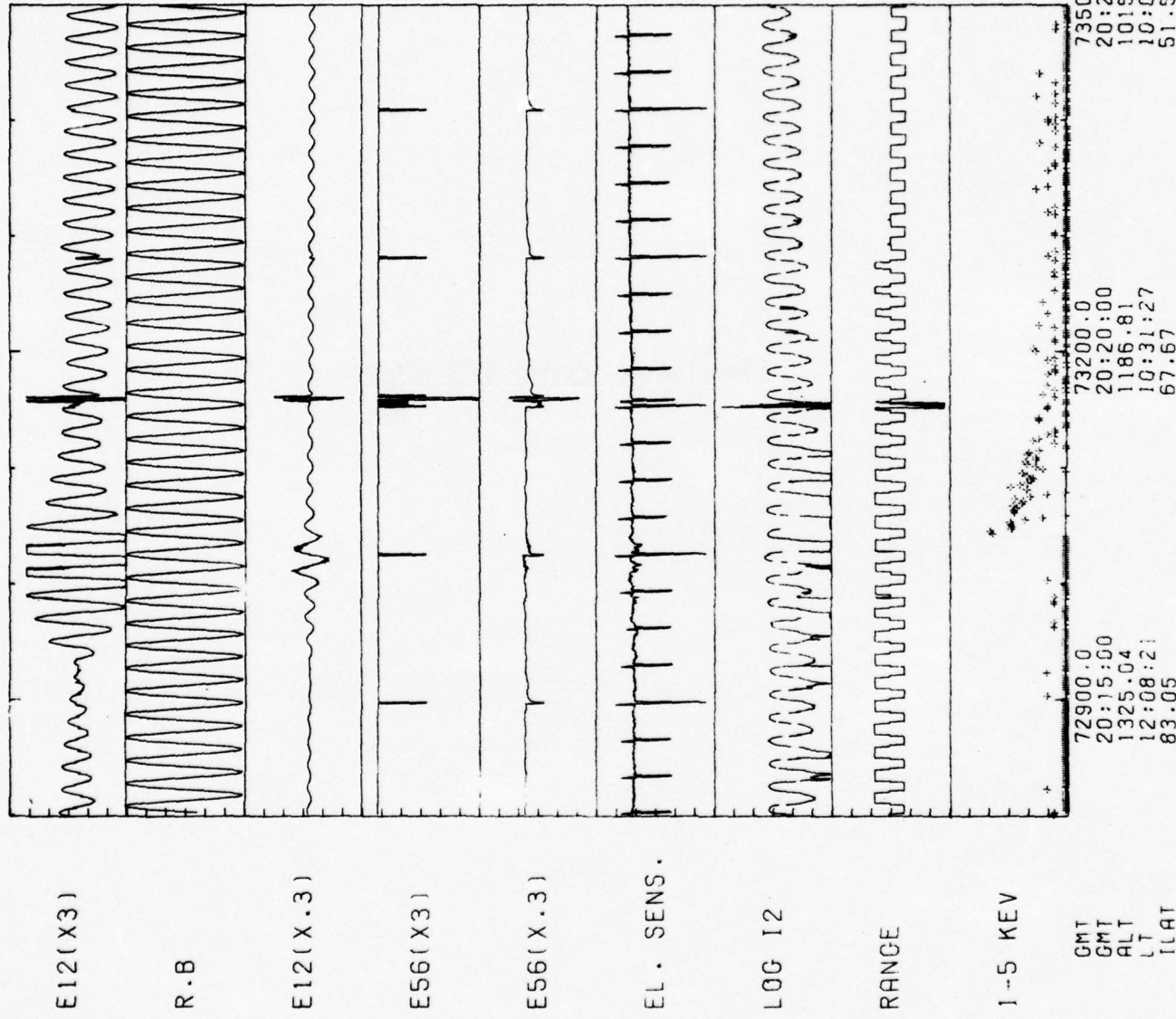


Figure 5. Combination Plot of Measurements from the E-Field, Plasma Motion, and High-Energy Particle Flux Experiments

Section 12. Plasma Bulk Motion

12.0 Plasma Bulk Motion

Initiator: P. Wildman

Project No.: 8617

Problem No.: 4701

Disturbances and irregularities in the ionosphere and magnetosphere, particularly in the polar and auroral regions affect electromagnetic wave communications, detection, tracking, guidance, and early-warning defense systems. Ambient plasma bulk motion is an important factor in forecasting ionospheric and magnetospheric plasma meteorology and in understanding the processes leading to polar region irregularities. This work supports research projects at AFGL on *in situ* satellite sensing of plasma bulk motion. Schematically, the tasks performed for this problem are outlined in Figure 1.

12.1 Data Processing

For data processing, three data tapes are required, viz., the plasma experiment data tape, the satellite attitude (OM) data tape, and the satellite ephemeris (ORMAG) data tape. The structures of these data are explained in the references.^(1,2)

The satellite signals consist of several patterns which have to be recognized. They are the TM applied voltage sweeps, electron sensor real sweeps, electron calibrates, ion calibrates, and range switchings. The TM sweeps are doubly filtered to remove any noisy data that may be present. The processed data are used in the computations of electron and ion properties in the ionosphere and magnetosphere. The flow chart of Figure 2 and the supplemental notes present the data processing and computation logic.

12.2 Electron Properties of Plasma

A TM applied voltage sweep appears once every 128 sec. in the experiment. This voltage is also applied to every real sweep of the electron sensor in the following 128 sec. period. The voltage-current response characteristics of the sensor output gives information on the electron properties of the plasma environment. Physically, the electron sensor current I is proportional to the velocity, thermal distribution, and density of the electrons, i.e.,

$$I \propto N_e A \sqrt{\frac{2 k T}{m}} \exp\left(-\frac{eV}{kT}\right)$$

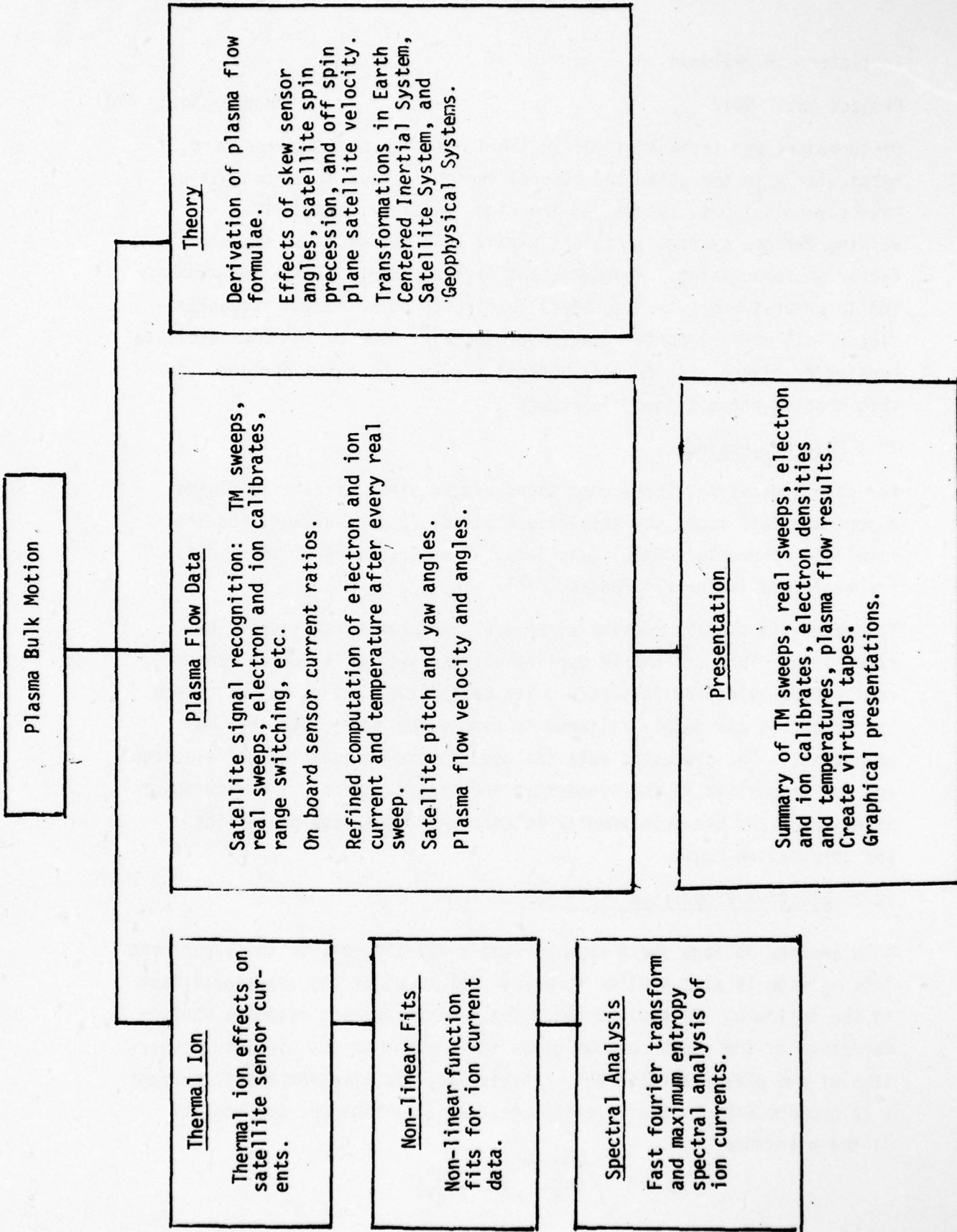


Figure 1. Task Outline for Plasma Bulk Motion Project

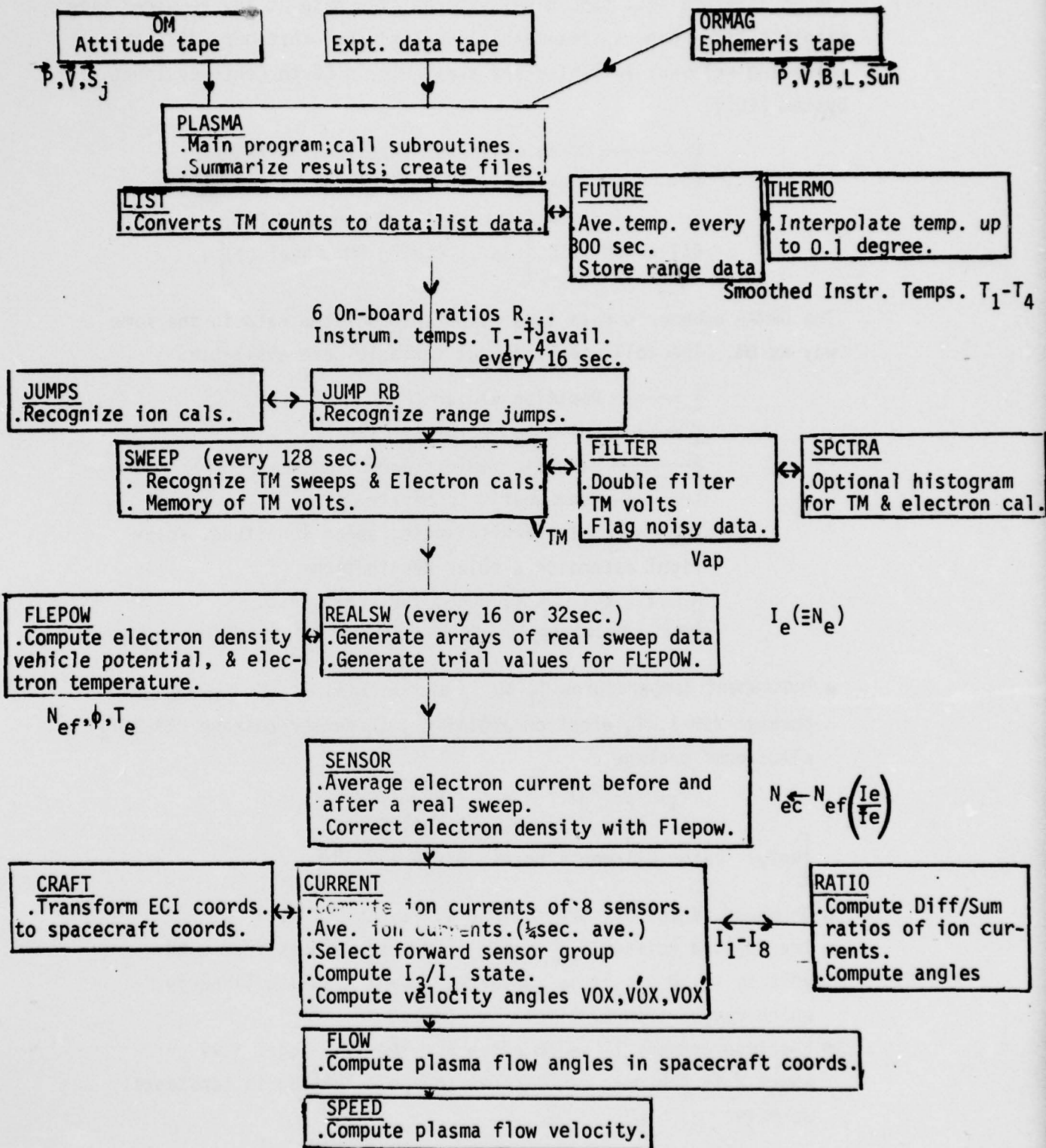


Figure 2. Data Processing and Computation Flow Chart for Plasma Flow Parameters

Supplement to the "Plasma Flow" Flow Chart

The OM attitude data tape gives interpolated data at any required time within a time span (approximately equal to the orbit period). The following relevant variables are available in Earth Centered Inertial System (ECI).

P—— Position vector (Nautical Miles)
V—— Velocity vector (Nautical Miles/Sec.)
S—— Direction cosines of sensor L.O.S. in
ECI coord. etc. [Ref.: Boeing OM Manual (1)].

The ORMAG ephemeris data tape gives interpolated data in the same way as OM. The following relevant variables are available.

P—— Position vector (km)
V—— Velocity vector (km/sec)
B—— Magnetic field (Gamma)
L—— Geomagnetic Coordinate L.
Sun—— Solar zenith angle, solar longitude, solar right ascension & solar declination.
M.L.T., L.T., LAT, LONG, INV. LAT., etc.
[Ref.: McInerney's AFCRL report (2)].

- Instrument temperatures T_1 to T_4 are defined as: T_1 for sensor package 219-1, T_2 electron amplifier, T_3 sensor package 219-2, T_4 electronic package

$$(T_1, T_2, T_3) = (V_T - 1.680)/0.0448$$

$$T_4 = (V_T - 2.190)/0.0404$$

[Ref.: Peter Wildman's notes, March 1975 (6)]

- On board ratios R_{ij} are defined as $(I_i - I_j)/(I_i + I_j)$
- The applied voltage V_{ap} during a TM sweep ranges from 8.00 volt to -8.50 v.; it is converted from its analog linearly, which ranges from 5.10 volt to -0.10v.
- Electron current I_e is obtained as $\log I_e = \log V + kV$ where V is the data of electron sensor. Putting in constants, we have

$$I_e = \exp \left\{ -23.8020759 + 0.0041976 T_2 + [2.4691428 + -.0017304 T_2] . V \right\}$$

Supplement to the "Plasma Flow" Chart (Continued)

Electron density N_e is given by

$$N_e = 4.3535 \times 10^{11} I_e / T_e^{1/2} f(v)$$

where $f(v)$ is chosen as 1.00, T_e as 2500.

- Flepow gives corrected electron density N_{ef} , vehicle potential, and electron temperature T_e after every real sweep. If the electron sensor is partially saturated, Flepow rejects the sweep.

- \bar{I}_e is average electron current before and after a real sweep.

(15.25 15.78)sec., (18.75 19.25) sec., if Hi rate;

(31.25 31.75)sec. (34.75 35.26) sec., if Lo rate.

[Ref.: Wildman notes, Sept. 1975⁽⁶⁾]

- Corrected electron density $N_{ec} = N_{ef} \frac{I_e}{\bar{I}_e}$

- Ion currents I_1 to I_8 are given by

$$I_i = [K_i V + C] \times 10^{-M}$$

where K_i is temperature dependent function, tabulated in Wildman's notes, July 1975; V is ion sensor data, C is chosen as -0.1, and M is a range dependent number.

- Time average of ion current is optional, from 1/16 sec. to 1 sec.; currently $\frac{1}{4}$ sec. average is used.

- Other items in the last boxes of the flow chart are less basic.

Details of these items are referred to Wildman's write up on April, 1976.⁽⁶⁾

where the square root term is due to the electron velocity, the exponential term is the Boltzmann distribution function, N is electron density, e is charge, and A is sensor aperture area. Therefore, the slope of $\log_e(I)$ plotted versus voltage $V(t)$ should yield the electron temperature T , and once T is found, N can be computed. However, in reality it turns out that the current response of the instrument is highly sensitive only in a very short time span near the middle of the sweep period. Thus, a slope measurement becomes non-trivial. In order to perform highly accurate computation, a subroutine FLEPOW is used, employing the steepest gradient minimization technique of Fletcher and Powell⁽³⁾. It yields results on electron density, electron temperature, vehicle potential, and plasma sheath radius, for every sweep. Calculated electron properties for a typical polar orbit are shown in Figure 3.

12.3 Ion Properties and Flow

Eight sensors, divided into two groups, provide measurement data of ion currents. It is the forward looking group which gives more accurate information. Since the satellite is always spinning the two sensor groups alternate in facing forward. Thus, sensor attitudes and velocity vectors are computed at all times to determine which sensor group to be processed at every moment. For diagnostic purpose ground computation of ion sensor current ratios are compared with on board ratios. To measure bulk ion plasma flow, there are approximately two regimes, viz, the relatively fast ion regime and the relatively slow ion regime. The former refers to the light ion mass regions such as those occupied predominantly by hydrogen, and the latter refers to high oxygen concentration regions.

In the light ion, fast flow regime, a mathematical formulation has been worked out for the determination of the pitch P_F , yaw Y_F and magnitude f of plasma flow. Details are reported in reference⁽⁴⁾. The results are as follows:

$$\tan(E_t + P_F) = \frac{V \cos \sigma_t \sin E_t - q \cos Y_Q \sin (E_t + P_Q)}{V \cos \sigma_t \cos E_t - q \cos Y_Q \cos (E_t + P_Q)} \quad (1)$$

$$\tan Y_F = \frac{V \sin \sigma_t - q \sin Y_Q}{\left[V^2 \cos^2 \sigma_t + q^2 \cos^2 Y_Q - 2Vq \cos \sigma_t \cos P_Q \cos Y_Q \right]^{\frac{1}{2}}} \quad (2)$$

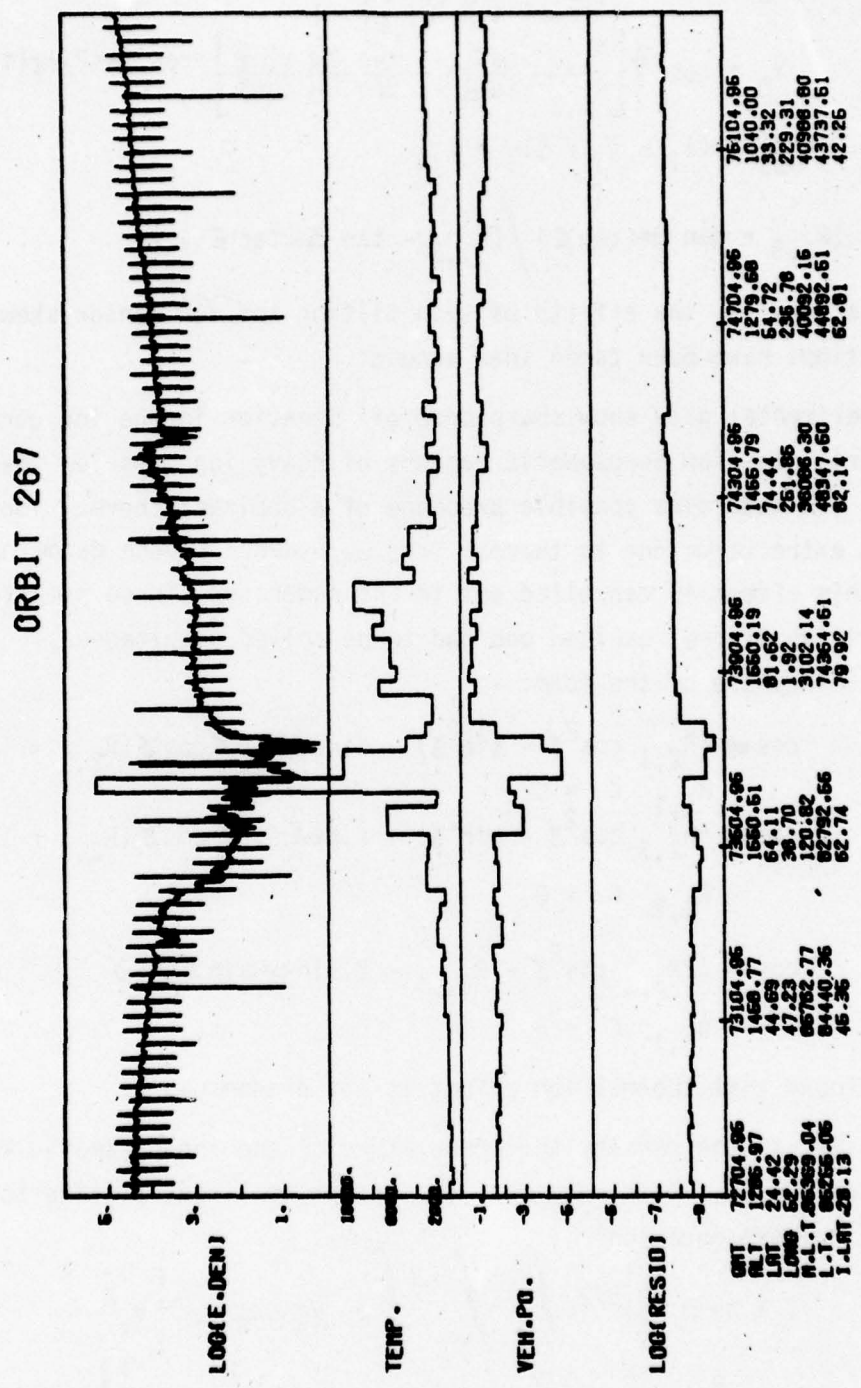


Figure 3. Plot of Parameters Computed from Electron Sensor Experiment

$$f^2 = q^2 + v^2 - 2q v (\cos \sigma_t \cos \gamma_Q \cos p_Q + \sin \sigma_t \sin \gamma_Q) \quad (3)$$

where

$$p_Q = \tan^{-1} \left\{ \frac{R_{2,4}}{\tan \alpha} \left[\frac{1-\chi}{1+\chi R_{2,4}} \right] \right\} - \epsilon(t)$$

$$\gamma_Q = \tan^{-1} \left\{ \left[\frac{R_{1,3} \cos \epsilon}{R_{1,3} \sin \epsilon} + \frac{\tan 2\alpha \sin \epsilon}{\tan 2\alpha \cos \epsilon} \right] \cos (\alpha + p_Q + \epsilon(t)) \right\}$$

$$R_{i,j} = (I_i - I_j) / (I_i + I_j)$$

$$\text{and } \chi = (R_{1,3} + \tan 2\alpha \tan \epsilon) / (R_{1,3} - \tan 2\alpha \tan \epsilon).$$

In these results, the effects of spin tilting and ion sensor skew orientations have been taken into account.

The experimental data show sharp drop off behavior in the ion current time variations for ionospheric regions of heavy ion mass low speed plasma. To determine possible presence of a dominant thermal ion effect, extra terms due to thermal ions were added to the denominator of $R_{i,j}$ while this effect is cancelled out in the numerator. Three simultaneous trigonometric equations resulted and had to be solved simultaneously at every second. They are of the form: -

$$\begin{aligned} & \cos \alpha (R_{2,1} \cos^2 \gamma - \sin^2 \gamma) - \sin \alpha \sin \gamma \cos \gamma (R_{2,1} + 1) \\ & + R_{2,1} C = 0 \\ & \cos \alpha (R_{2,3} \cos^2 \gamma - \sin^2 \gamma) + \sin \alpha \sin \gamma \cos \gamma (R_{2,3} + 1) \\ & + R_{2,3} C = 0 \end{aligned}$$

$$\begin{aligned} & \cos \alpha (2R_{3,1} \cos^2 \gamma - R_{3,1}) - 2 \sin \alpha \sin \gamma \cos \gamma \\ & + R_{3,1} C = 0 \end{aligned}$$

It was found that thermal ion effect is not predominant.

To investigate the density and temperature of the ion plasma in the low speed regime, it is necessary to perform nonlinear fitting to the ion current equation⁽⁵⁾:

$$I = N e A \left(\frac{a}{\pi} \right)^{3/2} \int_{V_x} \int_{V_y} \int_{V_z} v_z \exp \left\{ -a \left[v_x^2 + v_y^2 + v_z^2 + q^2 - 2q (v_z \cos \theta + v_y \sin \theta) \right] \right\} dv_x dv_y dv_z \quad (4)$$

Integrating, we have

$$I = \frac{1}{2} Ne A q \cos \theta \left[1 + \operatorname{erf}(x) + \exp(-x^2)/x\pi^{\frac{1}{2}} \right]$$

where $x = q a^{\frac{1}{2}} \cos \theta = (2q/c\pi^{\frac{1}{2}}) \cos \theta$

and $\operatorname{erf}(x)$ is the error function defined as

$$\operatorname{erf}(x) = \left(\frac{2}{\pi^{\frac{1}{2}}} \right) \int_0^x \exp(-t^2) dt$$

Here, q is the plasma flow velocity which, in low altitude and equatorial regions, is mainly due to the relative motion of the satellite in the plasma environment; $\cos \theta$ is the angle between flow direction and sensor normal.

The parameters to be fitted are $\alpha (=Ne A)$ and $\beta (= a^{\frac{1}{2}})$. The former (α) measures the ion density and effective sensor aperture area and is responsible for the height of the ion current variations. The latter(β) is also $\sqrt{\frac{m}{2kT}}$ which measures the plasma velocity, or ion mass to ion temperature ratio. β influences the profile of the ion current curves. A typical nonlinear fitting of ion current for a satellite spin is shown in Figure 4.

References

- (1) The Boeing Co., Document No. D233-10002-1.
- (2) McInerney, R.E. and Abelowitz, A. "Magnetic Field Package, " Air Force Report No. AFCRL-TR-73-0356, (1973).

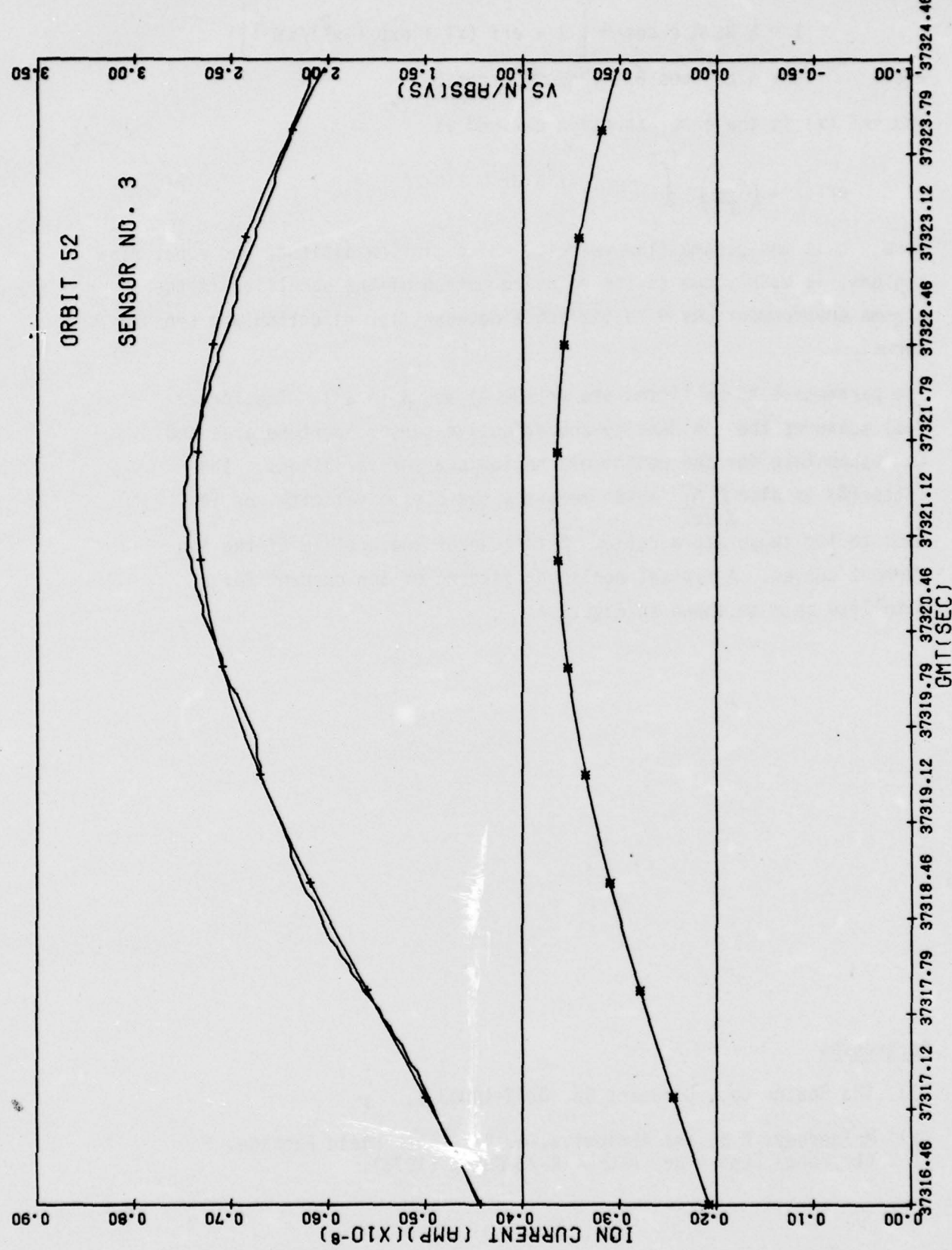


Figure 4. Plot of Measured and Modeled Ion Current During 1/2 Satellite Rotation
The component of the Vehicle Velocity in the direction of the Sensor Normal is
also plotted.

- (3) Fletcher, R. and Powell, M.J.D., "Rapidly Convergent Descent Method for Minimization", The Computer Journal, Vol. 6, p.163.
- (4) Lai, S.T., Smiddy, M., and Wildman, P., "Satellite Sensing of Low Energy Plasma Bulk Motion", accepted for presentation at the AMS/AIAA Symposium on Satellite Remote Sensing, Florida, Nov. 1976; to appear in the Proceedings of the Symposium on Satellite Remote Sensing.
- (5) Sagalyn, R.C. and Smiddy, M., "Positive Ion Measurements of Spacecraft Attitude: Gemini X and XII", J. Spacecraft and Rockets, Vol. 6, No. 9, (1969).
- (6) Wildman, P., Working Papers for "Plasma Bulk Motion".

Section 13. DMSP Topside Plasma Monitor (Phase I)

13.0 DMSP Topside Plasma Monitor (Phase I)

Initiator: R. Sagalyn

Project No.: 8617

Problem No.: 4836

The Topside Plasma Monitor to be flown on Defense Meteorological Systems Project (DMSP) satellites consists of two sensing systems; one, the electron sensor, measures ambient electron density, electron temperature and vehicle potential and the other system, the ion sensor, measures the ambient density of each ion specie, the average ion temperature and the vehicle potential. The observed parameters, measured as a function of time along the vehicle trajectory, are to be combined with ephemeris data to give plasma scale height and $f_0 F_2$ as a function of position and density irregularity frequency spectra. This Supplementary Sensor Ion-Electron (SSIE) system is to be used in cooperation with Global Weather Center, Offutt AFB.

This report outlines procedures planned as a result of analyses to date, both for the data processing system and for determination of electron and ion parameters. Preliminary studies

with sample data are anticipated to evaluate the one and two specie analysis procedures for H^+ , He^+ and O^+ . Stability of the solution technique using a restricted number of sweep data points is essential to providing a reliable on-line analysis package for determining specie densities, temperatures, vehicle potential, and eventually the plasma scale height and $f_0 F_2$.

13.1 Data Processing System

The data processing system, electron and ion mass and temperature analyses, and the file structures are defined for operation in a real time environment on a UNIVAC 1110 computer at Offutt AFB. Initial development and follow-on global mapping work is to be conducted on the CDC 6600 system at AFGL. Compatibility of the program between the two systems will be maintained by processing 36 bits of data from the UNIVAC 1110 in one 60 bit word on the 6600. Requisite conversion of floating point numbers will account for the shorter characteristic and mantissa, and the sign plus magnitude arithmetic of the 1110.⁽¹⁾ Other special conversion considerations include the use of IOWAIT and FLD instructions with GWCIØ, instead of WRITMS, READMS and the character and bit-processing instructions (MXGETX, LBYTX, etc.) with the 6600 SCOPE-Fortran System.

Data processing will consist of read out of multiples of 28-word sectors

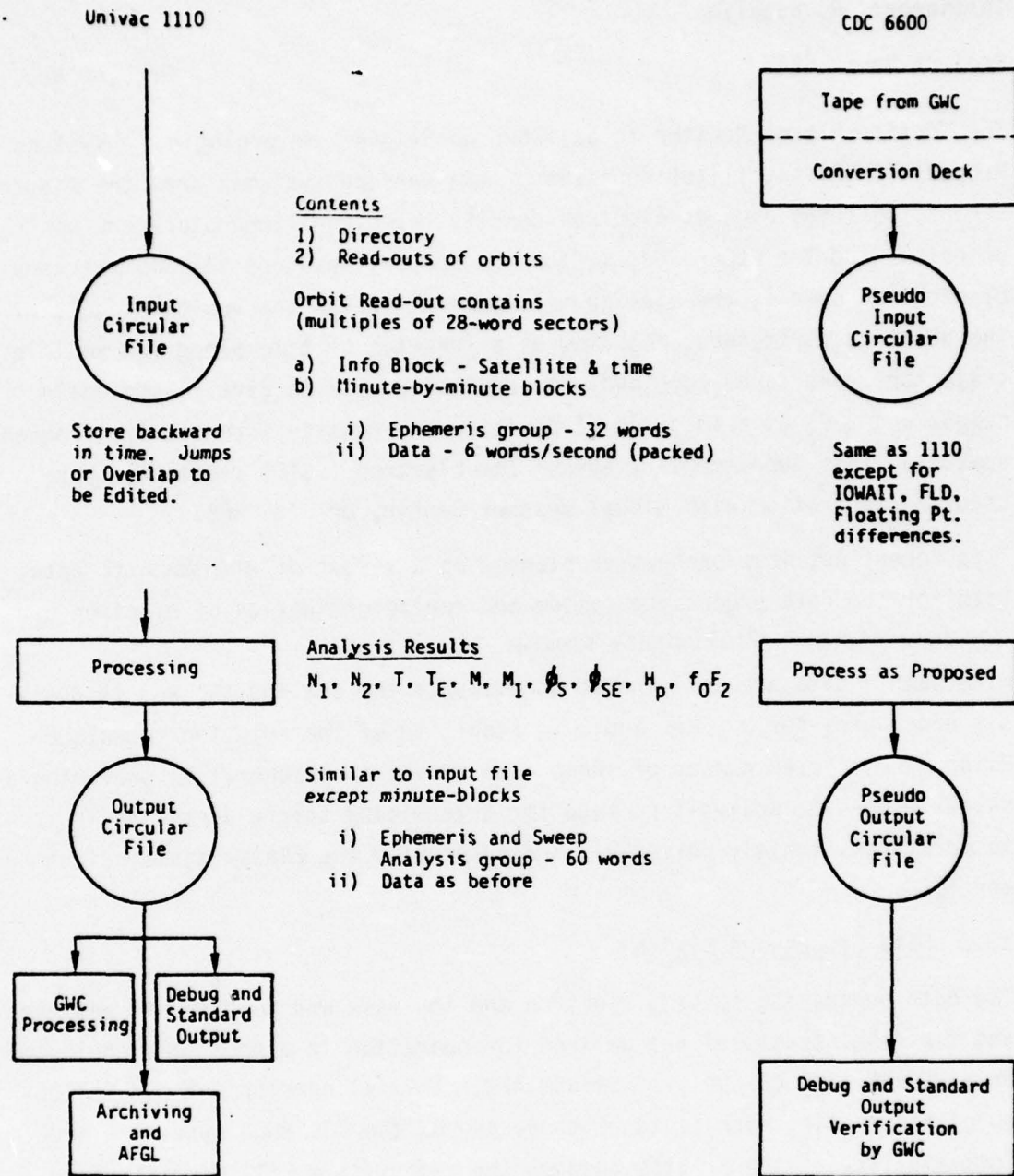


Figure 1. Defense Meteorological Systems Project SSIE Sensor Processing System

from the input circular file, editing and upacking of minute-by-minute blocks of ephemeris and instrumentation data, forward time handling of the backward recorded data, augmentation of the ephemeris group in each minute block by the results of the analysis of the electron and ion sweeps,⁽²⁾ and recreation of an output circular file. Observed vehicle potential and densities from each system will be compared as a check on satisfactory instrument performance. Debug and standard output, archiving capability, and mapping programs are required. A chart outline of files and functions, applicable either on the UNIVAC 1110 or on the CDC 6600, is presented in Figure 1.

13.2 Determination of Electron and Ion Parameters

The raw data obtained from the electron and ion sensor in sweep mode consist of current as a function of applied voltage. From this data electron and ion density and temperature must be deduced, as well as the vehicle potential with respect to the plasma⁽²⁾. Variations in densities between sweep modes are obtained by comparison of current at a fixed applied voltage to that obtained in the sweep mode of the appropriate sensor for the same voltage.

13.2.1 Electron Sweep Mode

The electron sensor current and slope as a function of applied voltage are

$$\begin{aligned} & \text{for } \varnothing \geq 0 \text{ (Retarding)} & & \text{for } \varnothing < 0 \text{ (Accelerating)} \\ I = A e \propto N_e a \frac{\exp(-x^2)}{2\sqrt{\pi}} & = & A e \propto N_e a \frac{(1-x^2)}{2\sqrt{\pi}} \\ \frac{\partial I}{\partial \varnothing_p} = \frac{-Ae^2 \propto N_e a \exp(-x^2)}{2k T_e \sqrt{\pi}} & = & \frac{-Ae^2 \propto N_e a}{2k T_e \sqrt{\pi}} \end{aligned}$$

$$\text{where } x = \frac{1}{a} \sqrt{\frac{2e\varnothing}{m_e}}$$

- \varnothing = potential of sensor with respect to plasma = $\varnothing_{SE} + \varnothing_p$ (volts)
- \varnothing_{SE} = vehicle potential with respect to plasma (volts)
- \varnothing_p = sensor potential with respect to vehicle (volts)
- A = sensor surface area = $4\pi r^2 (\text{m}^2)$ where r is sensor radius (m)
- e = electronic charge = -1.6021×10^{-19} (M.K.S u's)
- \propto = sensor transparency = 0.8

$$\begin{aligned}
 N_e &= \text{ambient electron density } (\text{m}^{-3}) \\
 m_e &= \text{electron mass } (\text{Kg}) \\
 a &= \sqrt{\frac{2kT_e}{m_e}} = \text{most probable electron speed } (\text{m/s}) \\
 T_e &= \text{electron temperature } (^{\circ}\text{K}) \\
 k &= \text{Boltzmann constant} = 1.38054 \times 10^{-23} \text{ (M.K.S u's)}
 \end{aligned}$$

This slope is expected to be constant for accelerating voltages. In actual practice the slope will increase with increasing θ due to Debye Shielding. Thus it should reach a minimum at $\theta = 0$ or $\theta_p = -\theta_{SE}$. The vehicle potential θ_{SE} is therefore obtained by locating this minimum. The electron temperature and density are obtained from the logarithmic slope of the negative of the current at this point and the current respectively.

13.2.2 Ion Sweep Mode

The ion sensor current as a function of applied voltage is

For $e \theta \geq 0$ (Retarding)

$$I = \frac{A e V_s \propto}{2} \sum_{i=1}^j \left\{ N_i \left[1 + \operatorname{erf}(x_i) + a_i \frac{\exp(-x_i^2)}{V_s \sqrt{\pi}} \right] \right\}$$

$$\frac{\partial I}{\partial \theta_p} = -\frac{A e^2 \propto}{\sqrt{2\pi kT}} \sum_{i=1}^j \left\{ N_i \frac{\exp(-x_i^2)}{\sqrt{m_i}} \right\}$$

where

$$x_i = \frac{1}{a_i} \left[V_s - \sqrt{\frac{2e\theta}{m_i}} \right]$$

$$\operatorname{erf}(x) = \frac{2}{\sqrt{\pi}} \int_0^x \exp(-z^2) dz - \text{definition}$$

θ = potential of sensor with respect to plasma = $\theta_s + \theta_p$ (volts)

θ_s = potential of vehicle with respect to plasma (volts)

θ_p = sensor potential with respect to vehicle (volts)

A = sensor aperture area = πr^2 (m^2) where r is aperture radius (m)

e = electronic charge = 1.60210×10^{-19} (M.K.S. u's)

\propto = sensor transparency = 0.59049

N_i = ambient ion density of i^{th} constituent (m^{-3})

m_i = mass of i^{th} constituent

$$a_i = \sqrt{\frac{2 k T}{m_i}} = \text{most probable speed of } i^{\text{th}} \text{ constituent (m/s)}$$

T = average ion temperature of all constituents (^0K)

k = Boltzmann constant = 1.38054×10^{-23} (M.K.S. u's)

j = number of ion constituents

v_s = vehicle speed (m/s) = 7.437172213×10^3 m/s

For $e\theta < 0$ (accelerating)

Put $\theta = 0$ in retarding equation whence $x_i = v_s/a_i$
and I is constant (not a function of θ_p) so

$$\frac{\partial I}{\partial \theta_p} = 0.$$

Only two species H^+ and O^+ are considered since they are expected to dominate at the altitude of interest (835 km). From the above we expect to find a minimum in the slope of I vs θ_p for each of these species present. This corresponds to the voltage just sufficient to repel a stationary ion (relative energy $\frac{1}{2} m_i V_s^2$) from the detector. When both ions are present the two minima will be widely separated and the slope at each can be assumed to be due only to the one ion. The procedure to be followed depends on whether one or two minima in the slope are detected.

13.2.2.1 Two Ion Case

In this case, indicated by the presence of two minima in the slope of current vs applied voltage, the temperature and O^+ density are obtained from solution of simultaneous equations for the current and slope at the O^+ minimum, since H^+ contributes to neither at this point. This yields

$$N_2 = \frac{16 m_p S_2}{A e^2} \left\{ \frac{V_s}{2} + \left[\frac{V_s^2}{4} + \frac{2 I_2 e}{16 m_p S_2} \right]^{\frac{1}{2}} \right\}$$

$$T = \frac{(A e N_2)^2 e^2}{2 \pi k 16 m_p S_2^2}$$

where I_2 is the current, S_2 the negative slope and m_p the proton mass.
The vehicle potential is obtained as

$$\theta_s = \frac{1}{2} \left[\frac{17 m_p V_s^2}{2 e} - (\theta_1 + \theta_2) \right]$$

where θ_1 and θ_2 are the locations of the two minima. The density of H^+ is then directly obtainable from the current at $\theta_p = -\theta_s$. The average ion mass M may also be obtained.

13.2.2.1 One Ion Case

In this case a rigorous algebraic solution of the equations is impossible. Two approximate methods are used to estimate the ion density

- 1) N_1 = electron density
- 2) N_1 obtained from current I_0 at $\theta_p = 0$, which is in the accelerating region ($I = \text{constant}$, $\partial I / \partial \theta_p \neq 0$), by setting the expression in the brackets = 2.

$$(x_1 \gg 0, \text{erf}(x_1) \sim 1, \exp(-x_1^2) \sim 0)$$

The equations for current and slope at the slope minimum ($-S_1$) are solved for mass and temperature yielding

$$m_1 = \frac{(A e \alpha N_1)^2 e}{2 S_1 \pi (I_1 - \frac{A e V_s \alpha N_1}{2})}, \quad T = \frac{(A e \alpha N_1)^2 e^2}{2 \pi k m_1 S_1^2}$$

The vehicle potential is

$$\theta_s = \left[\frac{m_1 V^2}{2 e} - \theta_1 \right]$$

13.2.2.1.1 Second Method of Estimating Mass

Small errors in the current I , or density N , can lead to large errors in the mass as obtained above because of the subtraction which occurs in the denominator. This is particularly dangerous if the ion happens to be H^+ at low temperatures, for which the slope minimum will be steep. Hence a second method is proposed based on the fact that

$$\frac{T_e}{2} \leq T \leq T_e$$

where T_e is the electron temperature. The ion present (H^+ or O^+) can then be assumed to be the one which yields a temperature closest to T_e .

13.2.3 Plasma Scale Height and $f_0 F_2$

We have sufficient information from the M2 EL and M2 ION modes to compute the plasma scale height H_p at a time centered on the two modes which occur

17 secs apart, that is H_p can be deemed to be determined at $(t_o + 8.5)$ where t_o is center of electron sweep, and re-evaluated at an interval of 128 secs.

$$H_p (t_o + 7.5) = k (T_e + T) / M m_p g (m)$$

Where g = acceleration due to gravity at 835 Km altitude (m/sec^2)

$$g = 7.675373268 \text{ m/sec}^2$$

M = average ion mass in AMU's

Substitute in constants:-

$$H_p (t_o + 8.5) = 1.083302743 \frac{(T_e + T)}{M} \text{ Km}$$

$f_0 F_2$ will be determined assuming a diffusive equilibrium model with a specified peak height of the F-region as a function of local time, and is given by the formula

$$n_e = 1.24 \times 10^4 f^2.$$

References

- (1) FLASH System Memos. -- Univac 1100 Time/Sharing Exec, Multi-Processor System, Site AFGWC, January 15, 1976.
- (2) Smiddy, M., Working Papers for "DMSP Plasma Monitor (SSIE)".

Section 14. High Latitude Scintillations Study

14.0 High Latitude Scintillations Study

Initiator: J. Aarons

Project No. 4643

Problem No.: 4785, 4844

14.0 High Latitude Scintillations Study

In order to provide a realistic statistical and dynamic model of scintillation occurrence at sub-auroral and auroral latitudes a model development was undertaken. The primary data consisted of several years' measurements at three stations of 15-minute samples of scintillation excursions in dB of the 137 MHz beacon from the ATS-3 synchronous satellite.

The initial model was to provide mean scintillation excursions as a function of month, time of day, magnetic index, and solar flux. In addition, the data base would be used for statistical distribution, regression, and short term forecasting studies.

14.1 Data Base Creation

Measurement data was provided on punched cards with 16 15-minute samples or 4 hours per card. The scintillation data card format is given below:

Column # 1-t	7	10	12-59	68-69	70-72	73-74	79-80
312	I1 2X,		1X,	16I3 9X , A2	I3	I2 4X , A2	
YR,MO,DA	Period of day	1 9 1-6 or 0	1 9	4 15min readings (x 4 hrs.)	Sat ID e.g.A3	Freq. ID e.g.	'DB' ID 137

1=001 low (whole period)
9=-99 no data (" ")
0=normal (read each column)

These cards were filed in time sequence and were edited for format, duplicates, and invalid range using the CDC Intercom system. The environment considered relevant to scintillations at the sample times was determined as follows:

The K_p values were provided by Dr. P. Fougere of the Space Physics Laboratory and the solar flux values were provided by Mr. W. Barron (LI). The ATS-3 satellite ephemeris was generated using Spadats element sets in the LOKANGL program provided by the Analysis and Simulation Branch. Sub-ionospheric latitude and longitude at 350 Km were obtained using routine SILL2 provided by the Ionospheric Physics Laboratory. The corresponding geomagnetic coordinates and geomagnetic time were then obtained based on G. Gustafsson's 1970 Revised Corrected Geomagnetic Coordinate System, using routines CORRGM2 and MAGTIM developed previously for the Ionospheric Physics Laboratory.⁽¹⁾

The average geographic, geomagnetic and geometric parameters for the sub-ionospheric points for the three stations are:

	Geographic		Inv.		
	Lat.	Long.	Lat.	El.	Az.
Narssarssuaq	5.42	51.0	63.2°	18.0°	208°
Goose Bay	48.3	61.7	60.3°	28.8°	191°
Sagamore Hill	39.3	70.6	53.5°	40.9°	178°

A full data base tape comprising each 15-minute sample and environmental parameters was generated for each station; the record format for each sample is described in Table 1.

TABLE 1. Scintillations Data Base Tape Format

VARIABLE	FORMAT
ID (station-data source)	I2
SAT ident.	A2
FREQ	I3
IY Year	I2
IM Month	I2
IDAY Day	I2
UT Hr.	F5.2
SI Scintillation Index	F4.1
"DB"	A2
Kp Geomagnetic Index (3-hourly)	F3.1
SF27 2.7 GHz solar flux	I3
SF50 5.0 GHz solar flux	I3
SLAT sub-ionos. latitude	F6.2
ELONG sub-ionos. long. (E positive)	F5.1
CGLAT sub-ionos. mag. lat.	F6.2
CGMT mag. time (hr.)	F5.2

The time span and size of the data bases are as follows:

Narssarssuaq	9/17/68 - 9/1/74	146,700 + samples
Goose Bay	1/1/72 - 12/31/74	71,000 + samples
Sagamore Hill	12/1/69 - 11/30/74	148,000 + samples

Goose Bay data for 1974 cover mainly November and December.

14.2 Modeling

Analyses were conducted separately for each station. In order to uniformize the data for modeling studies the data were partitioned into:

12 months, 7 K_p , 3 Solar Flux (2.7 GHz), and 24 UT ranges. The date, K_p , S_f and SI readings were averaged in each block. A compact file was thus made available for high speed iterative modeling studies. The seven K_p ranges are 0-1, 1+ to 2, 2+ to 3, 3+ to 4, 4+ to 5, 5+ to 6, 6+ and up. The three S_f ranges are 0 to 95, 96 to 120, 121 and up. Tables of the averaged SI were provided for each of the stations.

Out of a maximum possible 6048 blocks ($12 \times 7 \times 3 \times 24$), the averaged files comprised the following:

Narssarssuaq	4985 blocks
Goose Bay	4217 blocks
Sagamore Hill	5065 blocks

The empty blocks generally correspond to the highest two K_p ranges, i.e., 5+ and up, and occasionally the highest S_f range. Table 2 shows the averaged SI by hour, solar flux, and K_p range that were obtained for January and February for Goose Bay. 'R' implies absence of data.

TABLE II. VALUES FOR COORDINATE S, I. AVERAGED OVER 5000 DAY

Table 2

An extensive search was conducted to derive empirical models of SI for each of the three stations. Analytical forms of the model were preferred to ensure smooth transitions as a function of the known driving factors, viz. day of year, K_p , S_f and universal time. These forms also permitted use of regression techniques for least squares fitting to the averaged data file. Program MODEL was developed by adapting the IBM multiple linear regression program REGRE⁽²⁾. The square of the residuals of all available averaged data blocks is minimized when the multiple correlation of the partials of all the coefficients that are to be determined vanishes. Selective "fixing" of coefficients is permitted if the solution exhibits instability, and an automated procedure is available for rapidly converging to the optimum.

In the course of the search for improved fits special characteristics of the data were noted which suggested elaborations of the model form. Examples are the delayed peak in the diurnal SI variation with higher K_p , the seasonal effect on diurnal variation amplitude relative to the average SI, the seasonal effect on influence of K_p and S_f , and the need for higher harmonics to represent the diurnal variation. Figure 1 presents the optimized model that was obtained for Goose Bay. An identical model form with different coefficients was also obtained for the other stations⁽³⁾. The cosine terms for the seasonal variation omit $2\pi/365$ and the cosine terms for the diurnal variation omit $2\pi/24$ for convenience. A_S is 0.01 times the 2.7 GHz solar flux; and time is in hours UT.

Full comparative plots of the averaged data and the model were provided for each station. The model predictions used the actual averaged data, K_p and S_f for each hour, and are therefore absent when data are absent. These best fit models may occasionally predict small negative SI's; these should in practice be set to a selected minimum.

Figures 2-5 illustrate the behavior of the averaged data and of the best fitting model equations. The features of increasing scintillations with increasing K_p , and generally with increasing solar flux are evident. The diurnal and seasonal variations are also modeled. Standard deviations of the order of 2 dB are obtained with these models.

Subsequently, effort was directed to bridging the models for the three stations

GOOSE BAY
dB EXCURSIONS AT 137 MHz

$$-1.3 + 1.1 (1 - .77 FD) [1 + .5 (1 - .2 FD) \cos(HR - 2.5 - .6 Kp)]$$

$$+ .06 \cos(2(HR - 6.7)) + .02 \cos(3(HR + .6))]$$

$$* 2 [.3 Kp (1 + .1 FD) + .8 As (1 + 1.2 FD)]$$

$$FD = \cos(DA + .5) + .2 \cos(2(DA - 99))$$

DA = DAY NUMBER

HR = UT HOUR

As = SOLAR FLUX AT 2.76 Hz

Figure 1. Model of Average SI for Goose Bay Optimization is according to Table 2.

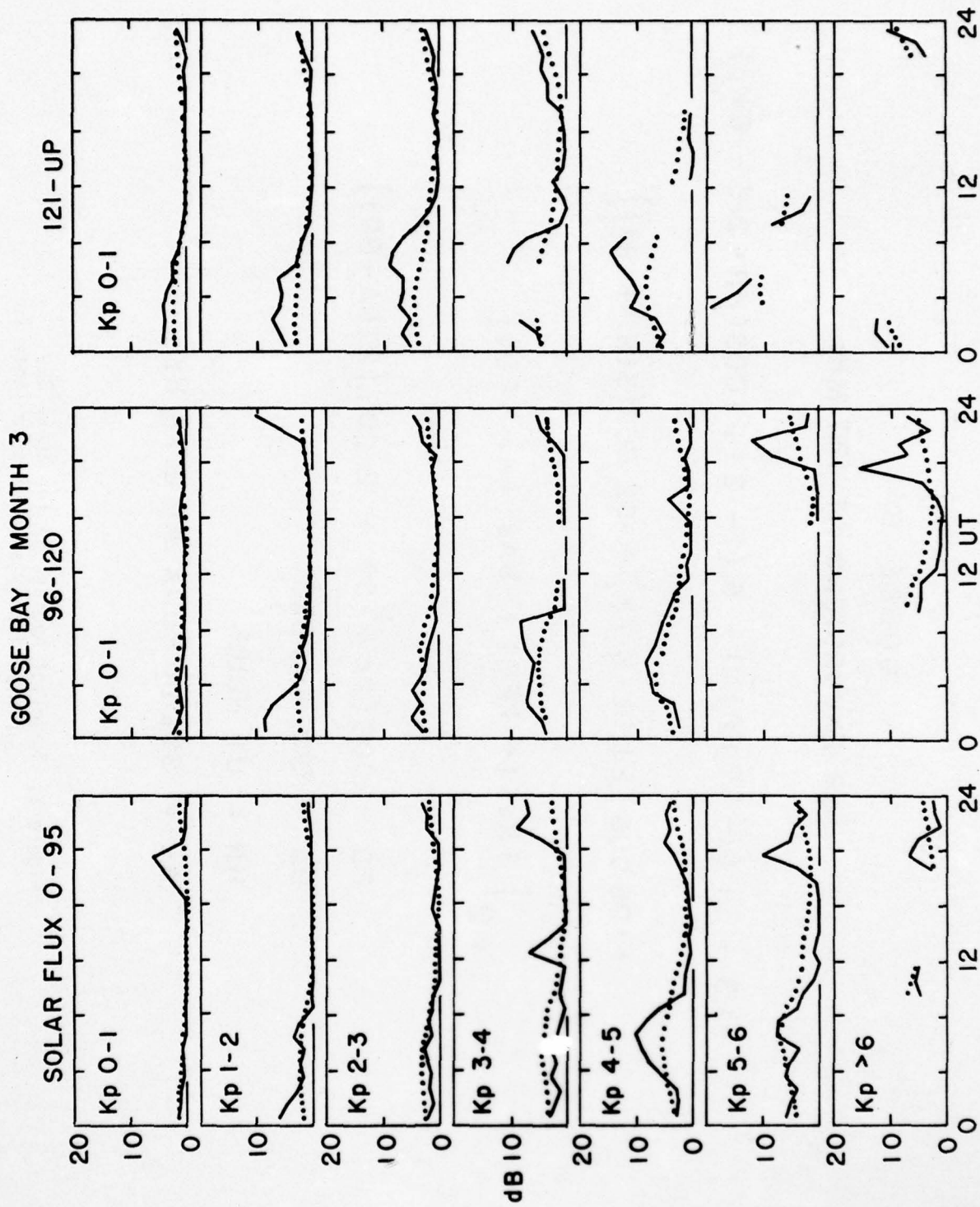


Figure 2. Average SI Data and Model Plots for Goose Bay for March

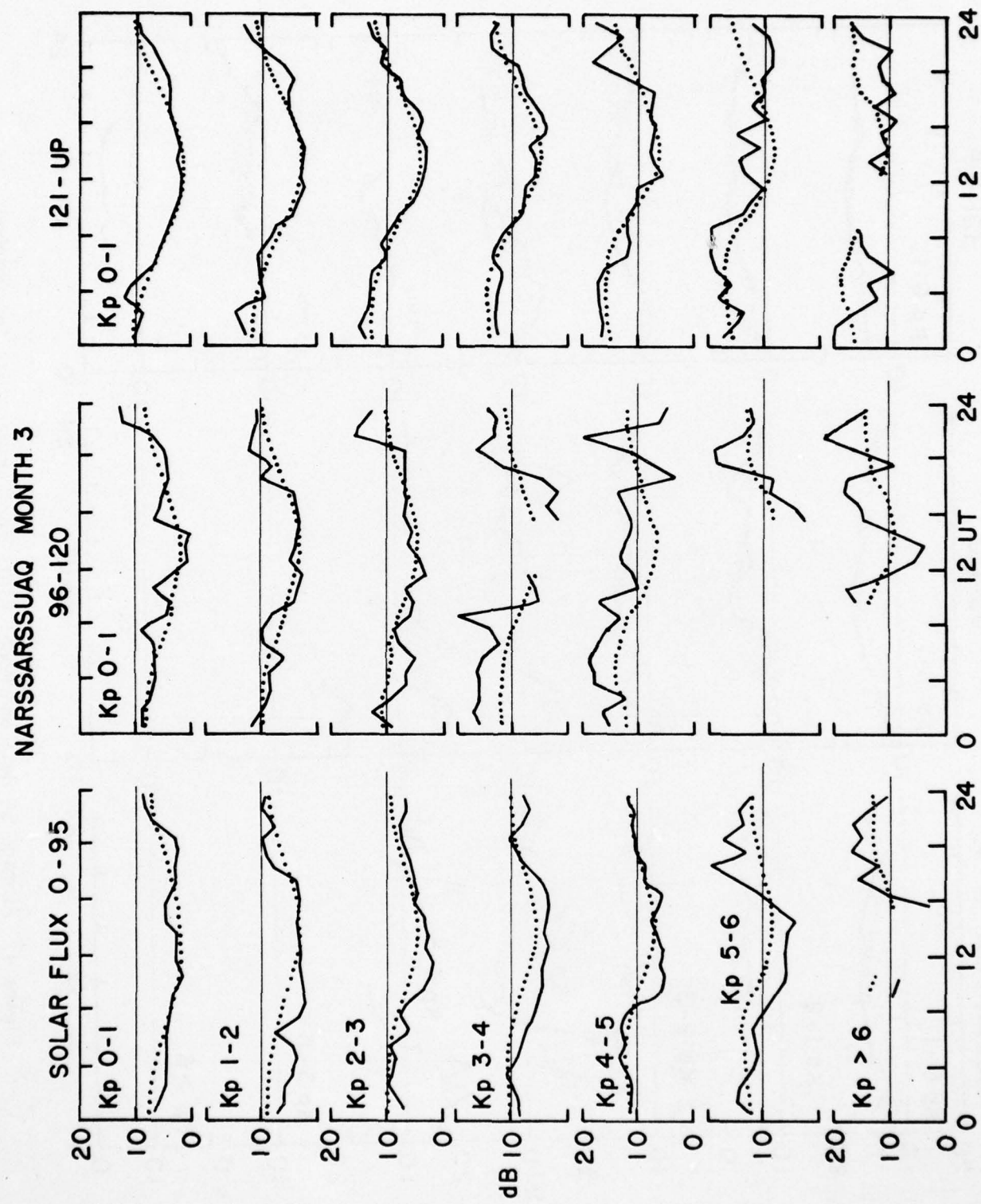


Figure 3. Average SI Data and Model Plots for Narssarsuaq for March

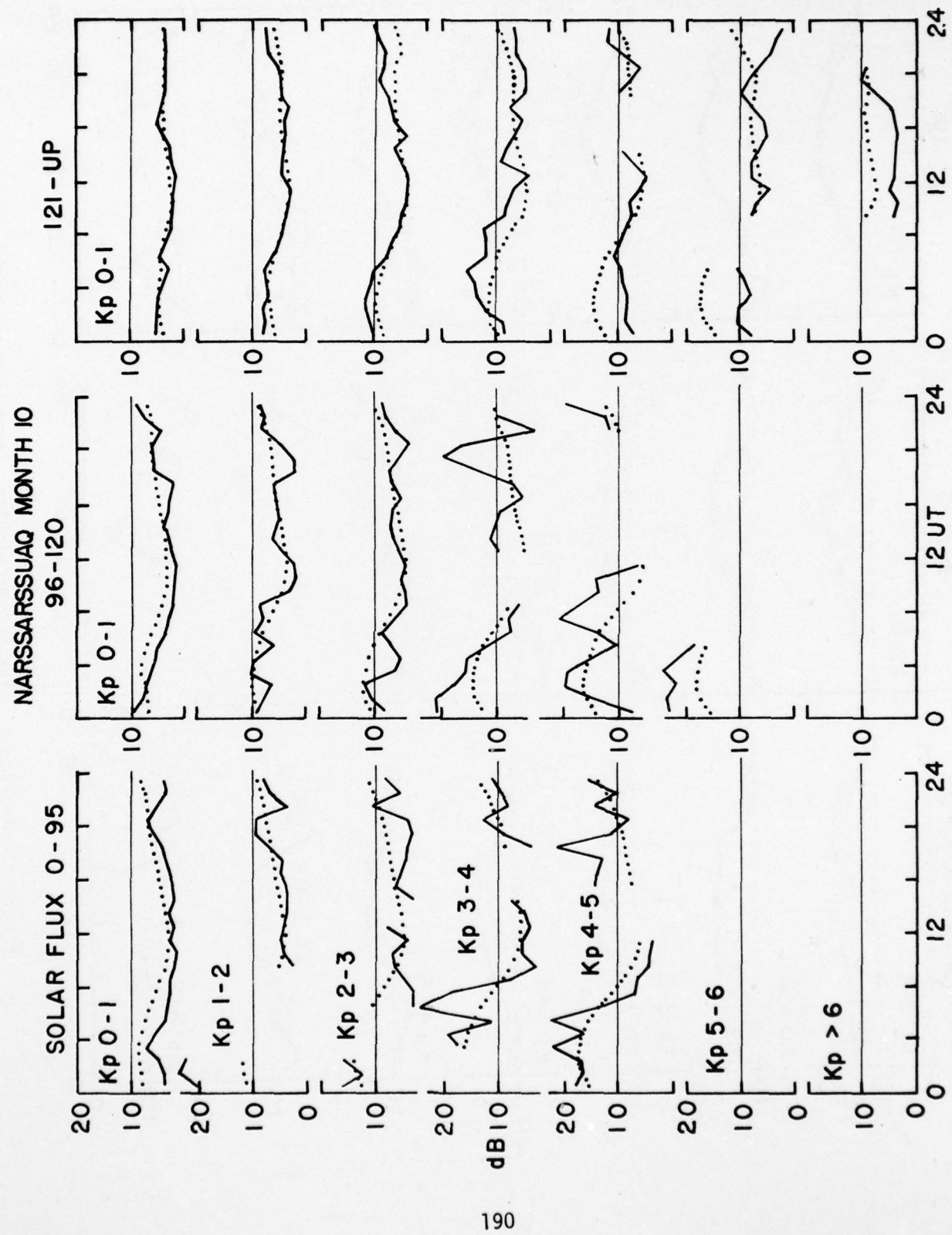


Figure 4. Average SI Data and Model Plots for Narssarsuaq for October

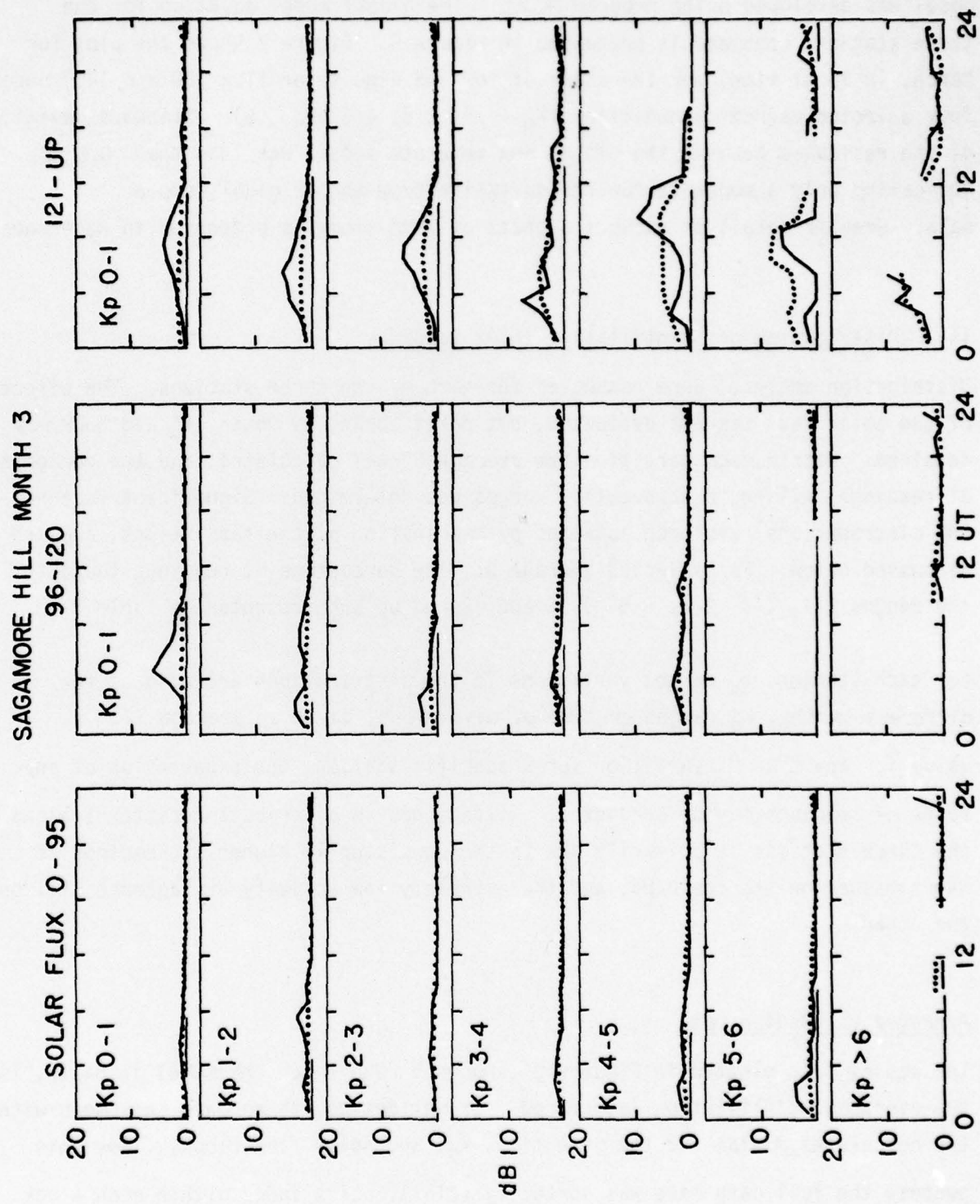


Figure 5. Average SI Data and Model Plots for Sagamore Hill for March

by going to a local time base and by including the geomagnetic latitudinal dependence. The three separate models provided the "data" and the new comprehensive model was developed using program MODEL. The global model equation for the three stations combined is presented in Figure 6. Figure 7 shows the plot for March, in local time, for the cases of low and high solar flux (80 and 140) under four selected magnetic conditions ($K_p = .5, 2.5, 4.5$ and 6.5). Standard deviation of the residuals between the global and separate models was less than 0.8 dB, indicating only a moderate further deviation from the original sample data. Greater detail on various aspects of this study is presented in Reference 3.

14.3 Distribution of Scintillation Index Readings

Distribution analyses were conducted for each of the three stations. The effect of the solar flux was not evaluated, but partitioning by month, K_p and hour was retained. Within each partition the average SI was calculated, and the percentage of readings falling in consecutive ranges was determined. Significant features of the distributions have been obtained by examination of the tabulations, and are discussed below. For selected average SI, the percentage SI readings found in the ranges 0-1, 1-3, 3-6, 6-9, 9-12 and 12 and up are presented in Table 3.

For each station, no marked variations in the distributions are evident for different months, K_p ranges or time of day. Thus, given an average SI value for any time- K_p partition for a specific station, the expectation of any range of readings may be predicted. Differences in distribution patterns among the three stations is primarily due to the consistently higher SI readings at Narssarssuaq on the one hand, and the extremely low activity at Sagamore Hill on the other.

Averaged vs. Median Data

The actual data plotted in Figures 2 through 5 upon which the model is based, is the averaged scintillation data in dB. It was desired to compare this mean with the calculated median for the same time, K_p , and solar flux blocks. For this purpose the full data base was sorted by scintillation index within each block, and a program SIMED obtained the medians for creation of a packed file similar to the averaged file. Figure 8 illustrates both the mean and median dB values for Goose Bay. This data is for the same time period (March) as described in the

II. *Narsarsuaq – Goose Bay – Sagamore Hill based.*

$$PD = \cos(DA + 16) + .3 \cos(2(DA - 30)); \quad FD = CDL * PD \quad XD = SDL * PD$$

$$\left\{ \begin{array}{ll} CL = \cos((PF - 54.4) * \pi / 25) & CDL = 1 + .7 SL \\ SL = \sin((PF - 54.4) * \pi / 25) & SDL = 1 - .3 SL \end{array} \right.$$

where

$$SI = -2.0 + 1.2 CL + 6.5 (1 - .2 FD) [1 + .6 (1 - .16 FD) (1 - .5 SL) \cos(HL + 2 - 4 Kp)]$$

$$+.05 \cos(2(HL-.9)) + .02 \cos(3(HL+3.5)) \left[** (1-CL) * EXA \right]$$

where $EXA = 2 \left[.2K_p(1+.2CL)(1-.1XD) + AS(1-.8SL)(1+.45FD) \right]$

Figure 6. Global High Latitude Model of Average SI Based on ATS-3 Data From 3 Stations

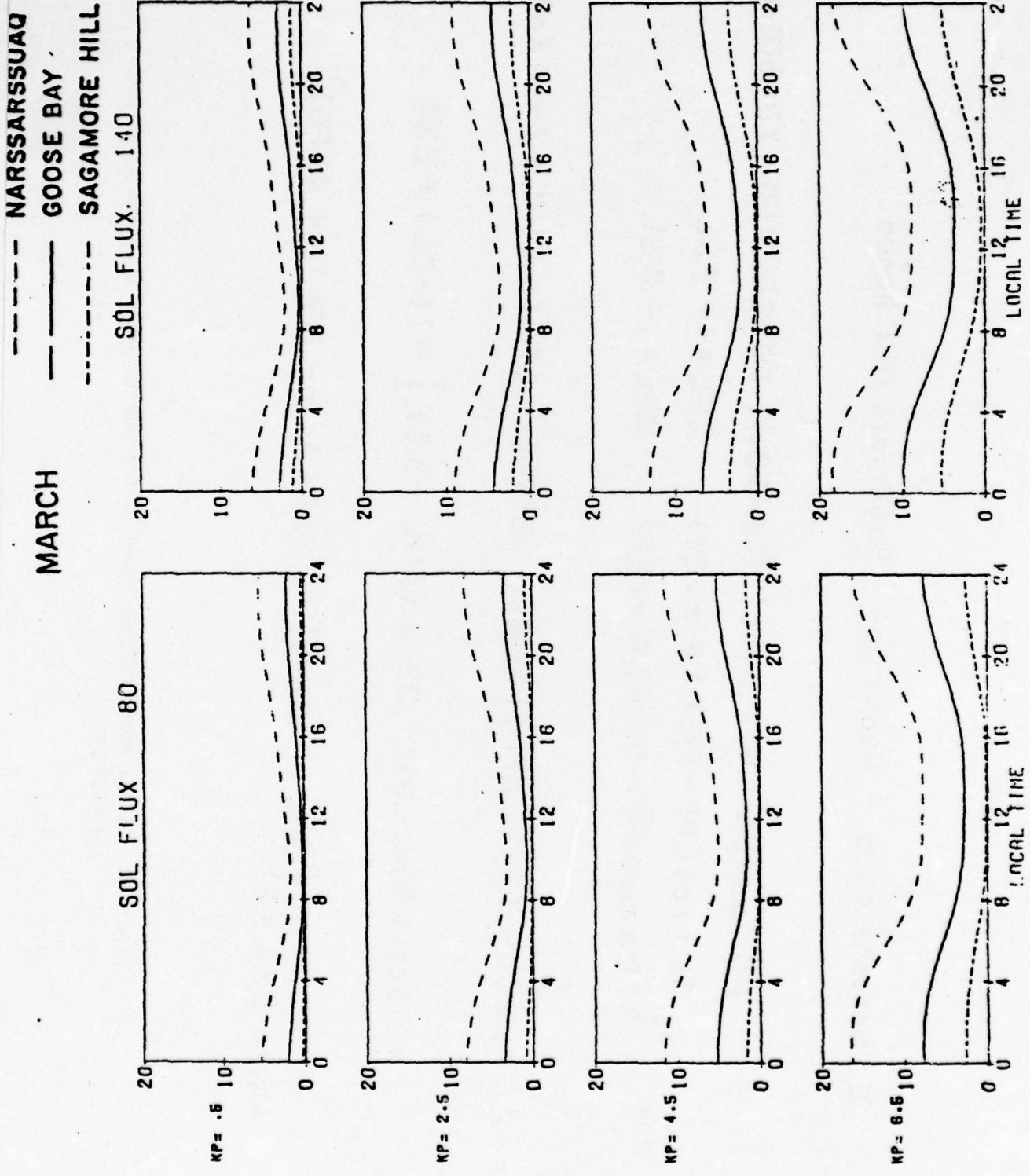


Figure 7. Average SI for March for the 3 Stations as Given by the Global Model

Avg. SI	Station	Percent Occurrence SI Range					
		0-1	1-3	3-6	6-9	9-12	12 up
1.0	Narss.	50	45	5	0	0	0
	Goose Bay	55	35	9	1	0	0
	Sag. Hill	70	15	10	3	2	0
2.0	Narss.	20	55	20	4	1	0
	Goose Bay	40	40	15	3	1	1
	Sag. Hill	55	25	10	5	3	2
3.0	Narss.	20	40	25	10	3	2
	Goose Bay	30	33	18	10	5	4
	Sag. Hill	50	20	12	7	5	6
4.0	Narss.	10	38	28	15	4	5
	Goose Bay	20	33	20	15	5	7
5.0	Narss.	6	33	30	18	5	8
	Goose Bay	12	30	25	18	6	9
6.0	any	3	25	35	20	6	11
8.0	any	2	15	25	20	16	22
10.0	any	1	6	15	18	20	40
13.0	any	1	1	8	10	20	60

Table 3. Distribution of SI readings for various average SI.

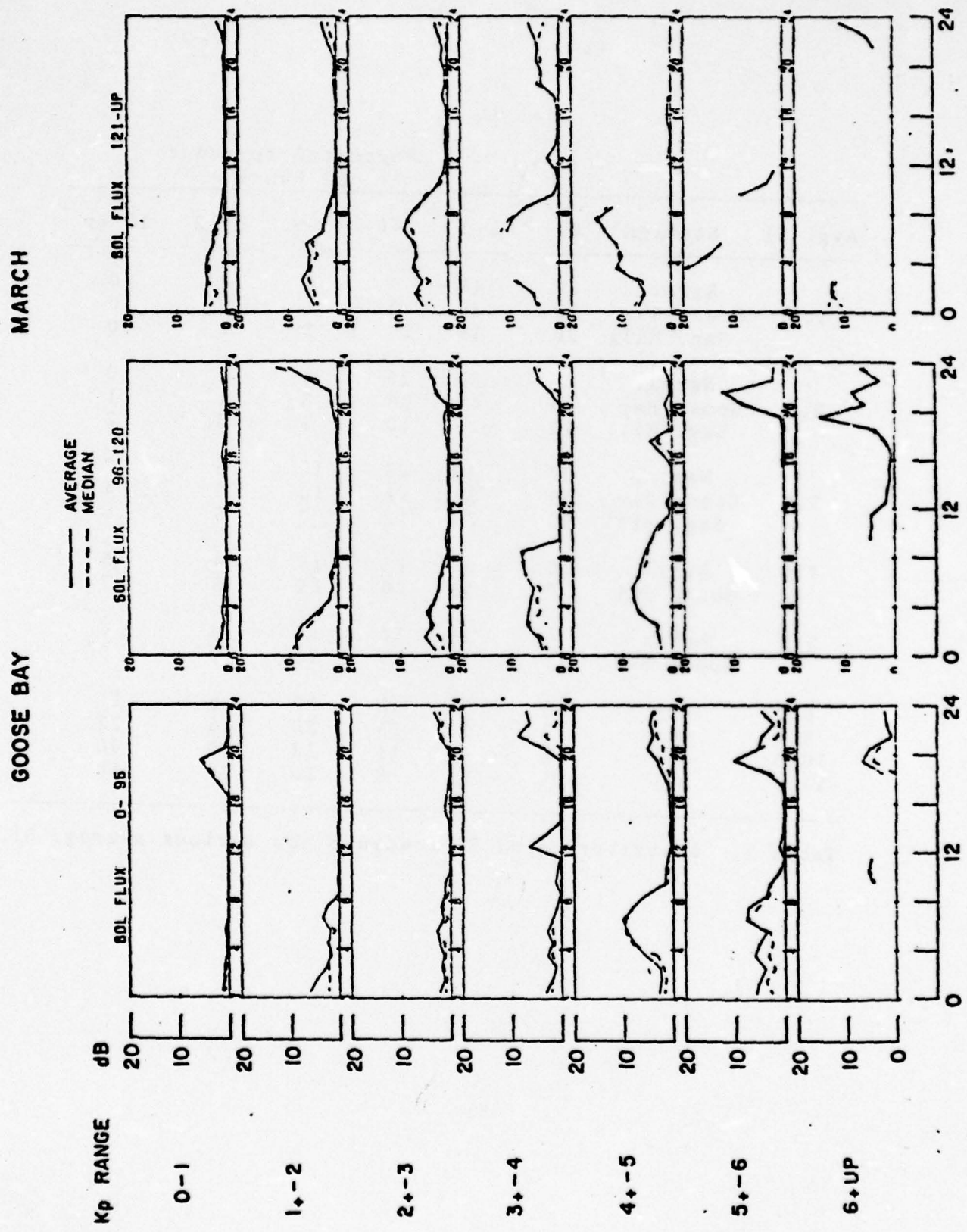


Figure 8. Average and Median SI for Goose Bay for March

earlier figures. It was seen that no substantial differences occur between the averaged and median dB values at any of the stations, except that for low scintillation activity median values tend to be lower than the averaged values.

14.4 Other Analyses

Some intermediate analyses were conducted during the course of this study. For each station, month, and hour the averaged file was used to run a multiple linear regression for scintillation index as a function of K_p and 2.7 GHz solar flux (FL2). The coefficients, correlations, and the multiple correlation was output for each interval. Table 4 is a sample of the output by hour for the first six months for Goose Bay. Plots of the correlation coefficients were also generated. In general the correlation with K_p is much greater than with solar flux. Multiple correlations are consistently high (about 0.8) for Narssarssuaq, around 0.65 for Goose Bay, and about 0.5 for Sagamore Hill.

Separate regression analyses also showed greater correlation with K_p during periods of higher magnetic activity.

A forecasting analysis attempted to predict early 1975 Goose Bay scintillations that were not included in the data base. The results showed unexpectedly high SI observations, possibly because of new instrumentation sensitive to high SI excursions.

Table 4. HOURLY SCINTILLATION INDEX REGRESSION COEFFICIENTS FOR GOOSE BAY Jan.-Jun.

	MONTH 1	MONTH 2	MONTH 3	MONTH 4	MONTH 5	MONTH 6
M FAN	1.1	2.7	4.5	5.7	5.2	5.7
INTERCEPT	-1.9	-0.5	-0.6	-1.3	-0.4	-0.7
KP COEF.	1.5	1.0	1.0	1.0	1.0	1.0
FL2 CO*100	1.6	-1.7	-1.0	-1.0	-1.0	-1.0
MULT. CORR.	-0.6	-0.73	-0.52	-0.60	-0.63	-0.64
KP CORR.	-0.1	-0.72	-0.51	-0.60	-0.64	-0.64
FL2 CORR.	-0.18	-0.25	-0.03	-0.12	-0.06	-0.16
# AVERAGES	13	14	14	14	14	14
M FAN	1.1	2.1	3.1	4.0	4.1	4.6
INTERCEPT	-1.9	-0.4	-0.3	-0.3	-0.3	-0.3
KP COEF.	1.5	1.0	1.0	1.0	1.0	1.0
FL2 CO*100	1.6	-1.7	-1.0	-1.0	-1.0	-1.0
MULT. CORR.	-0.6	-0.73	-0.52	-0.60	-0.63	-0.64
KP CORR.	-0.1	-0.72	-0.51	-0.60	-0.64	-0.64
FL2 CORR.	-0.18	-0.25	-0.03	-0.12	-0.06	-0.16
# AVERAGES	13	14	14	14	14	14
M FAN	1.1	2.7	4.5	5.7	5.2	5.7
INTERCEPT	-5.6	-6.8	-9.8	-10.1	-8.5	-12.5
KP COEF.	1.6	1.0	1.0	1.0	1.0	1.0
FL2 CO*100	5.7	6.5	9.6	11.1	9.1	11.7
MULT. CORR.	-0.75	-0.65	-0.69	-0.95	-0.92	-0.83
KP CORR.	-0.36	-0.41	-0.43	-0.30	-0.34	-0.36
FL2 CORR.	-0.67	-0.64	-0.74	-0.86	-0.90	-0.77
# AVERAGES	16	16	15	15	15	16
M FAN	1.1	2.1	3.1	4.0	4.1	4.6
INTERCEPT	-5.6	-6.8	-9.8	-10.1	-8.5	-12.5
KP COEF.	1.6	1.0	1.0	1.0	1.0	1.0
FL2 CO*100	5.7	6.5	9.6	11.1	9.1	11.7
MULT. CORR.	-0.75	-0.65	-0.69	-0.95	-0.92	-0.83
KP CORR.	-0.36	-0.41	-0.43	-0.30	-0.34	-0.36
FL2 CORR.	-0.67	-0.64	-0.74	-0.86	-0.90	-0.77
# AVERAGES	16	16	15	15	15	16
M FAN	1.1	2.7	4.5	5.7	5.2	5.7
INTERCEPT	-4.1	-6.3	-11.9	-16.0	-13.4	-11.9
KP COEF.	0.5	0.7	1.0	1.0	1.0	1.0
FL2 CO*100	6.5	10.1	12.8	17.1	12.7	11.2
MULT. CORR.	-0.61	-0.71	-0.64	-0.94	-0.91	-0.91
KP CORR.	-0.38	-0.39	-0.46	-0.69	-0.76	-0.75
FL2 CORR.	-0.67	-0.60	-0.70	-0.63	-0.56	-0.50
# AVERAGES	17	17	16	16	16	16
M FAN	1.1	2.1	3.1	4.0	4.1	4.6
INTERCEPT	-3.2	-6.0	-5.0	-3.0	-3.1	-4.4
KP COEF.	-0.4	-0.5	-0.4	-0.1	-0.1	-0.1
FL2 CO*100	1.1	-1.1	-1.6	-1.6	-1.6	-1.6
MULT. CORR.	-0.27	-0.30	-0.23	-0.74	-0.66	-0.67
KP CORR.	-0.27	-0.29	-0.31	-0.62	-0.67	-0.66
FL2 CORR.	-0.62	-0.10	-0.32	-0.31	-0.26	-0.37
# AVERAGES	17	17	17	17	17	17
M FAN	1.1	2.1	3.1	4.0	4.1	4.6
INTERCEPT	-5.7	-6.1	-5.3	-5.2	-5.1	-5.5
KP COEF.	1.6	1.0	1.0	1.0	1.0	1.0
FL2 CO*100	6.5	10.1	12.8	17.1	12.7	11.2
MULT. CORR.	-0.65	-0.59	-0.52	-0.66	-0.63	-0.65
KP CORR.	-0.35	-0.47	-0.65	-0.62	-0.64	-0.60
FL2 CORR.	-0.62	-0.25	-0.01	-0.19	-0.14	-0.27
# AVERAGES	15	15	15	15	15	15
M FAN	1.1	2.1	3.1	4.0	4.1	4.6
INTERCEPT	-5.7	-6.1	-5.3	-5.2	-5.1	-5.5
KP COEF.	1.6	1.0	1.0	1.0	1.0	1.0
FL2 CO*100	6.5	10.1	12.8	17.1	12.7	11.2
MULT. CORR.	-0.65	-0.59	-0.52	-0.66	-0.63	-0.65
KP CORR.	-0.35	-0.47	-0.65	-0.62	-0.64	-0.60
FL2 CORR.	-0.62	-0.25	-0.01	-0.19	-0.14	-0.27
# AVERAGES	15	15	15	15	15	15
M FAN	1.1	2.1	3.1	4.0	4.1	4.6
INTERCEPT	-5.7	-6.1	-5.3	-5.2	-5.1	-5.5
KP COEF.	1.6	1.0	1.0	1.0	1.0	1.0
FL2 CO*100	6.5	10.1	12.8	17.1	12.7	11.2
MULT. CORR.	-0.65	-0.59	-0.52	-0.66	-0.63	-0.65
KP CORR.	-0.35	-0.47	-0.65	-0.62	-0.64	-0.60
FL2 CORR.	-0.62	-0.25	-0.01	-0.19	-0.14	-0.27
# AVERAGES	17	17	17	17	17	17

References:

1. "Analysis and Programming for Scientific Research", Logicon, Inc.
Final Report, AFCRL-TR-74-0480, September 1974.
2. "System/360 Scientific Subroutine Package -- Version III", IBM
Application Program Manual GH20-0205-4.
3. Aarons, J., Mullen, J., Whitney, H., Martin, E., Bhavnani, K., and
Whelan, L., "A High-Latitude Empirical Model of Scintillation Ex-
cursions: Phase I", AFGL-TR-76-0210, September 1976.

Section 15. Real Time Signal Processing With CSP-30

15.0 Real Time Signal Processing With CSP-30

Initiator: J. Schindler

Project No.: 5635

Problem No.: 4794

15.1 Introduction

The purpose of this project is to develop assembly language real-time software for the CSP-30 digital signal processor. The software will be used in a simulation experiment designed to test recently-developed filtering techniques⁽¹⁾ for maximizing signal-to-clutter ratio when detecting a moving target with moving radar. The processor will receive 16 bit complex signals from each of several antenna elements (eventually 8) at a pulse repetition rate of 1.8 KHz. For each antenna element and pulse a signal is received from each of up to 16 contiguous range bins. For each range bin and pulse a linear combination of the signals for the different antenna elements are formed which define the radar patterns. These are then filtered and the outputs displayed on a storage display scope along with other pertinent information.

15.2 Maximum Signal to Clutter Processing

The Doppler shift of a signal received by a moving radar (velocity v_0) from a stationary clutter element at angle θ with respect to the velocity vector is⁽¹⁾

$$\omega_d = \frac{4\pi v_0}{\lambda} \sin \theta \quad (1)$$

Where λ is the wavelength of the signal. Thus for equal transmitted and received antenna patterns $P(\theta)$ the doppler clutter spectrum is

$$D(\omega_d) = P^2 \left[\Theta(\omega_d) \right] = P^2 \left(\sin^{-1} \frac{\lambda \omega_d}{4\pi v_0} \right)$$

The presence of a moving target within a given interval of the doppler spectrum may be detected by constructing a received antenna pattern with a null over the appropriate angular range to exclude ground clutter contributing to this interval and filter the resulting signal to pass frequencies within this interval. Reference 1 describes a method of selecting the coefficients defining either the antenna pattern or filter to maximize the signal to clutter ratio by deriving an expression for it which is quadratic in the set of coefficients (antenna or filter) which are to be varied. The results are as follows:

(1) Radar coefficients

$$\bar{X} = \begin{pmatrix} X_1 \\ X_2 \\ \vdots \\ X_N \end{pmatrix}$$

where X_n is the complex coefficient of the n^{th} element in the radar pattern:

$$\bar{X} = \bar{B}^{-1} \bar{a}$$

where

$$B_{np} = \sum_{m=1}^N \sum_{q=1}^N S_{mn}^* s_{qp} \int dy \exp \left[-j(m-q)dky \right] \cdot \left| F\left(\frac{2yv_0}{\lambda}\right) \right|^2 P_t (\sin^{-1}y) \left| f(\sin^{-1}y) \right|^2 (1-y^2)^{\frac{1}{2}}$$

$$\bar{a} = \bar{s}^T \bar{e}^*$$

with,

$$S_{mn} = S_{mn} + S'_{mn}$$

S'_{mn} = field scattering coefficient from m^{th} radar element to n^{th} radar element

$$k = 2\pi/\lambda$$

d = spacing between antenna elements

$f(\theta)$ = common pattern of individual antenna elements

* = complex conjugate operation

T = complex conjugate transpose operation

$F(f) =$ doppler filter frequency response

$P_t(\theta) =$ transmitted antenna power pattern

$$e_i = \exp(j\lambda k d \sin \theta_t)$$

$\theta_t =$ angle of target

$$j = \sqrt{-1}$$

(2) Filter Coefficients α_i :

$$\bar{\alpha} = \bar{B}^{-1} \bar{a},$$

Where

$$B_{np} = \int_{-\pi/2}^{\pi/2} P_r(\theta) P_t(\theta) \exp [2jkv_0(n-p)T \sin \theta] d\theta$$

$$a_n = \exp(-j\omega_t n T)$$

With

$P_r(\theta) =$ received antenna pattern

$T =$ time spacing between samples.

$\omega_t =$ doppler frequency of target

15.3 Hardware

Figure 1 shows the probable configuration in which the CSP-30 will be used in this experiment. The CSP-30⁽²⁾ is a 16 bit digital computer with signed fixed point arithmetic and a basic cycle time of 100 nanoseconds. It contains 4096 words of high speed integrated circuit (IC) memory and 32767 of low-speed (600 n sec) core memory. In addition there exists an accumulator file of 32 registers and a super accumulator or A register. Background instructions are available to initiate transfer of data between core and the higher 16 registers,

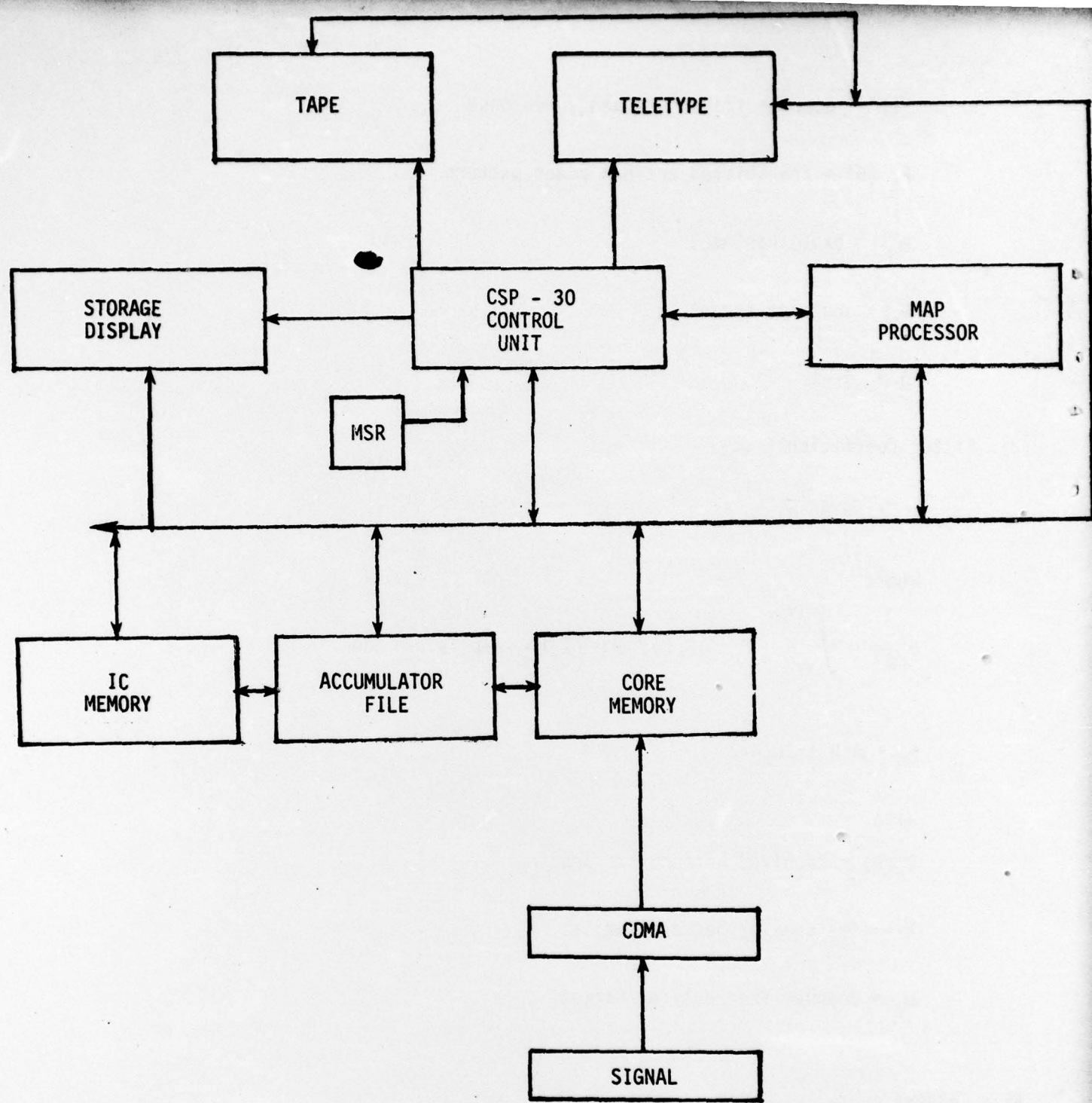


FIGURE 1. CSP-30 OPERATIONAL CONFIGURATION

partially concurrent with the execution of subsequent instructions.

Programmed one word data transfers may be initiated to and from the tapes and teletype. The digital radar signals are to be input as blocks through the core direct memory access channel (CDMA). The storage display scope contains a 1024x1024 point screen on which display may be stored at the option of the program. Hardware facilities include plots of points, cursors, x and y axes.

Priority interrupt logic and status words (not shown) permit overlapping of I/O and other operations. CDMA operations may be overlapped with any other operation not accessing core memory.

A direct communication between the operator and computer is possible through the master switch register (MSR), a set of 16 console switches, numbered 0 through 15.

A special high-speed (MAP) processor to be provided by CSPI will facilitate the real-time processing to be done.

15.3.1 Timing Considerations

Table 1 shows significant timing data which will effect this experiment. The complex multiplication operations include 4 single precision multiplications, 2 addition and any memory access required (other than core). The CDMA data transfer time is for the case in which the CDMA has exclusive access to core memory (an option available to the program). Timing information for data transfers to and from the MAP processor is not available as of this writing.

It is expected that several processes might be taking place simultaneously to make optimum use of the facility, such as,

- A. Process the data (form radar patterns and filter) for one pulse
- B. Input data for next pulse
- C. Output results from previous pulse

Based on Table 1 the following time estimates are obtained:

A. Form p antenna patterns for m range bins n antenna elements and filter with f point filter

$$t_A = mp(n+f)t_M$$

B. Input next pulse to IC memory

$$t_I = 4.4mn \mu\text{sec}$$

C. Display results of previous pulse (one point for each antenna pattern of

each range bin)

$$t_D = 30 \text{ m}\mu\text{sec}$$

The advantage of using the MAP processor for (A) is evident. Even if this is the case, however, it is apparent that at most 3 radar patterns can be formed for the planned 8 antenna elements and 16 range bins, in the 500 μ sec pulse interval. Thus the number of range bins may have to be reduced to obtain better Doppler resolution. The timing requirement t_D could be reduced by displaying only the largest outputs.

TABLE 1. Approximate CSP-30 Timing Data

complex Multiplication, t_M (CSP-30)	7 μ sec
complex Multiplication, t_M (MAP)	1 μ sec
CDMA Data Transfer	1 μ sec/word
Core to accumulator file Data Transfer	.6 μ sec/word
Accumulator File to IC Data Transfer	.6 μ sec/word
Display	30 μ sec/point

15.4 Fast Fourier Transform Display

To gain familiarity with the computer a program, described in Figures 2-5, was written to compute and display the discrete Fourier transform of some simple functions. The discrete Fourier transform of an N point time sequence f_i is

$$F_K = N^{-1} \sum_{i=1}^N f_i e^{-2\pi j(i-1)}$$

To compute F_K the program makes use of the Fast Fourier Transform (FFT) algorithms incorporated into a signal processing software supplied with the computer. The "VIDEO" function referred to in Figures 2 and 4 is described in Reference 4. (3)

REFERENCES

1. "Processing for Maximum Signal-to-in AMTI Radars", William B. Goggins, Jr., Lt. Col. USAF, and John K. Schindler, AFCRL-TR-74-0577, 1974.
2. "CSP-30 Programmer's Reference Manual", Computer Signal Processors, Inc. (CSPI), 1972.
3. "An Algorithm for the Machine Calculation of Complex Fourier Series", J. W. Cooley and J. Tukey, Math. Comp., Vol. 19, P. 297-301 (1965); "Numerical Methods for Scientists and Engineers", R. W. Hamming, McGraw-Hill, New York, 1973, Chapter 33.
4. "A Computer Simulation Scheme for an Aircraft Moving Target Indication System (Part 1)", Theodore B. Barrett, AFCRL-TR-75-0313, 1975.

```

!FFT TEST
!
!COMPUTES AND DISPLAYS ONE OF FOLLOWING FUNCTIONS
!16 POINT SIMULATED SIGNAL FROM BARRETT'S CMC
!SUBROUTINE VIDEO (SEE LISTING UNDER VIDEO)
!
!1024 POINT COMPLEX EXPONENTIAL
!.5*EXP(-J*THETA), THETA=(I-1)*N*2*PI/1024,
!WHERE N = FREQUENCY
!
!SQUARE PULSE = .5 I .LT. W
!          = 0   1 .GT. W
!W IS WIDTH OF PULSE FROM 1 TO 1024
!
!DISPLAY IS EITHER LOG BASE 2 OF MAGNITUDE AND PHASE
!FOR REAL AND IMAGINARY PARTS. THE LOG PLOT OCCUPIES THE UPPER
!HALF OF THE SCREEN, WITH THE PHASE IN THE LOWER HALF
!WHILE THE REAL PART IS PLACED IN THE UPPER HALF
!AND THE IMAGINARY PART IN THE LOWER HALF
!
!AXIS SCALES
!X AXIS -PRF/2 .LE. X .LE. +PRF/2
!WHERE PRF IS PULSE REPETITION FREQUENCY
!
!Y AXIS
!LOG PLOT -16 .LE. Y .LE. 0 PHASE -PI .LE. Y .LE. PI
!REAL AND IMAGINARY PARTS -2*N .LE. Y .LE. +2*N
!WHERE N IS THE NUMBER OF CURSORS APPEARING
!IN A HORIZONTAL ROW IN THE UPPER HALF OF
!SCREEN, POSITIVE IF NEAR THE TOP,
!NEGATIVE IF NEAR CENTRAL X AXIS

```

Figure 2. Fast Fourier Transform Display:
 Description of Options. Here $j = \sqrt{-1}$,
 I is point number (from 1 to 1024),
 N is in units of PRF/1024, and the pulse repetition (sampling)
 frequency PRF is arbitrary.

```

*****SWITCH SETTINGS*****
0  SUPPRESS PLOT OF AXES
1  PLOT LOG OF MAGNITUDE AND PHASE
   RATHER THAN REAL AND IMAGINARY
   PARTS OF DATA
2  ENTER NON-STORE MODE INITIALLY!
   REFRESH PLOT UNTIL MSR 2 RESET, THEN STORE
   PLOT AND HALT
   OTHER SETTINGS CAN BE CHANGED WITH MSR 2 OR,
   CHANGING DISPLAY
3  FOR 16 POINT BARRETT VIDEO, PLOT IMAGINARY
   PART OF FFT AS CURSOR RATHER THAN POINT!
   FOR 1024 POINT FUNCTION PLOT SQUARE PULSE IF SET!
   ELSE PLOT COMPLEX EXPONENTIAL
4  16 POINT BARRETT VIDEO SIGNAL USED
   ELSE 1024 POINT SIGNAL SPECIFIED BY MSP 3,5-15
5-15 WIDTH OF PULSE OR FREQUENCY OF COMPLEX EXPONENTIAL
*****
```

Figure 3. Console Master Switch Register (MSR) Settings to Implement Various Options

VIDEO: - .01346,.1675
- .04441,.2008
- .05700,.2275
- .05861,.2492
- .03732,.2641
.005042,.2475
.03818,.1892
.03973, .1079
.005959,.02090
- .07080,-.05562
- .1827,-.08286
- .2757,-.03831
- .2997,.03353
- .2777,.07305
- .2606,.08974
- .2365,.1252

Figure 4. 16 Point Complex Simulation Signal Generated by Subroutine VIDEO (Reference 4)

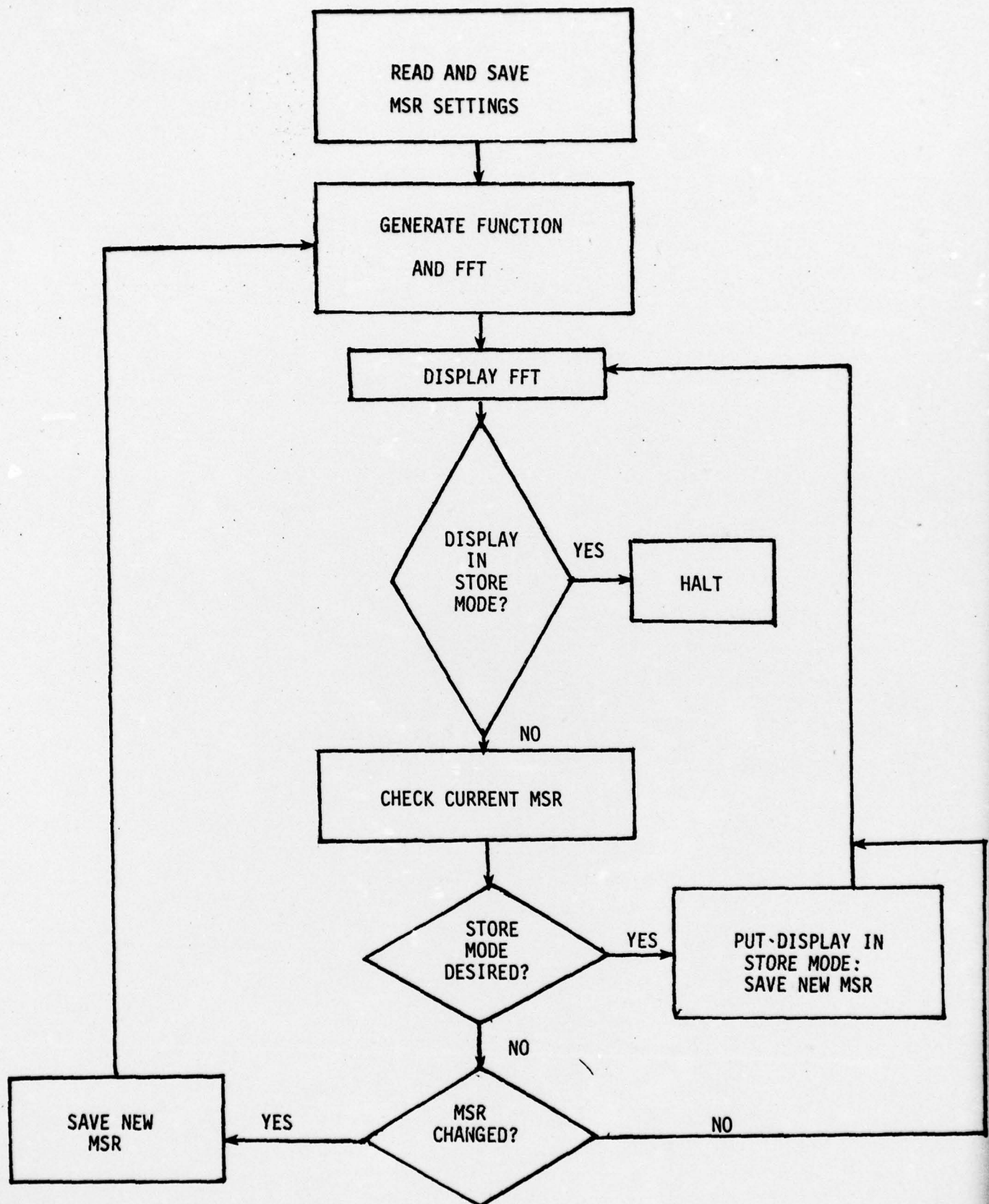


FIGURE 5. FLOW DIAGRAM FOR FFT DISPLAY PROGRAM